UC Riverside

UC Riverside Electronic Theses and Dissertations

Title

Adsorptions and Reactions on Topological Insulator Surfaces Investigated by Low Energy Ion Scattering

Permalink

https://escholarship.org/uc/item/5825x2z3

Author

Zhu, Haoshan

Publication Date

2019

Copyright Information

This work is made available under the terms of a Creative Commons Attribution License, availalbe at https://creativecommons.org/licenses/by/4.0/

Peer reviewed|Thesis/dissertation

eScholarship.org Powered by the California Digital Library
University of California

UNIVERSITY OF CALIFORNIA
RIVERSIDE

Adsorptions and Reactions on Topological Insulator Surfaces Investigated by Low Energy Ion Scattering

A Dissertation submitted in partial satisfaction
of the requirements for the degree of

Doctor of Philosophy

in

Physics

by

Haoshan Zhu

June 2019

Dissertation Committee:
Dr. Jory Adam Yarmoff, Chairperson
Dr. Jing Shi
Dr. Nathaniel Gabor

Copyright by
Haoshan Zhu
2019

The Dissertation of Haoshan Zhu is approved:

_____

_____

_____

Committee Chairperson

University of California, Riverside

ACKNOWLEDGEMENTS

During the past five years, I was immersed in the surface science world in Prof. Yarmoff's lab. The surface techniques and science are exciting and attractive, but the everyday experiments can be repetitive, and the result is usually frustrating. It would be impossible for me to go through this journey without the accompany of all the people I met here.

Highest gratitude to my advisor Jory Yarmoff. He gives me full freedom in arranging my research but is always available when I need help and instruction.

I was lucky to get instructed by Weimin Zhou in operating the chamber. Chao Lian was helpful in teaching me DFT calculations. Thanks to all the group members, with their help, I could set up the MBE chamber and do experiment quickly and smoothly.

Special thanks to Christopher Salvo, who accompanied me in numerous days in the lab. He's willing to share his life experience and knowledge with me and bring me closer to the American culture. He also offered great help in my job searching.

I am grateful to Siyu and all my friends in Riverside, without whom life could be boring in a foreign country.

This thesis is based on work supported by, or in part by, the National Science Foundation under Grant No. CHE – 1611563, the U.S. Army Research Laboratory and the U.S. Army Research Office under Grant No. 63852-PH-H.

Last but not least, many thanks to my parents for supporting and believing in me all the time.

PUBLICATIONS AND PRESENTATIONS

PUBLICATIONS

[1] *"The growth of bismuth on Bi_2Se_3 and the stability of the first bilayer",* **H. Zhu**, W. Zhou, and J. A. Yarmoff, Thin Solid Films **660**, 343 (2018)

[2] *"Spatial distribution of topological surface State electrons in Bi_2Te_3 probed by low energy Na^+ ion scattering",* W. Zhou, **H. Zhu**, and J. A. Yarmoff, Phys. Rev. B **97**,035413 (2018)

[3] *"Halogen Adsorption and Reaction with $Bi_2(Se,Te)_3$ and $Bi/Bi_2(Se,Te)_3$",* **H. Zhu**, W. Zhou, and J. A. Yarmoff, J. Phys. Chem. C **122**,16122 (2018)

[4] *"Cs adsorption on Bi_2Se_3",* **H. Zhu**, W. Zhou, and J. A. Yarmoff, Surf. Sci. **683**, 17 (2019)

[5] *"Preparation of clean surfaces and se vacancy formation in Bi_2Se_3 by ion bombardment and annealing",* W. Zhou, **H. Zhu**, C. M. Valles, and J. A. Yarmoff, Surf. Sci. **662**, 67 (2017)

[6] *"Detailed analysis of impact collision ion scattering spectroscopy of bismuth selenide",* W. Zhou, **H. Zhu**, and J. A. Yarmoff, J. Vac. Sci. Technol. A **35**, 03E104 (2017)

[7] *"Termination of single-crystal Bi_2Se_3 surfaces prepared by various methods",* W. Zhou, **H. Zhu**, and J. A. Yarmoff, Phys. Rev. B **94** (2016)

[8] *"Surface structure of in situ cleaved single crystal Bi_2Se_3 measured by low energy ion scattering",* W. Zhou, **H. Zhu**, and J. A. Yarmoff, J. Vac. Sci. Technol. B **34**, 04J108 (2016)

POSTERS AND PRESENTATIONS

Presentation APS March meeting 2017 New Orleans.
Characterization and Halogen Etching of Bi Bilayer on Bi_2Se_3/Bi_2Te_3

Presentation APS March meeting 2018 Los Angeles.
Spatial distribution of topological surface state electrons in Bi_2Te_3 probed by low-energy Na^+ ion scattering

Presentation AVS 65th International Symposium & Exhibition 2018 Long Beach.
Adsorption and Reactions on Topological Insulators Surfaces Probed by Low Energy Ion Scattering

Poster AVS 65th International Symposium & Exhibition 2018 Long Beach.
Adsorption and Reactions on Topological Insulators Surfaces Probed by Low Energy Ion Scattering

ABSTRACT OF THE DISSERTATION

Adsorptions and Reactions on Topological Insulator Surfaces
Investigated by Low Energy Ion Scattering

by

Haoshan Zhu

Doctor of Philosophy, Graduate Program in Physics
University of California, Riverside, June 2019
Dr. Jory A. Yarmoff, Chairperson

Topological insulator (TI) materials are insulators in the bulk while they conduct along the surface, which makes them promising for future quantum computing and spintronics applications. The momentum-spin locked electron states are concentrated in the first few atomic layers, which demands a surface sensitive technique to probe. Meanwhile, the stability of the surfaces under various conditions still needs more study before TIs can be further utilized. Low energy ion scattering (LEIS) is an extremely surface sensitive tool for investigating both surface structure and electronic properties. In this thesis, the spatial distribution of the filled topological surface states (TSS), halogen and Cs adsorption and reaction on Bi_2Se_3 and Bi_2Te_3 TI surfaces and heterostructures of bismuth bilayers on TIs are studied using LEIS and other surface analysis techniques.

TABLE OF CONTENTS

ACKNOWLEDGEMENTS iv
PUBLICATIONS AND PRESENTATIONS v
ABSTRACT OF THE DISSERTATION vi
TABLE OF CONTENTS vii
LIST OF FIGURES ix
LIST OF TABLES xiv
Chapter 1 1
1.1 Motivation 1
1.1.1 Topological Insulators 1
1.1.2 Adsorption and Reactions on $Bi_2(Se,Te)_3$ 5
1.1.3 Bismuth bilayers 5
1.2 Low Energy Ion Scattering 6
1.2.1 Binary Collision Approximation 6
1.2.2 Shadowing and Blocking 9
1.2.3 Resonant Charge Transfer 11
1.3 Experimental Techniques 16
1.3.1 Ultra-high Vacuum 16
1.3.2 Chamber setup 17
1.3.3 Time-of-flight Spectroscopy 19
1.3.4 Impact Collision Ion Scattering Spectroscopy 21
1.3.5 Low Energy Electron Diffraction 23
1.3.6 Surface Work Function 24
1.3.7 Atomic Force Microscopy 26
1.3.8 Halogen and Cs deposition 27
1.4 Single Crystal Growth and Surface Preparation Methods 29
1.5 Molecular Beam Epitaxy 30
Bibliography 34
Chapter 2 38
2.1 Introduction 38
2.2 Experimental Procedure 40
2.3 Results 43
2.4 Discussion 63
2.5 Conclusions 66
Bibliography 68
Chapter 3 73
3.1 Introduction 73
3.2 Experimental Procedure 76
3.3 Results and Discussion 77
3.4 Conclusions 85
Bibliography 86

Chapter 4 89
4.1 Introduction 89
4.2 Experimental Procedure 92
4.3 Results 95
4.4 Discussion 114
4.5 Conclusion 116
Bibliography 118
Chapter 5 123
5.1. Introduction 123
5.2 Experimental Procedure 125
5.3. Results and Discussion 128
5.4. Conclusions 143
Bibliography 144

LIST OF FIGURES

Figure 1.1. Calculated band structures for the family of $(Bi, Sb)_2(Se, Te)_3$ compounds. The topological surface states are the Dirac cone at the Γ points in Bi_2Se_3, Bi_2Te_3 and Sb_2Te_3, but are missing in Sb_2Se_3 as it is not a TI [10]. 2

Figure 1.2. Atomic structure of single crystal Bi_2Se_3. A quintuple layer with Se1–Bi1–Se2–Bi1–Se1 is indicated by the red square. Z is in [0001] direction [10]..... 3

Figure 1. 3. DFT simulation of the surface state charge distribution. The topological surface states are primarily located in the first quintuple layer [13]. 4

Figure 1. 4. Schematic of shadowing and blocking cones and the surface flux peak caused by focusing at the edge of shadow cones. 9

Figure 1. 5. TOF spectrum, after conversion to an energy scale, for normally incident 3.0 keV Na^+ scattered from Bi_2Se_3 cleaved at room temperature. The scattered projectiles were emitted at a polar angle of 35° with respect to the surface plane (scattering angle = 125°). The inset shows a schematic side view of Bi_2Se_3(0001) indicating the shadow (purple and green) and blocking (blue) cones for the orientation employed. The spectra show that only projectiles scattered from Bi sites are detected [45]. 10

Figure 1. 6. A diagram illustrating resonant charge transfer between an ion and a metal surface. When the ion gets closer to the surface, its s-level is broadened and shifted because of interactions with the conduction states in the metal and the image charge on the metal surface. The neutralization probability of the scattered particle is determined by the relative position of the local electronic potential and the ionization level at a close distance. 13

Figure 1. 7. Estimated NF of 3 keV Na^+ scattered from surface with different work functions (blue curve). The black dots are experimental values reported in this dissertation. 15

Figure 1.8. A schematic diagram showing the UHV chamber with the instrumentation used in this dissertation..... 18

Figure 1. 9. A schematic of the Time-of-Flight setup. 19

Figure 1.10. A schematic of the Comstock electrostatic analyzer..... 22

Figure 1. 11. ICISS simulations of the Se SSP intensity for 3 keV Na^+ scattering from Bi_2Se_3(0001) at different scattering and incident angles. 23

Figure 1. 12. A schematic of the instrumentation used to measure the surface work function with LEED optics. 24

Figure 1.13. A schematic of the AFM instrumentation using the reflection of a laser beam to measure displacement of the cantilever tip. 26

Figure 1. 14. A photograph of a solid-state electrochemical cell. 28

Figure 1. 15. Cross-sectional views of the three primary modes of thin-film growth (a) Volmer–Weber (VW: island formation), (b) Frank–van der Merwe (FM: layer-by-layer), and (c) Stranski–Krastanov (SK: layer-plus-island). Each mode is shown for several different surface coverages, Θ. 31

Figure 2. 1. AFM images collected from (a) an *in-situ* cleaved Bi_2Se_3 surface, and from Bi films grown on Bi_2Se_3 with evaporation times of (b) 2.5 min, (c) 3.5 min (d) 5.5 min and (e) 21 min, which lead to the indicated Bi coverages (see text), (f) 3 Bi BLs grown on Bi_2Se_3 and annealed at 120°C for 10 hrs, (g) height profiles of lines A, B and C that are drawn in (c), (d) and (e). 45

Figure 2. 2. LEED patterns collected from Bi_2Se_3 surfaces with the indicated Bi coverages. (d') is a close-up of the boxed area in (d). All of the LEED images were collected using a beam energy of 21.8 eV. 47

Figure 2. 3. Top layer lattice constant as a function of Bi coverage calculated using the length of line D in Fig. 2.2(b) and calibrated with the known Bi_2Se_3 lattice constant of 4.14 Å. 48

Figure 2. 4. LEIS TOF spectra collected from Bi_2Se_3 with the indicated Bi coverages. A 3.0 keV Na^+ ion beam is incident normal to sample surface and the detector is positioned at a scattering angle of 125°. In each spectrum, the black line represents total yield and red line represents the scattered neutral particles. The spectra are normalized to each other using the ion beam current measured on the sample and the data collection time so that they can be quantitatively compared. 51

Figure 2. 5. (a) Top view of a single Bi bilayer on a Bi_2Se_3(0001) surface. (b) Side view of the ($\mathbf{12\bar{1}}$0) plane of 1 Bi bilayer on Bi_2Se_3(0001). Representative shadow and blocking cones are indicated in (b). 52

Figure 2. 6. Neutral fractions of the Bi SSP for 3.0 keV Na^+ scattered from Bi_2Se_3 in both single and double alignment along with the Se:Bi ratio calculated from ion scattering data collected in single alignment, shown as a function of Bi coverage. 54

Figure 2. 7. Impact collision ion scattering spectroscopy (ICISS) polar angle scans and simulations for the Se (left panels) and Bi (right panels) SSPs collected from Bi_2Se_3 and

the 1 Bi BL covered surface using 3.0 keV Na^+ ions at a scattering angle of 161°. The sample rotates in the polar direction along the [**1010**] azimuth so that the ion incidence direction gradually varies from the surface plane to the surface normal. The surface flux peaks are indicated in upper panels. The legend in bottom right panel applies to all of the graphs. 56

Figure 2. 8. LEED patterns collected from 3 Bi BLs deposited on Bi_2Se_3 (a) before annealing, (b) after annealing at 120°C for 10 hrs, and (c) after annealing at 490°C for 0.5 hrs. 60

Figure 2. 9. LEIS TOF double alignment spectra collected using 3.0 keV Na^+ ions scattered from 3 Bi BLs deposited on a Bi_2Se_3(0001) surface and after annealing at the indicated temperatures for the indicated times. 62

Figure 3. 1. (a) A schematic of the Te and Bi atoms in the outermost atomic layers of single crystal Bi_2Te_3 shown along with the spatial distribution of the TSS electrons as suggested by calculations in the literature. The solid balls indicate the positively charged nuclei, while the cones indicate the electron clouds of the filled TSS, which accumulate below the Te and above the Bi atoms. The incoming ion beam and exit paths for singly scattered projectiles are shown. Note that the diagram is not drawn to scale. (b) A top view of the (001) surface showing the atoms in the first three atomic layers that are visible to the incoming ion beam along the surface normal. The [100] azimuthal direction along which the detector is place is also indicated. 74

Figure 3. 2. Typical TOF spectra collected for normally incident 3.0 keV Na^+ scattered from Bi_2Te_3 along the [100] azimuth at a scattering angle of 130°. The x-axis is shown in reverse, as smaller flight times indicate higher scattered energies. The solid line shows the scattered neutral projectiles, while the dashed line shows the total scattered yield. The neutral spectrum is multiplied by a factor of 5 for clarity. 79

Figure 3. 3. Neutral fractions of the Bi (circles) and Te (squares) SSPs (1) after the initial IBA preparation, (2) after 3 hrs of additional 1.0 keV Ar^+ sputtering, (3) after 9 hrs of additional Ar^+ sputtering, and (4) after 30 min of annealing at 340°C. 81

Figure 4. 1. LEIS total yield TOF spectra collected from (top) clean Bi_2Te_3, (middle) after 30 μA hrs of Br_2 exposure, and (bottom) post-annealing at 130 °C for 2 hrs. The 3.0 keV Na^+ ion beam is incident normal to sample surface and the detector is positioned at a scattering angle of 130°. The upper panels include top view schematics with projections of the azimuthal directions of the scattered beams, the atoms and their layer numbers indicated. The spectra in the left panel are collected along the (**1210**) azimuthal plane, which is a double alignment configuration. The spectra in the right panel are collected in single alignment by rotating the azimuthal angle with respect to the detector by 30°. The intensities of the spectra are normalized to each other using the ion beam current measured on the sample and the data collection time. 97

Figure 4. 2. 3.0 keV Na^+ LEIS spectra collected with the ESA from Bi_2Te_3 and the Ta sample holder following 40 μA hrs of Cl_2 exposure. The beam is incident at a 70° angle from the surface normal and the detector is positioned at a scattering angle of 40°. The spectra are offset vertically for clarity..... 102

Figure 4. 3. 3.0 keV Na^+ LEIS TOF spectra collected from surfaces of (left) 1.5 Bi BL covered Bi_2Te_3, and (right) after exposure to 10 μA hrs of Br_2. All of the spectra are collected in single alignment. The solid black lines show the total yield spectra of scattered projectiles, while shaded areas show spectra of the scattered neutral particles. 105

Figure 4. 4. LEED pattern collected from 1.5 Bi BL covered Bi_2Se_3 exposed to 6.7 μA hrs of Br_2. The image is collected using a beam energy of 21.8 eV and shows a $\mathbf{3 \times 3\ R30°}$ LEED pattern..... 109

Figure 4. 5. 3.0 keV Na^+ LEIS TOF spectra collected in double alignment from the surfaces of clean Bi_2Te_3 and after subsequent treatments as marked in the graph and described in the text. 112

Figure 4. 6. The proportion of Bi on the surface following cycles of halogen adsorption and annealing shown as a function of (a) Br_2 exposure and (b) Cl_2 exposure. The annealing is performed at a temperature of 130°C for 4 hrs with Br_2 etching of Bi/Bi_2Se_3, 2 hrs for Br_2 etching of Bi/Bi_2Te_3, 0.5 hrs for Cl_2 etching of Bi/Bi_2Se_3 and 2 hrs for Cl_2 etching of Bi/Bi_2Te_3. The horizontal dashed lines indicate the proportions measured from the clean bulk-terminated surfaces. Note that the error bars associated with many of points are smaller than the symbols. 113

Figure 5. 1. Work function of an IBA-prepared Bi_2Se_3 surface (solid triangles) and the Ta sample holder (solid circles) shown as a function of Cs exposure time. The inset is the same work function data, but instead given with respect to Cs coverage (see text). The dashed line illustrates the trend of the work function change as an aid to the eye and is not a fit to the data. 128

Figure 5. 2. TOF spectra of the scattered total yield and neutrals for 3.0 keV Na^+ in both double (left panel) and single (right panel) alignments before and after 0.07 ML of Cs is deposited onto Bi_2Se_3 surfaces that contain about 8% Se vacancies created by Ar^+ sputtering. The Na^+ ion beam is incident normal to sample surface and the detector is positioned at a scattering angle of 125° along the indicated azimuths. The spectra are normalized to the incident beam fluence. The insets to each panel show a schematic top view diagram of the crystal structure in which the atoms and their layer numbers are indicated along with projections of the azimuthal directions of the scattered beams. 132

Figure 5. 3. The measured work function with the samples held at room temperature shown as a function of time after various Cs depositions on IBA-prepared Bi_2Se_3. 137

Figure 5. 4. Se, Cs and Bi coverages and neutral fractions for 3.0 keV Na^+ singly scattered in single alignment from an IBA-prepared Bi_2Se_3 sample shown as a function of the initial Cs coverage. The points connected by solid lines were derived from LEIS spectra collected immediately after deposition, while the points connected by dashed lines are from data collected after the samples sat in the UHV chamber overnight (about 9 hrs) at room temperature. 139

LIST OF TABLES

Table 4. 1. Coverage of surface atoms calculated from ratios of the single scattering peak areas in LEIS TOF spectra collected in both double and single alignment orientations from Bi_2Te_3 and 1.5 Bi BL covered Bi_2Te_3 surfaces before and after exposure to Br_2 and Cl_2. No data is presented for chlorine coverages as the Cl SSP is not visible in the TOF spectra..... 100

Table 4. 2. The neutralization probability for 3.0 keV Na^+ singly scattered from Bi in a single alignment orientation from clean Bi_2Se_3, Bi_2Te_3 and these samples covered with 1.5 BL of Bi before and after 10 μA hrs exposures to Br_2 and Cl_2. 107

Chapter 1

Introduction

1.1 Motivation

1.1.1 Topological Insulators

A topological insulator (TI) material is an insulator in the surface or bulk but conducts along the edges or across the surface. The surface conductivity comes from the topological surface states (TSS), which have energy dispersion curves that connect the bulk conduction and valence bands, as shown in Fig. 1.1. Due to strong intrinsic spin-orbit coupling, the spins of the TSS charges are locked to their momentum, which is equivalent to the quantum spin hall effect without a magnetic field. Furthermore, with the protection of the spin-obit coupling, the spin carriers cannot backscatter from surface impurities, which brings up spin-transport and superconducting possibilities. Because of these nontrivial electronic properties, TIs are promising materials for future quantum computing, spintronics and other applications [1].

First generation, or two-dimensional (2D) TIs, are only conductive along the edges. They were originally predicted to exist in graphene [2] and in 2D semiconductor systems with a uniform strain gradient [3]. This behavior was subsequently predicted [4] and observed in HgCdTe quantum well structures [5].

Second generation, or three-dimensional (3D) TIs, are conductive across the surface but are insulators in the bulk material. They were predicted by three theoretical

groups independently [6-8]. Moore and Balents [7] induced the term "topological insulator" to describe this electronic phase. Fu and Kane predicted the topological phase in some real materials, including $Bi_{1-x}Sb_x$, which was first verified experimentally in 2008 [9]. The surface structure of $Bi_{1-x}Sb_x$ is rather complicated and the band gap is small. This motivated a search for topological insulators with a larger band gap and simpler surface structure. In 2009, 3D topological insulators, including Bi_2Se_3 and Bi_2Te_3, were identified both experimentally and theoretically [10-12]. ARPES data directly show the TSS with a spin-polarized Dirac cone, as displayed in Fig. 1.1. Since then, studies of topological materials have been getting more popular and many papers have been published each year.

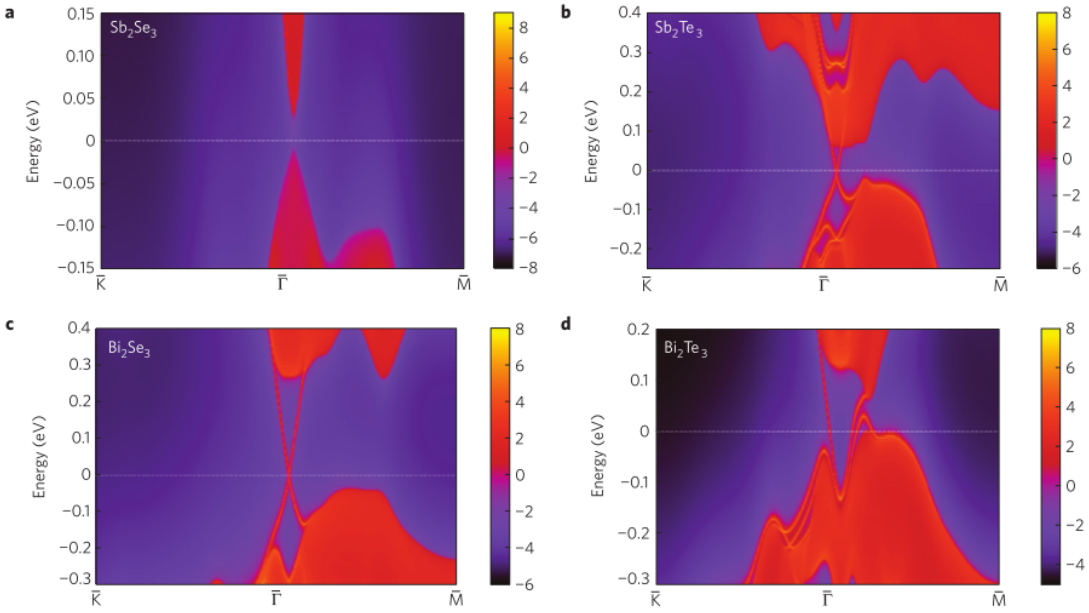

Figure 1.1. Calculated band structures for the family of $(Bi, Sb)_2(Se, Te)_3$ compounds. The topological surface states are the Dirac cone at the Γ points in Bi_2Se_3, Bi_2Te_3 and Sb_2Te_3, but are missing in Sb_2Se_3 as it is not a TI [10].

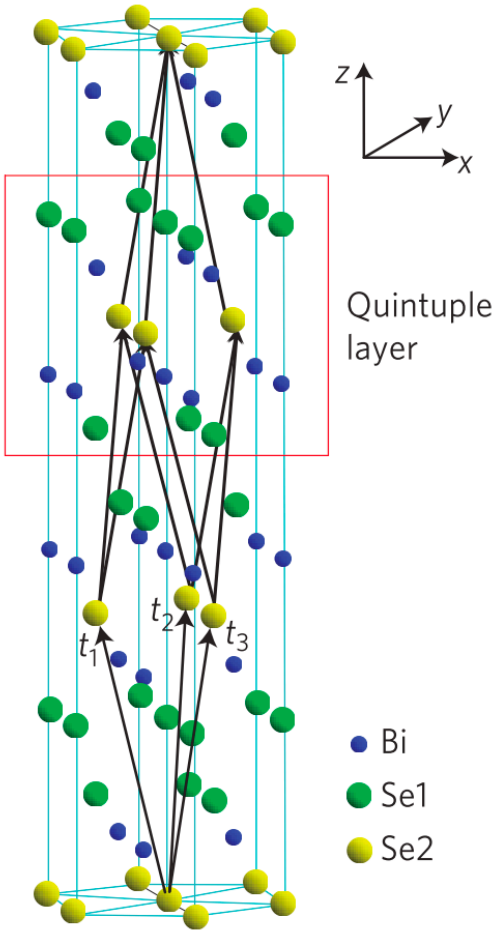

Figure 1.2. Atomic structure of single crystal Bi_2Se_3. A quintuple layer with Se1–Bi1–Se2–Bi1–Se1 is indicated by the red square. Z is in [0001] direction [10].

Bi_2Se_3 is the most well-known and promising TI material as it has a very clear Dirac cone and a large band gap (0.35 eV), which makes room temperature spintronics or quantum computation possible. Bi_2Te_3 had been investigated as a thermoelectric (TE) material for a long time before it was studied as a TI, but its band gap is smaller (0.21 eV) and the Dirac point is buried in the valence band. Both Bi_2Se_3 and Bi_2Te_3 are 3D TIs and they share very similar crystal structures. They have the same rhombohedral structure with

space group $D_{3d}^{5}(R\bar{3}m)$. The crystal is a layered material comprised of stacked quintuple layers consisting of Se(Te)-Bi-Se(Te)-Bi-Se(Te) layers in the [0001] direction with each of the quintuple layers connected to each other by weak Van de Waals forces.

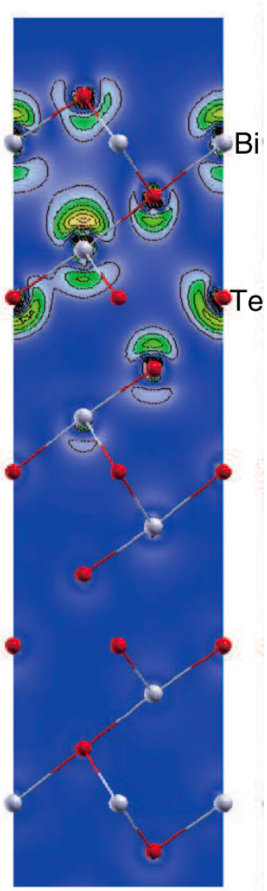

Figure 1. 3. DFT simulation of the surface state charge distribution. The topological surface states are primarily located in the first quintuple layer [13].

First principles calculations predict that the charges of the TSS are located within the outermost QL and are accumulated below the first layer Te atoms and above the second layer Bi atoms, as shown in Fig 1.3 [13-15]. There was, however, no experimental verification of this prior to the work presented in Chapter 3 of this dissertation [16].

1.1.2 Adsorption and Reactions on $Bi_2(Se,Te)_3$

Adsorption of various species on TIs has been extensively studied [17,18]. It is predicted that the TSS would be protected by time-reversal symmetry after adsorption of nonmagnetic atoms or molecules [19,20]. One use of surface adsorption is to tune the Fermi level to a desired position, such as the Dirac point. In addition, adsorption and reactions on TI surfaces may cause a change in the atomic structure and thus their electronic properties. The Fermi level of Bi_2Se_3 is often found to spontaneously shift up over time, also known as the aging effect, which is believed to be related to the formation of Se vacancies caused by surface reactions [21,22]. It is thus interesting to study the behavior of atoms and molecules adsorbed on TI surfaces. Alkali atom adsorption on TIs has been studied extensively as a means to modify the electronic structure [23-26]. Reactions of $Bi_2(Se,Te)_3$ with O_2 and H_2O have also been investigated extensively [20,27-29]. Reactions of halogens with $Bi_2(Se,Te)_3$ surfaces have not been reported prior to the work presented in Chapter 2 of this dissertation [30].

1.1.3 Bismuth bilayers

A single Bi(0001) bilayer (BL) is reported to be a 2D topological insulator [31,32]. Hetero-structures of Bi BLs and other materials are thus becoming a popular means for producing materials with novel transport properties [33-35]. Bi BL-terminated Bi_2Se_3 surfaces show giant Rashba-split states [36-38] and are predicted to have lower surface energy than a bare Se-terminated surface, an idea that is supported by density functional theory (DFT) [39,40] and experimental results for Bi BL deposition on *in-situ* [40] and *ex-*

situ [41] cleaved Bi_2Se_3 surfaces. Therefore, it is interesting to explore the structure and stability of Bi BLs on TI surfaces.

1.2 Low Energy Ion Scattering

Low Energy Ion Scattering (LEIS) is a surface sensitive technique that provides the atomic composition, structure and even electronic information about the first few atomic layers of a material [42-44]. It is thus an important tool for investigating the structure and electronic properties of TI materials and reactions on the TI surfaces since their novel electronic states are confined to the outermost atomic layers. Low energy ions are defined as those with kinetic energies in range of 0.5 to 10 keV.

1.2.1 Binary Collision Approximation

The interactions of low energy ions with a solid can be approximated as a series of classical binary scattering events between the projectile and individual atoms, which is known as the binary collision approximation (BCA). In addition, some inelastic interactions will occur with the electrons in the target, which lead to phenomena such as energy loss and charge exchange. The speed of low energy Na^+ projectiles is in the range of 6.5 to 290 km/s, which corresponds to de Broglie wavelengths up to 0.027 Å. Thus, relativistic effects and diffraction can be ignored.

The energy of a scattered particle following a single binary elastic collision can be calculated using energy and momentum conservation as

$$E_f = E_i \left(\frac{\cos\theta + \sqrt{\left(\frac{m_t}{m_p}\right)^2 - \sin^2\theta}}{1 + m_t/m_p}\right)^2 \qquad (m_t > m_p) \qquad \text{----- (1.1)}$$

where θ is the scattering angle, m_p and m_t are the masses of projectile and target atoms, respectively, and E_i and E_f are the energies of the projectile before and after scattering, respectively. In the limit of complete backscattering, when $\theta = 180°, E_f = E_i \left(\frac{m_t - m_p}{(m_t + m_p)}\right)^2$.

The prevalent features in LEIS spectra are single scattering peaks (SSPs) that correspond to projectiles that have made only one collision with a target atom that causes them to scatter directly into the detector. Equation 1.1 can then be used to determine the mass of the target atom from the energy of the SSP. In this way, LEIS spectra provide a mass spectrum of the surface region. As an example, the spectrum shown in Fig. 1.5 show the SSP for Na scattered from surface Bi.

The collisions can be described by a pure Coulombic force only for high energy (MeV) projectiles, however, due to screening from the electrons at lower (keV) energies, so that the interaction potential falls off faster than 1/r. The most widely used potentials in the low energy regime may be considered as a Coulombic term (1/r) multiplied by a screening function, such as

$$V(r) = \left(\frac{Z_1 Z_2 e^2}{4\pi\epsilon r}\right)\phi\left(\frac{r}{a}\right) \quad \text{----- (1.2)}$$

Here a represents the "screening length". The screening function $\phi(\frac{r}{a})$ gives good results when Moliere approximation is applied to Thomas-Fermi model (TFM) [42], which is

$$\phi\left(\frac{r}{a}\right) = \phi(X) = 0.35e^{-0.3X} + 0.55e^{-1.2X} + 0.1e^{-6.0X} \quad \text{----- (1.3)}$$

This screening length is normally reduced by a factor C, which is typically in the range of 0.6 to 0.8, to provide a better match to experimental data. C can alternatively be estimated as [42]

$$C = 0.54 + 0.045(\sqrt{Z_1} + \sqrt{Z_2}) \quad \text{----- (1.4)}$$

An important parameter in LEIS is the differential cross-section for each scattering event, which depends on the projectile kinetic energy, projectile and target masses and scattering angle [42]. The number of scattered projectiles measured with a detector that has a fixed acceptance angle is proportional to the differential cross-section. Thus, the differential cross-section should be taken into consideration for peak intensity normalization. It can be calculated using various potentials and values for C via the link at http://www.iap.tuwien.ac.at/www/surface/leis.

1.2.2 Shadowing and Blocking

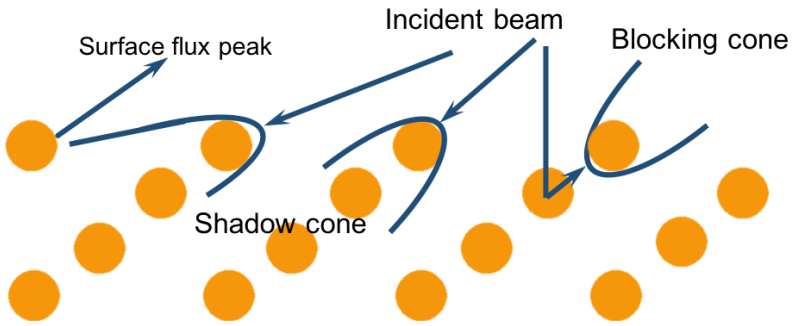

Figure 1. 4. Schematic of shadowing and blocking cones and the surface flux peak caused by focusing at the edge of shadow cones.

Shadowing and blocking in LEIS can be understood with the use of Fig. 1.4. A shadow cone is the region behind a surface atom from which the incident projectiles are excluded due to scattering. A blocking cone is the region above a surface atom in which outgoing scattered projectiles are excluded from reaching the detector due to scattering. The shadow and blocking cones become larger with a smaller ion kinetic energy or a larger target atom radius. As an example, for 3 keV Na^+ shadowed by a Se atom, the shadow cone has a radius of ~1.5 Å.

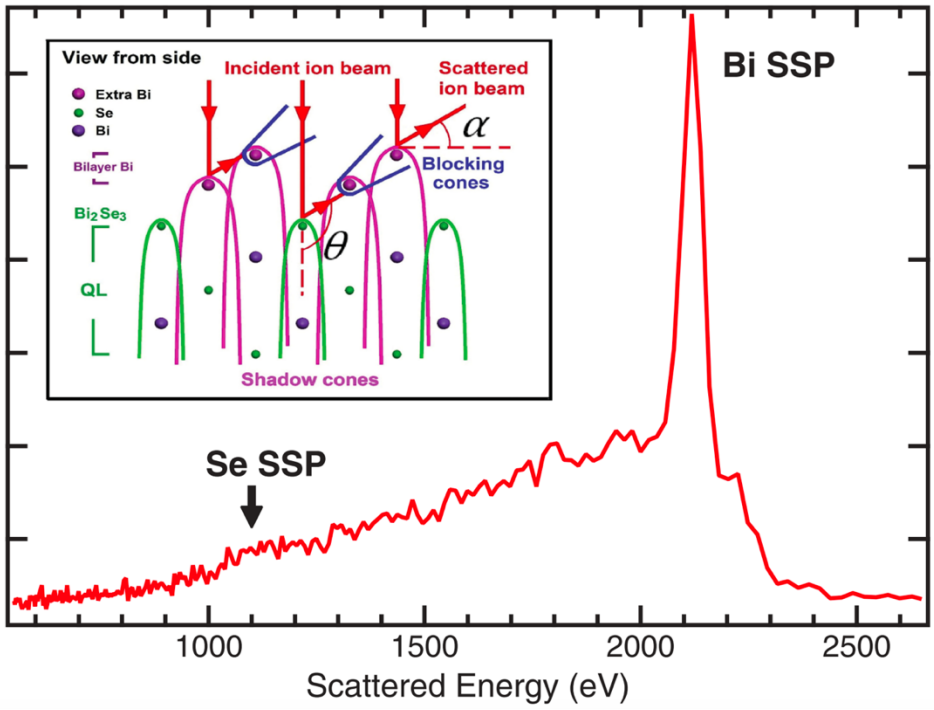

Figure 1. 5. TOF spectrum, after conversion to an energy scale, for normally incident 3.0 keV Na^+ scattered from Bi_2Se_3 cleaved at room temperature. The scattered projectiles were emitted at a polar angle of 35° with respect to the surface plane (scattering angle = 125°). The inset shows a schematic side view of Bi_2Se_3(0001) indicating the shadow (purple and green) and blocking (blue) cones for the orientation employed. The spectra show that only projectiles scattered from Bi sites are detected [45].

By choosing specific angles of incidence and emission, shadowing and blocking can be used to emphasize scattering from specific surface atoms. For example, aligning both the ion beam and detector along low index directions, which is referred as double alignment, can produce spectra in which only the outermost surface atoms are detected. Figure 1.5 shows a TOF-LEIS spectrum in which the incident ion beam is normal to the surface and the detector is aligned along a different low index direction. The inset to the figure shows that only the top three layers of atoms can be directly impacted by the ion

beam due to shadowing, while any projectiles scattered from the 2nd or 3rd atomic layer are blocked from reaching the detector by 1st and 2nd layer atoms. Thus, single scattering can only occur from the outermost atoms. In contrast, if the detector is set at a random direction while maintaining normal incidence, which would be a single alignment configuration, then the top three layers of atoms are detected.

In addition, measuring the yield of singly scattered projectiles as a function of incident or emission angle can be used to determine the quantitative surface atomic structure and lattice parameters of single crystal surfaces [42]. When the incident beam is oriented such that the edges of a shadow cone of one surface atom intersect a neighboring atom, a sharp increase of the scattering intensity is observed, which is called a flux peak in an angular scan. A surface flux peak is created at a critical incident angle when the enhancement is due to two atoms in the same atomic layer. A specialized form of angular resolved LEIS used in this dissertation is impact collision ion scattering spectroscopy (ICISS) in which the ion source and detector, i.e., the scattering angle, are fixed while the sample is rotated [46].

1.2.3 Resonant Charge Transfer

When an alkali atom or ion is in the vicinity of a solid surface, such as occurs during LEIS, electron can tunnel between the alkali and the solid, which can be explained with the resonant charge transfer (RCT) model. As indicated by Fig. 1.6, when the alkali approaches the surface, the ionization level (3s for Na^+) shifts up due to the interaction with its image charge. An estimate for the magnitude of this shift is given by [47]

$$\Delta E(z) = \frac{1}{\sqrt{\frac{1}{{v_{max}}^2} + \frac{16z^2}{e^4}}} \quad \text{----- (1.5)}$$

Here, z is the distance between the alkali and the surface and v_{max} is a parameter used to define the saturation value at z = 0. This equation shows that the energy shifts up when z reduces. In reality, however, the shifting saturates when z reaches 0 due to higher order effects from the structure of the surface. As an example of a typical value, v_{max}= 2.6 eV is used for Cu(001) [48]. For Na with an ionization level at -5.14 eV, its s level will be at -4.05 eV when it is 3 Å away from a Cu(001) surface.

In addition to shifting, the level also broadens due to hybridization of the s level with the states in the surface. The following empirical equation, given in Ref. [47], can be used to conveniently estimate the magnitude of the broadening,

$$\Delta(z) = \Delta_0/(e^{4\alpha z} + \left(\frac{\Delta_0}{\Delta_{sat}}\right)^4 - 1)^{1/4} \quad \text{----- (1.6)}$$

The halfwidth of the level, Δ, increases as z approaches 0 and it saturates at Δ_{sat}. Δ_0 and Δ_{sat} can be derived by fitting to Nordlander and Tully's calculation [49]. Since Li 2s and Na 3s have very similar broadening curves, values from Marston's paper [47] is used for this estimate, i.e., Δ_0= 2.23 a.u., Δ_{sat}= 0.04 a. u. and $\alpha = 0.86$. Using this method, it is estimated that the halfwidth of the 3s level of Na at 3 Å from the surface is 0.42 eV.

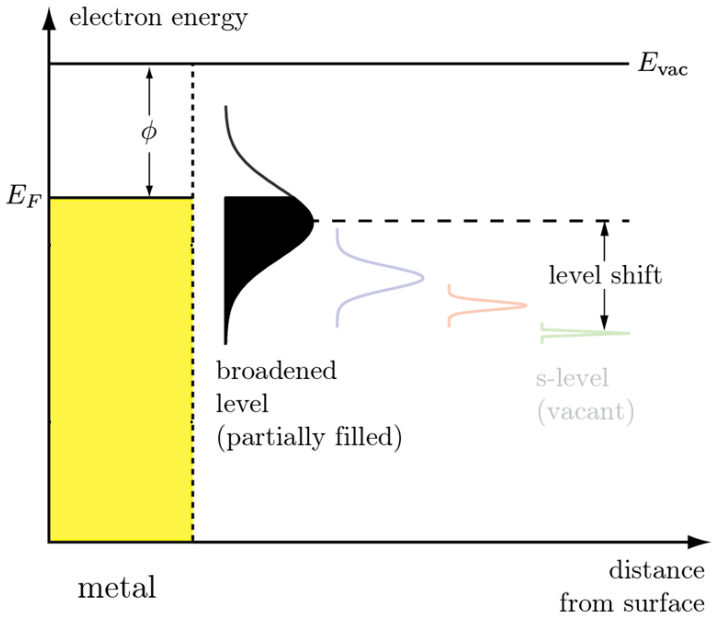

Figure 1. 6. A diagram illustrating resonant charge transfer between an ion and a metal surface. When the ion gets closer to the surface, its s-level is broadened and shifted because of interactions with the conduction states in the metal and the image charge on the metal surface. The neutralization probability of the scattered particle is determined by the relative position of the local electronic potential and the ionization level at a close distance.

After a low energy alkali projectile collides with a surface, it exits with speed v and electrons continue to tunnel to and from the solid until the projectile is far enough away from the surface so that tunneling can no longer occur. Due to the strong coupling between the states of the solid and the projectile, the projectile quickly loses its memory of its initial charge state. The tunneling rate decays quickly with the increase of the particle's distance from the surface and becomes zero when z is large (a few Å). This process happens quickly (less than 10 fs) so that the overlapping levels are never in equilibrium, making the neutralization of scattered alkali ions a nonadiabatic process. Because of this, the neutralization probability, or neutral fraction (NF), is determined along the exit trajectory

of the projectiles. The expected NF can be calculated by first order perturbation theory (Fermi's golden rule) [50], but it can also be determined statically by the degree of overlap of the filled states in the solid with the broadened energy level of the outgoing projectile at an effective "freezing distance", Z_{fr} [51]. The freezing distance can be roughly estimated by the empirical formula [52]

$$Z_{fr} = \frac{1}{\alpha} ln(\frac{2\Delta_0}{\alpha v_\perp}) \quad \text{----- (1.7)}$$

Z_{fr} increases as the perpendicular component of the exit velocity, $v_\perp$, decreases. Plugging in the numbers above, the freezing distance of a 1.0 or 2.0 keV Na atom will be 3.0 or 2.7 Å, respectively.

Assuming that the shape of the broadened level is Gaussian, then the overlapping area between the states in solids and the broadened level at the freezing distance is the neutralization probability. It can be shown that

$$\sigma = \Delta(Z_{fr})/\sqrt{2ln2} \quad \text{----- (1.8)}$$

$$\mu = \mathrm{I} + \Delta E(Z_{fr}) \quad \text{----- (1.9)}$$

$$\mathrm{NF} = \int_{-\infty}^{-\phi} \frac{1}{\sigma\sqrt{2\pi}} e^{-\frac{1}{2}\left(\frac{-\phi-\mu}{\sigma}\right)^2} d\phi = \frac{1}{2} + \frac{1}{2} erf(\frac{\phi-\mu}{\sigma\sqrt{2}}) \quad \text{----- (1.10)}$$

where Φ is the work function of the solid and the μ is the shifted energy level of the projectile. Figure 1.7 shows the relationship of the NF and the work function using μ

= -4.05 eV and $\Delta(Z_{fr})$ = 0.42 eV. As the figure indicates, the higher the work function of the target surface, the lower the neutralization probability will be. Most of measured NFs in this dissertation follow this trend, as shown by the experimental data in the figure. A discrepancy between the NFs at the same work function can also observed, however, which implies that such surface do not have a homogenous potential so that local effects are involved in the neutralization process. A detailed discussion about local effects is given in Chapter 3.

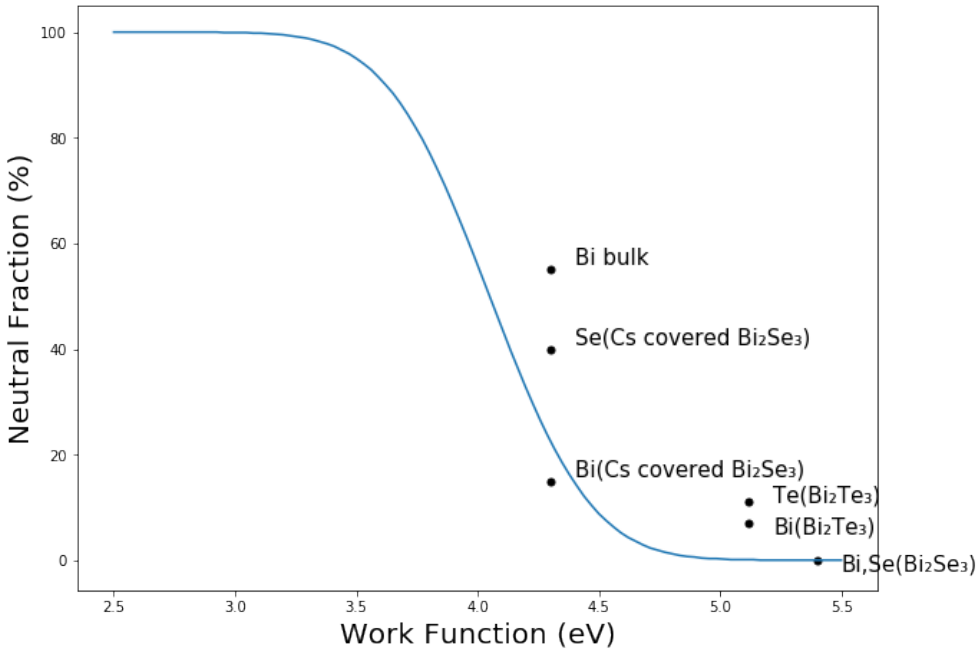

Figure 1. 7. Estimated NF of 3 keV Na^+ scattered from surface with different work functions (blue curve). The black dots are experimental values reported in this dissertation.

1.3 Experimental Techniques

1.3.1 Ultra-high Vacuum

Ultra-high vacuum (UHV) is defined as a pressure lower than ~10^{-9} Torr. UHV is crucial to surface science research as it is required to keep surfaces clean and allow the transmission of molecular, electron or ion beams when using techniques such as molecular beam epitaxy (MBE), x-ray photoelectron spectroscopy (XPS) or LEIS.

An estimate of the adsorption of residual gases onto sample surfaces in an UHV chamber can be performed by assuming that the gases are ideal. After an UHV chamber is baked to remove water and hydrocarbon adsorbates from the inner walls, the main gasses remaining inside the chamber are hydrogen and CO. According to the Maxwell Boltzmann distribution, the average velocity for hydrogen is:

$$\bar{v} = \sqrt{8RT/\pi M} \qquad \text{----- (1.11)}$$

where R = 8.3 J mol^{-1} K^{-1} is the universal gas constant, T is the absolute temperature, and M is the molecular weight of the gas. Using 300 K for T and M = 0.002 kg/mol for hydrogen, the average velocity would be 1780 m/s.

The mean free path of a gas molecule before it collides with another molecule is:

$$\lambda = \frac{RT}{\sqrt{2}\pi d^2 P N_A} \qquad \text{----- (1.12)}$$

where d is a variable that approximates the diameter of an ideal gas molecule and N_A is Avogadro's number, 6.02×10^{23}. Using 2.9 Å for the diameter of a hydrogen molecule and 1×10^{-9} Torr for the pressure, the mean free path of H_2 is 83 km! Thus, background gases would hardly interact with ion or electron beams.

The collision frequency with the chamber walls is given by

$$\Gamma = \frac{PN_A}{\sqrt{2\pi MRT}} \quad \text{----- (1.13)}$$

For hydrogen, the collision frequency is 1.4×10^{12} cm^{-2} s^{-1}. The atomic density on a sample surface is typically ~10^{15} cm^{-2}. Assuming that the sticking coefficient is 100%, the time it would take for a monolayer to adsorb is about 12 min at a vacuum of 1×10^{-9} Torr. For this reason, the pressure for surface studies needs to be closer to 1×10^{-10} Torr to reduce the level of contamination formed on the surfaces during measurements.

1.3.2 Chamber setup

Figure 1.8 shows a schematic diagram of the two-level UHV main chamber, the attached molecular beam epitaxy (MBE) chamber and a load-lock chamber for sample introduction. The main chamber has a base pressure of 2×10^{-10} Torr, the MBE chamber 7×10^{-10} Torr and the load-lock chamber 1×10^{-8} Torr. The main chamber contains low energy electron diffraction (LEED) optics (Princeton Research Instruments), a thermionic emission alkali ion gun (Kimball Physics) mounted on a turntable, an ion sputter gun (Perkin-Elmer), a Comstock Electrostatic Analyzer (ESA), a 0.5 m long TOF leg and

sapphire leak valves that can admit controlled amounts of argon, oxygen and other gases into the chamber.

The sample is mounted on the foot of an x-y-z manipulator in the main chamber that can be rotated both azimuthally and polarly. A 0.008" thick tungsten filament is mounted behind the sample holder for electron beam heating the sample up to 1200°C. The load-lock chamber has a Thermionics sample transfer system so that samples can be inserted without venting the main chamber. The MBE chamber currently has Bi and Te evaporators and a quartz crystal microbalance (QCM) thickness monitor installed. Samples can be transferred between the MBE and main chambers while remaining under UHV.

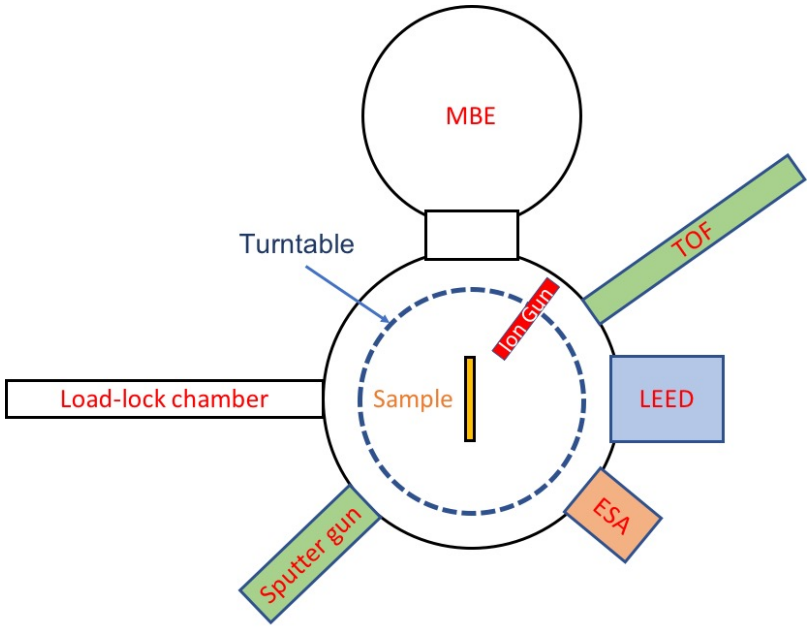

Figure 1.8. A schematic diagram showing the UHV chamber with the instrumentation used in this dissertation.

1.3.3 Time-of-flight Spectroscopy

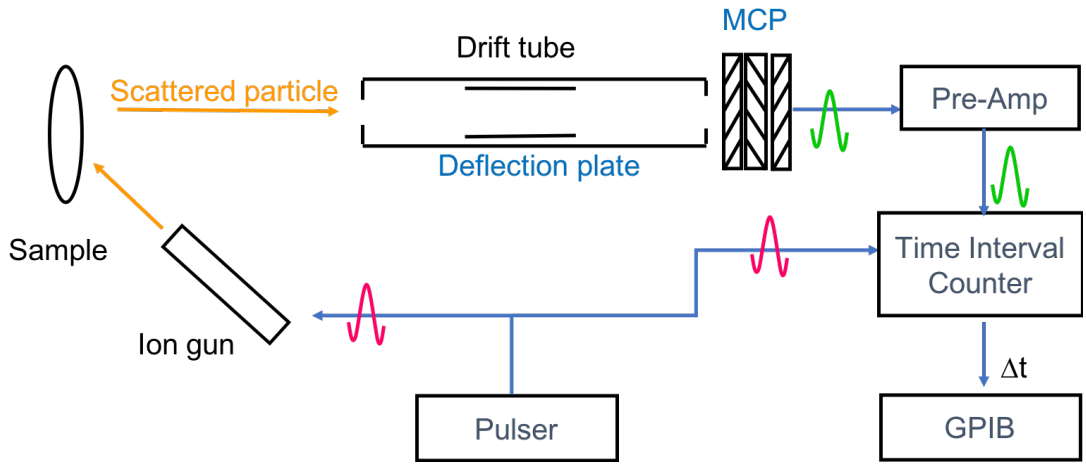

Figure 1. 9. A schematic of the Time-of-Flight setup.

Time-of-flight (TOF) spectroscopy measures the flight time of scattered projectiles. Figure 1.9 is a schematic of the TOF setup. A pulse generator (Avtech) sends pulse signals to both the ion gun and the universal time interval counter (Stanford Research Systems). High voltage pulses are sent to the gun, as described below, while a TTL pulse is sent to the time interval counter.

The ion gun can be used in either a continuous or a pulsed mode. Four deflection plates, labeled X+ , X- , Y+ and Y-, are located between the ion gun and in front of a 1 mm diameter aperture. These are used to control the direction of the outcoming ions. In the continuous mode, the beam is tuned by applying a voltage (usually less than 200 V) to X+, Y+ and leaving X- and Y- at 0 V in order to get the ions to pass through the aperture. The pulsed mode is used for TOF measurements. The pulse generator sends a bipolar and a unipolar pulse of about 150 V to X- and Y-, so that the ion beam follows a square pattern that passes through the aperture. Ions are emitted only when the rising edge of X- hits 0 V

and Y- is at 0 V. The width of the ion pulse is about 40 ns, which determines the resolution of the TOF spectra. The width can be adjusted through a potentiometer attached to the X- output that slows the rise time of the pulse.

The backscattered projectiles travel through a double 3 mm aperture in a 0.57 m long flight tube and hit the triple microchannel plate (MCP) detector, which is attached to a discriminator/preamplifier that sends a TTL signal to the time interval counter. The front of the MCP is held at ground potential so that it has the same detection efficiency for both scattered ions and neutrals. The absolute detection efficiency quickly decreases when the kinetic energy of the projectiles falls below about 1 keV [53]. Two parallel metal deflection plates are installed in the drift tube. When 400 V is applied across the plates, the ions will be deflected away so that only neutral particles can reach the MCP detector. The voltage on the plates is switched on and off periodically (typically every 60 s), in order to collect total and neutral spectra at the same time thus eliminating any effects that could be caused by the ion beam flux changing over a long period of time.

The time interval counter calculates the time interval between the MCP and pulse generator signals and sends the data to a computer through a GPIB interface. The TOF spectra are a histogram of these time intervals collected over a sufficient period of time to obtain good statistics.

The pulse frequency is set at 100 kHz, so that each measurement cycle has a period of 10 μs. With a typical sample current of 30 pA, the signal rate is about 100 counts s^{-1}. Therefore, the probability for two scattered particles to reach the detector in a single measurement cycle is very small and the detector dead time (~0.1 μs) can be ignored.

Surface damage is a concern in LEIS measurements, as each collision will irreversibly remove one to ten surface atoms. Since the density of surface atoms is on the order of 10^{15} cm^{-2}, the damage can be maintained under 1% of a monolayer for a beam size of 1 mm^2 by limiting the data acquisition time to less than 30 min before re-preparing the sample.

1.3.4 Impact Collision Ion Scattering Spectroscopy

Impact collision ion scattering spectroscopy (ICISS) was developed in the 1980s by Aono and coworkers [54]. ICISS measures the scattering yield as a function of incident angle while keep the scattering angle fixed. Ideally, the scattering angle would be set at 180° to make analysis easier, but the size of the ion gun limits the angle that can be obtained. Thus, the scattering angle is set at about 160° for the ICISS data collected in this dissertation.

The ICISS spectra are collected with a Comstock electrostatic analyzer (ESA). Figure 1.10 is a schematic of the analyzer. It is composed of an Einzel lens for focusing at the entrance, two hemispherical plates for energy selection and a dual MCP detector at the end. Voltages are applied to the hemispherical plates and the trajectory of incident ions are bent by the electric field, which creates an energy filter that only allows charged particles within a certain energy window, called the pass energy, to reach the MCP detector. The energy resolution is determined by the value of the pass energy and size of the apertures installed inside the ESA.

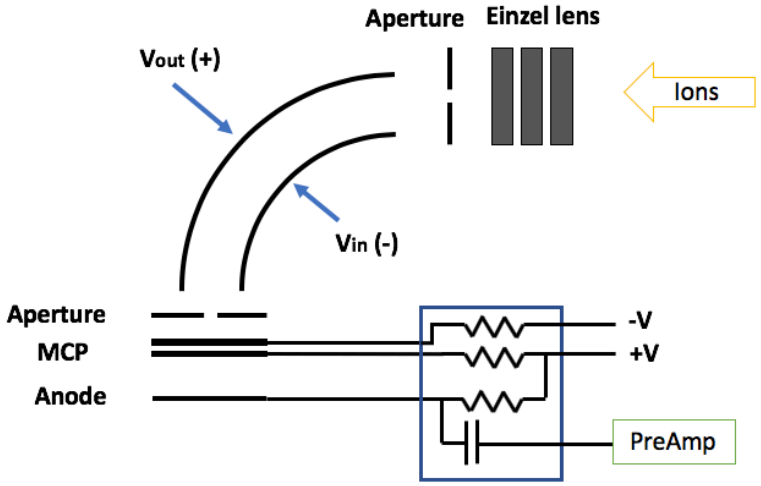

Figure 1.10. A schematic of the Comstock electrostatic analyzer.

The most notable features in ICISS angular scans are the flux peaks that occur when the edges of a shadow cone hit a neighboring atom. Analysis of the positions of the flux peaks provide information about the angle and distance between the two neighboring atoms. The ICISS spectra can be quasi-fit by simulations employing molecular dynamics (MD), although these simulations do not capture the multiple scattering background. Figure 1.11 is an example of a simulated map of ICISS at various scattering angles produced with the Kalypso software package [55]. As shown in the figure, the surface flux peak is always at an incident angle of 10º since it is determined only by the angle of the incident ion beam with respect to the surface, while flux peaks originating from deeper atomic layers vary with scattering angle as they also depend on the exit angle.

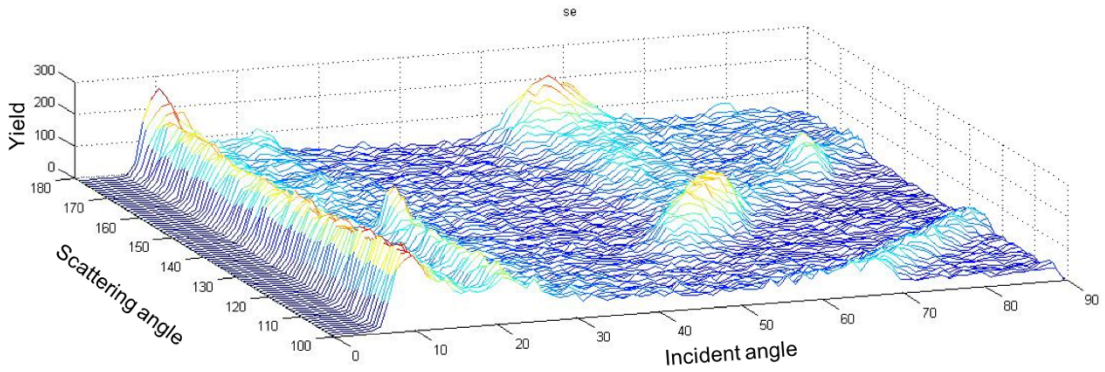

Figure 1. 11. ICISS simulations of the Se SSP intensity for 3 keV Na^+ scattering from Bi_2Se_3(0001) at different scattering and incident angles.

1.3.5 Low Energy Electron Diffraction

Low energy electron diffraction (LEED) is one of the most commonly used techniques in surface studies. It utilizes the wave properties of low energy electrons to provide images that represent the periodicity of the surface structure in reciprocal space. Typically, LEED uses electrons with kinetic energies from 20 to 150 eV. According to the de Broglie formula, the wavelength of an electron can be estimated as

$$\lambda\,[nm] = \frac{h}{\sqrt{2mE}} \approx \sqrt{\frac{1.5}{E(eV)}} \qquad \text{----- (1.14)}$$

The wavelength of the electrons used in LEED are around 1 to 3 Å, which is comparable to the distance between atoms in solids. The penetration depth of low energy electron is around 5 atomic layers and thus it's more sensitive to the atomic structure in the surface

region than X-ray diffraction. The position of LEED spots shows the size, symmetry and orientation of the surface unit cells. The sharpness and intensity of LEED spots reflect the cleanness of the surface and the crystal grain size. By monitoring the intensity of the LEED spots versus the electron energy, which is called an I-V curve, the atomic structure of the top few atomic layers can be determined [56,57].

1.3.6 Surface Work Function

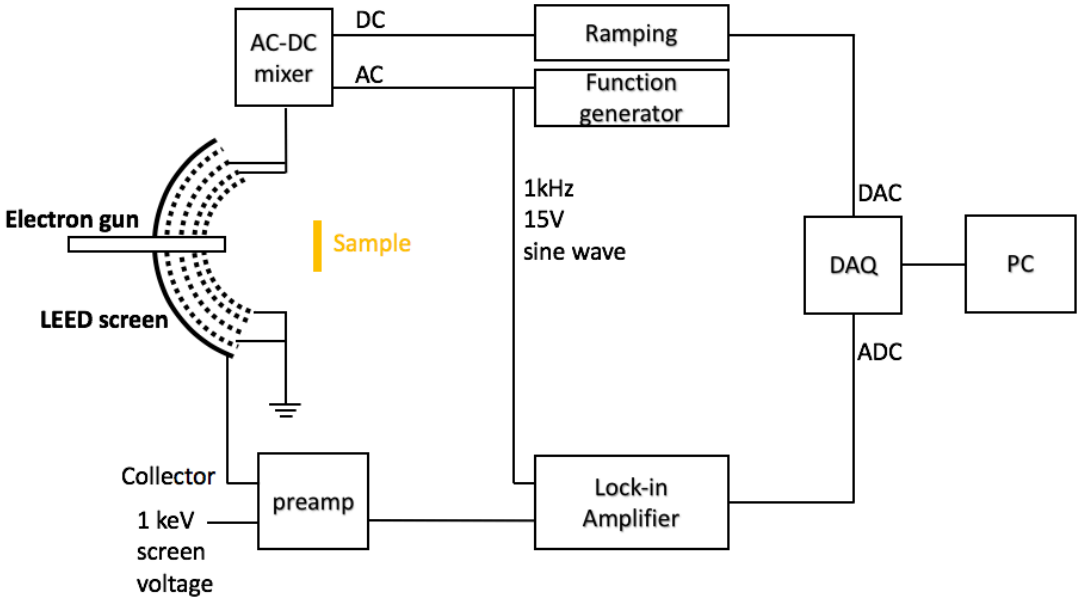

Figure 1. 12. A schematic of the instrumentation used to measure the surface work function with LEED optics.

Changes to the surface work function (WF) are measured by monitoring the position of the secondary electron cutoff when the sample is bombarded with low energy electrons. The measurements are performed with the LEED optics, with a schematic of the

connections shown in Fig. 1.12. The sample is biased with -20 V, so that the all the secondary electrons have enough kinetic energy to overcome any effects of the Earth's magnetic field. The LEED optics contain an electron gun, a 4-grid retarding filter and an electron collector. An electron beam energy of 200 eV is used to create a large number of secondary electrons while not damaging the sample. Grids 1 and 4 are grounded, while a voltage applied to both grids 2 and 3 acts as a high-pass filter to block electrons with lower kinetic energy from passing through. The sum of a ramped DC and a small AC voltage is placed on those grids to modulate the signal of electrons around the DC value. A lock-in amplifier is used to resolve the small signal of scattered electrons from the background, and thus produces a derivative spectrum of the emitted electrons. The measured secondary electron current is $I\big(V + V_0 sin(\omega t)\big)$ plus a noise term. If the current is Taylor expanded, it will be

$$I\big(V + V_0 sin(\omega t)\big) = I(V) + I'(V)V_0 sin(\omega t) + O(I'') \quad \text{----- (1.15)}$$

After Fourier integration, only the differential part remains, which is the number of emitted electrons at that energy. The emitted electron current has a cutoff at a voltage that represents the lowest possible kinetic energy of emitted electrons plus the bias voltage, which changes linearly with the WF. The measured cutoff voltage is related to the sample bias, and the WF of the analyzer as

$$E_{cutoff} = V_{bias} + WF_{sample} - WF_{analyzer} \quad \text{----- (1.16)}$$

The sample bias and WF of the analyzer are thus treated as a constant offset. This technique can only provide changes to the WF as the sample is modified, so that a surface with a known work function is used as a calibration to determine the absolute value.

1.3.7 Atomic Force Microscopy

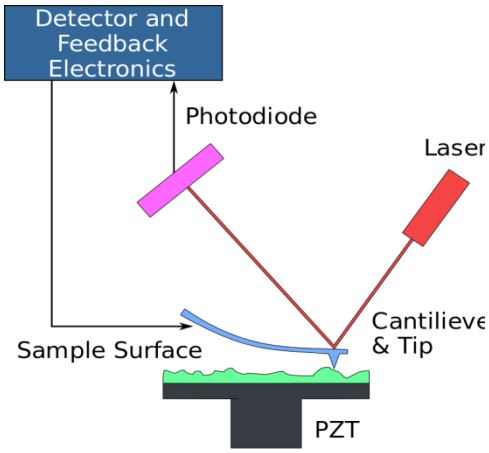

Figure 1.13. A schematic of the AFM instrumentation using the reflection of a laser beam to measure displacement of the cantilever tip.

Atomic force microscopy (AFM) is used to plot the surface topography on the atomic scale. Figure 1.13 shows a schematic of an AFM instrument. A tip, placed close to the sample surface, is driven to vibrate at a certain frequency by an external force. A laser beam reflecting from the tip is used to monitor the displacement or frequency change of the tip. The piezoelectric (PZT) is used to adjust the position of the tip on the sample and the distance between the sample and tip.

An AFM can be used in different ways such as contact mode, non-contact mode and tapping mode. For all of the experiments in this thesis, the tapping mode is used. When the tip is close to sample surface, the vibration frequency will change due to forces caused by interactions such as mechanical contact, van der Waals force, capillary force, electrostatics, magnetism, Casimir forces, solvation forces, etc. The feedback electronics adjusts the sample height to restore the vibration frequency and thus maintain the tip at a constant distance above the surface. By mapping the sample displacement over x and y, the topography of the sample surface can then be plotted. Usually, the height resolution obtained is better than 1 Å, while the lateral resolution is around several nanometers.

The AFM measurements in this dissertation were conducted in the Center for Nanoscale Science & Engineering at UC Riverside. The images were collected in air at room temperature in tapping mode using a Dimension 3000 AFM (Digital Instruments) with TESPA-V2 silicon tips (Bruker).

1.3.8 Halogen and Cs deposition

A solid-state electrochemical cell is used to deposit halogen molecules in UHV [58,59]. Figure 1.14 is a photograph of the solid-state electrochemical cell. A silver-halide pellet is the source of halogen molecules, which is mounted above a piece of Ag metal. During operation, the cells are heated to approximately 120°C to enable ionic conduction through the pellet. An electrochemical reaction causes the silver-halide to dissociate and form Ag metal and negative halogen ions that transport to the surface of the cell. The cell is operated by placing a voltage across the pellet so that a current of about 10 μA of halogen

ions is produced. When the halogen ions reach the surface of the pellet, they combine to form molecules that are emitted into vacuum. The exposures are reported in terms of the cell current integrated over time and given in units of μA hrs. The coverage of halogen molecules can be calibrated by LEIS spectra, and the exposure amount is considered to be saturated when LEIS spectra do not change with additional halogen exposure.

Figure 1. 14. A photograph of a solid-state electrochemical cell.

A Cs SAES getter is used to deposit Cs atoms. The getter needs several hours of degassing before operating it for first time. Afterwards, 2 A should be kept running through it to prevent contamination. To deposit Cs atoms onto the sample, 6 A is run through the getter. The coverage of Cs can be calibrated by LEIS spectra.

1.4 Single Crystal Growth and Surface Preparation Methods

Bulk single crystal Bi_2Se_3 and Bi_2Te_3 are synthesized using a slow-cooling method. Bi shot and Se(Te) shot (Alfa Aesar, 5N purity) are mixed stoichiometrically and sealed in a 17 mm diameter ampule and flashed twice under high purity Ar. After flashing, the ampule is pumped to a pressure of about 2×10^{-6} Torr. For Bi_2Se_3, the ampule is heated to and kept at 750°C for one day, slowly cooled to 500°C for 68 hours, and then annealed at 500°C for three days before being cooled to room temperature. For Bi_2Se_3, the tube is heated to 700°C for 60 hrs, cooled to 475°C and kept at that temperature for 3 days before cooling naturally to room temperature. The crystals produced in this manner can be easily cleaved along the (0001) plane and flakes with dimensions of around 1 cm × 1 cm × 3 mm can be used as samples.

Two methods are deployed to prepare clean and ordered sample surfaces. The first is *in situ* cleaving. An Al bar is glued to sample surface by epoxy, and sample is glued to sample holder by silver paste. By knocking off the Al bar in vacuum, a fresh ordered surface is exposed. The second is *ex situ* cleaving using carbon tape and followed by Ar^+ ion bombardment and annealing (IBA) in vacuum. Samples are attached to sample holders by spot-welded Ta strips and cleaved several times by carbon tape until a shiny flat surface

is produced. The sample is transferred into the UHV chamber and lightly annealed at 130ºC to degas it and remove adsorbed water and hydrocarbons. The surface is then bombarded by 0.5 keV Ar^+ at an average beam flux of approximately 200 nA cm^{-2} for 30 min. The sample is finally recrystallized by annealing it for 30 min at 430ºC for Bi_2Se_3 or 340ºC for Bi_2Te_3. LEED confirms that the surfaces are ordered by displaying a clear 1×1 pattern.

1.5 Molecular Beam Epitaxy

Molecular beam epitaxy (MBE) is a thin film growth method [60]. Each MBE source produces a beam of atoms or molecules that is aimed at the substrate. There is little scattering between the molecules as their mean free path is very large in UHV. MBE can be used to grow films epitaxially, which means that it grows ordered crystalline overlayers due to the use of a low deposition rate combined with a good lattice match between the deposited material and the substrate. The MBE instrument used in this dissertation has two Knudsen effusion cells for evaporating Bi and Te. The sample can be transferred from main chamber to the MBE chamber and mounted onto a rotatable manipulator. The sample can be heated up to 500ºC on this manipulator. A quartz crystal microbalance is used to calibrate the deposition rate.

There are three primary growth modes for epitaxial growth at a crystal surface or interface [61], which are represented in Figure 1.15. The first one is the Volmer-Weber or 'island' growth mode, which occurs when the bonding energy between the atoms of the evaporated material is stronger than bonding to the substrate. The second is the Frank-van der Merwe, or layer-by-layer growth, mode which occurs when there is a good match of

the lattice parameters of the substrate and material being deposited. The third is the Stranski-Krastanov, or layer-plus-island, mode in which the first layer grows in registry with the substrate but successive layers form islands. In reality, however, growth via MBE can also be much more complicated.

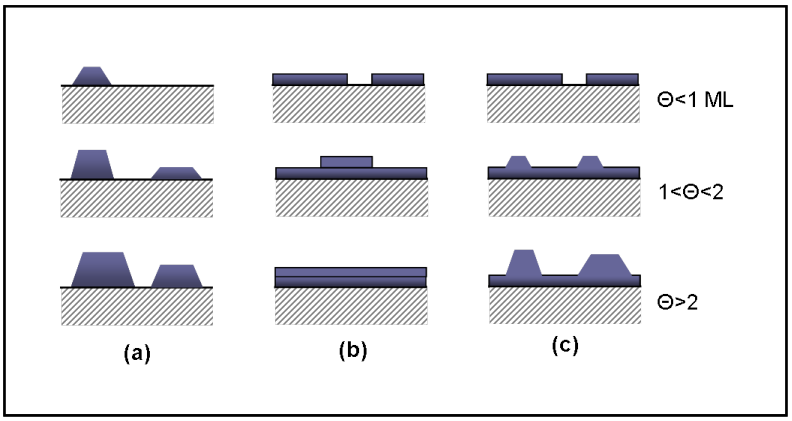

Figure 1. 15. Cross-sectional views of the three primary modes of thin-film growth (a) Volmer–Weber (VW: island formation), (b) Frank–van der Merwe (FM: layer-by-layer), and (c) Stranski–Krastanov (SK: layer-plus-island). Each mode is shown for several different surface coverages, Θ.

1.6 Outline of the Dissertation

This dissertation involves investigations of the atomic and electronic structure of TI surfaces and the reactions on these surfaces using surface sensitive tools including LEIS, LEED and AFM. Chapter 1 provides the background of the projects and introduces the techniques used in the experiments.

Chapter 2 talks about Bi(0001) films with thicknesses up to several bilayers (BLs) grown on Se-terminated Bi_2Se_3(0001) surfaces. LEED, LEIS and AFM are used to investigate the surface composition, topography and atomic structure. It is found that the lattice constant of the first Bi BL matches that of the substrate and a single Bi BL on Bi_2Se_3 is a particularly stable structure.

Chapter 3 shows that dipoles caused by the spatial distribution of the conductive electrons in the TSS in Bi_2Te_3 can be detected by the neutralization of scattered low-energy Na^+. This result demonstrates how alkali ion scattering method can be applied to provide direct experimental evidence of the spatial distribution of electrons in filled surface states.

Chapter 4 presents the adsorption and reaction of halogens (Br_2 and Cl_2) with Bi_2Se_3 and Bi_2Te_3 and these same surfaces covered with Bi films. It is found that Br weakly chemisorbs to the Se- or Te-terminated clean surfaces and light annealing removes the adsorbates restoring the intact surfaces. In contrast, halogens dissociatively adsorb onto surfaces covered with an additional bilayer of Bi, having a p-doping effect. Annealing these halogen-covered surfaces at 130ºC causes Bi atoms to be chemically etched away and the surface eventually reverts to a Se- or Te-termination.

Chapter 5 discusses Cs adsorption on the Bi_2Se_3 surface. The results show that much of the deposited Cs quickly diffuses to the step edges forming one-dimensional chains of positively charged adatoms that lower the surface WF. A slow diffusion of adsorbed Cs from the terraces to the step edges is marked by further changes in the neutralization of scattered Na^+ and work function over time. The WF of clean Bi_2Se_3 is too high to observe any difference in the neutralization of Na^+ scattered from Bi and Se, but

upon Cs deposition the WF decreases and differences are observed. The spatial distribution of the conductive charges in the TSS, which are positioned between the first and second atomic layers as in Bi_2Te_3, is thus confirmed for Bi_2Se_3 and it is shown that the Cs adsorption does not affect them.

Bibliography

1. M. Z. Hasan and C. L. Kane, Rev. Mod. Phys. **82**, 3045 (2010).

2. C. L. Kane and E. J. Mele, Phys. Rev. Lett. **95**, 146802 (2005).

3. B. A. Bernevig and S.-C. Zhang, Phys. Rev. Lett. **96**, 106802 (2006).

4. B. A. Bernevig, T. L. Hughes, and S.-C. Zhang, Science **314**, 1757 (2006).

5. M. König, S. Wiedmann, C. Brüne, A. Roth, H. Buhmann, L. W. Molenkamp, X.-L. Qi, and S.-C. Zhang, Science **318**, 766 (2007).

6. C. K. L. Fu, E. Mele, Phys. Rev. B **106803**, 1 (2007).

7. J. E. Moore and L. Balents, Phys. Rev. B **75**, 3 (2007).

8. R. Roy, Phys. Rev. B **79** (2009).

9. D. Hsieh, D. Qian, L. Wray, Y. Xia, Y. S. Hor, R. J. Cava, and M. Z. Hasan, Nature **452**, 970 (2008).

10. H. Zhang, C.-X. Liu, X.-L. Qi, X. Dai, Z. Fang, and S.-C. Zhang, Nat. Phys. **5**, 438 (2009).

11. Y. Xia, D. Qian, D. Hsieh, L. Wray, A. Pal, H. Lin, A. Bansil, D. Grauer, Y. S. Hor, R. J. Cava, and M. Z. Hasan, Nat. Phys. **5**, 398 (2009).

12. Y. L. Chen, J. G. Analytis, J.-H. Chu, Z. K. Liu, S.-K. Mo, X. L. Qi, H. J. Zhang, D. H. Lu, X. Dai, Z. Fang, S. C. Zhang, I. R. Fisher, Z. Hussain, and Z.-X. Shen, Science **325**, 178 (2009).

13. T. Hirahara, G. Bihlmayer, Y. Sakamoto, M. Yamada, H. Miyazaki, S.-i. Kimura, S. Blügel, and S. Hasegawa, Phys. Rev. Lett. **107**, 166801 (2011).

14. H. Lin, T. Das, Y. Okada, M. C. Boyer, W. D. Wise, M. Tomasik, B. Zhen, E. W. Hudson, W. Zhou, V. Madhavan, C.-Y. Ren, H. Ikuta, and A. Bansil, Nano Lett. **13**, 1915 (2013).

15. Z. Wei, Y. Rui, Z. Hai-Jun, D. Xi, and F. Zhong, New J. Phys. **12**, 065013 (2010).

16. W. Zhou, H. Zhu, and J. A. Yarmoff, Phys. Rev. B **97**, 035413 (2018).

17. H. M. Benia, C. Lin, K. Kern, and C. R. Ast, Phys. Rev. Lett. **107**, 177602 (2011).

18. T. Valla, Z.-H. Pan, D. Gardner, Y. S. Lee, and S. Chu, Phys. Rev. Lett. **108**, 117601 (2012).

19. D. Hsieh, Y. Xia, D. Qian, L. Wray, J. H. Dil, F. Meier, J. Osterwalder, L. Patthey, J. G. Checkelsky, N. P. Ong, A. V. Fedorov, H. Lin, A. Bansil, D. Grauer, Y. S. Hor, R. J. Cava, and M. Z. Hasan, Nature **460**, 1101 (2009).

20. M. Koleini, T. Frauenheim, and B. Yan, Phys. Rev. Lett. **110**, 016403 (2013).

21. H. J. Noh, H. Koh, S. J. Oh, J. H. Park, H. D. Kim, J. D. Rameau, T. Valla, T. E. Kidd, P. D. Johnson, Y. Hu, and Q. Li, Europhys Lett **81**, 57006 (2008).

22. M. Bianchi, R. C. Hatch, D. Guan, T. Planke, J. Mi, B. B. Iversen, and P. Hofmann, Semicond Sci Technol **27**, 124001 (2012).

23. C. Seibel, H. Maaß, M. Ohtaka, S. Fiedler, C. Jünger, C.-H. Min, H. Bentmann, K. Sakamoto, and F. Reinert, Phys. Rev. B **86**, 161105(R) (2012).

24. M. Bianchi, R. C. Hatch, Z. Li, P. Hofmann, F. Song, J. Mi, B. B. Iversen, Z. M. Abd El-Fattah, P. Löptien, L. Zhou, A. A. Khajetoorians, J. Wiebe, R. Wiesendanger, and J. W. Wells, ACS Nano **6**, 7009 (2012).

25. A. G. Ryabishchenkova, M. M. Otrokov, V. M. Kuznetsov, and E. V. Chulkov, J. Exp. Theor. Phys+. **121**, 465 (2015).

26. Z.-H. Zhu, G. Levy, B. Ludbrook, C. N. Veenstra, J. A. Rosen, R. Comin, D. Wong, P. Dosanjh, A. Ubaldini, P. Syers, N. P. Butch, J. Paglione, I. S. Elfimov, and A. Damascelli, Phys. Rev. Lett. **107**, 186405 (2011).

27. M. T. Edmonds, J. T. Hellerstedt, A. Tadich, A. Schenk, K. M. O'Donnell, J. Tosado, N. P. Butch, P. Syers, J. Paglione, and M. S. Fuhrer, J. Phys. Chem. C **118**, 20413 (2014).

28. L. V. Yashina, J. Sa´nchez-Barriga, M. R. Scholz, A. A. Volykhov, A. P. Sirotina, V. S. Neudachina, M. E. Tamm, A. Varykhalov, D. Marchenko, G. Springholz, G. Bauer, A. Knop-Gericke, and O. Rade, ACS Nano **7**, 5181 (2013).

29. H. M. Benia, C. Lin, K. Kern, and C. R. Ast, Phys. Rev. Lett. **107**, 177602 (2011).

30. H. Zhu, W. Zhou, and J. A. Yarmoff, J. Phys. Chem. C **122**, 16122 (2018).

31. S. Murakami, Phys. Rev. Lett. **97**, 236805 (2006).

32. I. K. Drozdov, A. Alexandradinata, S. Jeon, S. Nadj-Perge, H. Ji, R. J. Cava, B. Andrei Bernevig, and A. Yazdani, Nat. Phys. **10**, 664 (2014).

33. G. Bian, Z. Wang, X.-X. Wang, C. Xu, S. Xu, T. Miller, M. Z. Hasan, F. Liu, and T.-C. Chiang, ACS Nano **10**, 3859 (2016).

34. F. Yang, L. Miao, Z. F. Wang, M.-Y. Yao, F. Zhu, Y. R. Song, M.-X. Wang, J.-P. Xu, A. V. Fedorov, Z. Sun, G. B. Zhang, C. Liu, F. Liu, D. Qian, C. L. Gao, and J.-F. Jia, Phys. Rev. Lett. **109**, 016801 (2012).

35. L. Miao, Z. F. Wang, W. Ming, M.-Y. Yao, M. Wang, F. Yang, Y. R. Song, F. Zhu, A. V. Fedorev, Z. Sun, C. L. Gao, C. Liu, Q.-K. Xue, C.-X. Liu, F. Liu, D. Qian, and J.-F. Jia, PNAS **110**, 2758 (2013).

36. A. Eich, M. Michiardi, G. Bihlmayer, X. G. Zhu, J.-L. Mi, B. B. Iversen, R. Wiesendanger, P. Hofmann, A. A. Khajetoorians, and J. Wiebe, Phys. Rev. B **90**, 155414 (2014).

37. Z. F. Wang, M. Y. Yao, W. Ming, L. Miao, F. Zhu, C. Liu, C. L. Gao, D. Qian, J. F. Jia, and F. Liu, Nature Communications **4**, 1384 (2013).

38. T. Lei, K.-H. Jin, N. Zhang, J.-L. Zhao, C. Liu, W.-J. Li, J.-O. Wang, R. Wu, H.-J. Qian, F. Liu, and K. Ibrahim, J Phys: Condens Matter **28**, 255501 (2016).

39. Y. N. Zhang, J. Chem. Phys. **143**, 151101 (2015).

40. X. He, W. Zhou, Z. Y. Wang, Y. N. Zhang, J. Shi, R. Q. Wu, and J. A. Yarmoff, Phys. Rev. Lett. **110**, 156101 (2013).

41. A. S. Hewitt, J. Wang, J. Boltersdorf, P. A. Maggard, and D. B. Dougherty, J. Vac. Sci. Technol. B **32**, 04E103 (2014).

42. H. Niehus, W. Heiland, and E. Taglauer, Surf. Sci. Rep. **17**, 213 (1993).

43. W. J. Rabalais, *Principles and applications of ion scattering spectrometry : surface chemical and structural analysis* (Wiley, New York, 2003).

44. E. Taglauer and W. Heiland, Applied physics **9**, 261 (1976).

45. X. He, W. Zhou, Z. Y. Wang, Y. N. Zhang, J. Shi, R. Q. Wu, and J. A. Yarmoff, Phys. Rev. Lett. **110**, 156101 (2013).

46. T. Fauster, Vacuum **38**, 129 (1988).

47. A. V. Onufriev and J. B. Marston, Phys. Rev. B **53**, 13340 (1996).

48. J. B. Marston, D. R. Andersson, E. R. Behringer, B. H. Cooper, C. A. DiRubio, G. A. Kimmel, and C. Richardson, Phys. Rev. B **48**, 7809 (1993).

49. P. Nordlander and J. C. Tully, Surf. Sci. **211**, 207 (1989).

50. P. Nordlander and J. C. Tully, Phys. Rev. B **42**, 5564 (1990).

51. A. J. Algra, E. v. Loenen, E. P. T. M. Suurmeijer, and A. L. Boers, Radiation Effects **60**, 173 (1982).

52. G. A. Kimmel and B. H. Cooper, Phys. Rev. B **48**, 12164 (1993).

53. M. Barat, J. C. Brenot, J. A. Fayeton, and Y. J. Picard, Rev. Sci. Instrum. **71**, 2050 (2000).

54. M. Aono, C. Oshima, S. Zaima, S. Otani, and Y. Ishizawa, Jpn. J. Appl. Phys. **20**, L829 (1981).

55. M. A. Karolewski, Nucl. Instr. Meth. Phys. Res. B **230**, 402 (2005).

56. J. B. Pendry, in *Interaction of Atoms and Molecules with Solid Surfaces*, edited by V. Bortolani, N. H. March and M. P. Tosi (Springer US, Boston, MA, 1990), p. 201.

57. J. B. Pendry, *Low Energy Electron Diffraction: The Theory and Its Application to Determination of Surface Structure* (Academic Press, London, 1974).

58. W. K. Wang, W. C. Simpson, and J. A. Yarmoff, Phys. Rev. B **61**, 2164 (2000).

59. R. D. Schnell, D. Rieger, A. Bogen, K. Wandelt, and W. Steinmann, Solid State Commun. **53**, 205 (1985).

60. A. Y. Cuo and J. R. Arthur, Prog Solid State Chem **10** (1975).

61. J. A. Venables, G. D. T. Spiller, and M. Hanbucken, Rep Prog Phys **47**, 399 (1984).

Chapter 2

The growth of bismuth on Bi_2Se_3 and the stability of the first bilayer

2.1 Introduction

Topological Insulators (TIs) are promising materials for superconductor, spintronics and quantum computing applications because of their intrinsic topological surface states (TSS) that are protected by time-reversal symmetry [1-3]. Bi_2Se_3 is one of the most well-known TIs due to its comparatively large, and thus practical, bulk band gap of 0.35 eV [2] and it's simple surface band structure in which the TSS form a Dirac cone [4]. Bi_2Se_3 has a rhombohedral structure belonging to the $R\bar{3}m$ space group. Five two-dimensional (2D) hexagonal lattices of Bi and Se are stacked together along the [0001] direction in the sequence of Se-Bi-Se-Bi-Se to form a quintuple layer (QL). Adjacent QLs are connected to each other by weak van der Waals forces. When a high quality pure Bi_2Se_3 single crystal is cleaved in ultra-high vacuum (UHV) or subjected to ion bombardment and annealing (IBA) in UHV, the resulting surface is highly ordered and terminated by Se at the top of a complete QL [5].

This chapter contains material published in H. Zhu, W. Zhou, J. A. Yarmoff, The growth of bismuth on Bi_2Se_3 and the stability of the first bilayer, *Thin Solid Films* **660**, 343 (2018)

Bulk Bi is also a 2D material that is composed of bilayers (BLs) bonded to each other by van der Waals forces [6]. A single Bi(0001) BL is also reported to be a 2D topological insulator [7,8]. Ultrathin Bi films of only a few BLs are attracting more interest for their nontrivial properties such as a large magnetoresistance and topological edge states [9,10]. Hetero-structure engineering with Bi BLs and other materials, including 3D TIs, are becoming popular because of the ability to control their electronic properties and fabricate unique device structures [11-13]. Recent studies show giant Rashba-split states in Bi BL-terminated Bi_2Se_3 surfaces prepared by both epitaxial growth [14-16] and hydrogen etching methods [17,18].

Deposited Bi grows on TI surfaces at room temperature along the [0001] direction in a quasi bilayer-by-bilayer mode, and has the same hexagonal lattice symmetry as Bi_2Se_3 [19,20]. Previous STM work shows that the first Bi bilayer is strongly compressed on Bi_2Se_3(0001) substrate so that it matches the lattice parameter of the substrate. Further Bi deposition forms BL islands that eventually coalesce to complete bilayers with sufficient coverage. A periodic buckling of the lattice is found beginning from deposition of the 2^{nd} BL and lasting until the 5^{th} BL is deposited. The Bi BL lattice gradually relaxes to become bulk-like at a coverage of 24 BLs.

An interesting aspect of the Bi/Bi_2Se_3 system is the unique stability of a single deposited BL. Density functional theory (DFT) calculations show that the single BL-terminated structure has a lower surface energy than the bare Se-terminated surface [21,22] and there is a stronger bonding between a QL and a Bi BL than there is between QLs [23,24]. In support of this notion, Bi_2Se_3 surfaces terminated with a single Bi BL have been

found to spontaneously form on *in-situ* [22] and *ex-situ* [25] cleaved samples. In addition, there is a report that exposing a Se-terminated surface to air for 5 minutes can form a stable Bi BL on the surface, presumably through a (still-unidentified) surface chemical reaction [26].

The present paper presents a low energy electron diffraction (LEED), low energy ion scattering (LEIS) and atomic force microscopy (AFM) study of Bi BLs grown on Bi_2Se_3(0001) by molecular beam epitaxy (MBE). It is confirmed that the first deposited BL grows epitaxially, and it is further shown that the Bi atoms in this first BL sit in fcc-like sites. As shown previously, subsequent layers grow as islands, since they are affected by the strain resulting from the differences in the lattice constants of Bi_2Se_3 and Bi, until the film is thick enough to form what is essentially bulk single crystal Bi. A relatively low temperature annealing of the thicker films shows that the first BL remains in place as the rest of the deposited Bi coalesces into islands, which is another sign of the unique stability of the 1st BL.

2.2 Experimental Procedure

Single crystal Bi_2Se_3(0001) is used as the substrate. Bulk Bi_2Se_3 was prepared by melting stoichiometric mixtures of Bi (99.999%, Alfa Aesar) and Se shot (99.999+%, Alfa Aesar) in an evacuated quartz ampule (2×10^{-6} Torr) with an inner diameter of 17 mm, and then following a slow-cooling procedure [5]. Approximately 1 cm × 1 cm × 2 mm single crystal Bi_2Se_3 plaques are cleaved from the bulk Bi_2Se_3 crystals and attached to a transferable tantalum (Ta) sample holder (Thermionics) using spot-welded Ta strips.

Most of the measurements are performed in an ultra-high vacuum (UHV) main chamber that has a base pressure better than 2×10^{-10} Torr. There is a load-lock chamber that enables the sample holders to be inserted without the need to vent and re-bake the main chamber. The samples are transferred onto an x-y-z manipulator that allows for rotation about both the polar and azimuthal axes and includes an electron-beam heater. For the measurements performed here, the samples are heated radiatively without applying a bias voltage to the filament, as the annealing temperature needed to prepare Bi_2Se_3 is rather low. This main chamber contains a sputter gun (Physical Electronics) for sample cleaning, optics for LEED (Princeton Research), and the equipment needed for LEIS that is described below. The sample is held at room temperature during the collection of LEED images and LEIS spectra.

A Se-terminated Bi_2Se_3(0001) surface is prepared in the main UHV chamber by ion bombardment and annealing (IBA), which involves 30 min of 500 eV Ar^+ ion bombardment at a current density of 2.5×10^{12} cm^{-2} sec^{-1} with the sample at room temperature followed by annealing at 490°C for 30 min. This IBA procedure produces high quality clean and well-ordered surfaces, as described elsewhere [27]. The annealing temperature is calibrated by a thermocouple attached to the Ta sample holder, but the actual temperature of the surface can vary from -50°C to +20°C from the reported value as the thermocouples are not attached directly to the samples. Also, thicker samples require more annealing time to allow the surface to reach the desired temperature.

Bi(0001) BLs are grown on Bi_2Se_3(0001) surfaces at room temperature using a molecular beam epitaxy (MBE) system that is attached to the main chamber such that

samples can be transferred under UHV. Bi is evaporated at a rate of 1.45 Å min^{-1}, as calibrated by a quartz crystal microbalance (QCM), from a Knudsen cell heated to 530°C. The amount of Bi deposited is also confirmed using AFM images, as discussed below.

The rear-view LEED system (Princeton Research Instruments) is used to ascertain the sample cleanness, crystallinity and orientation of the surface unit cell, and to monitor how the lattice parameter changes with the growth of Bi films. The sample position is kept the same with respect to the LEED optics for each measurement. The electron beam is normally incident onto the surface with the beam energy fixed at 21.8 eV.

Low energy ion scattering (LEIS) time-of-flight (TOF) spectra are used to identify the surface elemental composition [28] and measure the neutral fraction (NF) of scattered Na^+ [29]. A 3.0 keV Na^+ ion beam (Kimball Physics IGS-4) pulsed at 100 kHz is normally incident onto the sample surface and the scattered projectiles are collected at a scattering angle of 125° by a microchannel plate (MCP) detector located at the end of a 0.57 m long flight tube. A bias voltage of 400 V is applied to deflection plates in the flight tube to separate scattered ions from neutrals, allowing for independent collection of spectra for the total scattered yield and the scattered neutrals. The bias voltage is periodically turned on and off every 60 sec while both spectra are collected simultaneously to avoid any effects of long term drift in the incident ion beam current. The front of the MCP is held at ground potential so that the scattered neutrals and ions impact the detector with the same kinetic energy.

Impact collision ion scattering spectrometry (ICISS) is used to probe the surface atomic structure [30]. ICISS is performed using a 3.0 keV Na^+ ion beam and a Comstock

electrostatic analyzer (ESA), which measures only scattered ions, by fixing the scattering angle at 161° and rotating the sample about the polar axis. An energy spectrum is first collected to locate the positions of the Bi single scattering peak (SSP) and the Se SSP. The detection energy is then fixed at one SSP energy and the intensity of that SSP is monitored with respect to the incident polar angle as the sample is rotated. The energy is then set to the other SSP energy, and the ICISS data collection procedure is repeated. The sample manipulator has a computer-controlled stepper motor that automatically rotates the sample to enable quick and reproducible collection of the ICISS angular distributions.

AFM images are collected using a separate Dimension 3000 (Digital Instruments) apparatus. The samples used for AFM are cleaved *in situ* under UHV, as this produces larger terraces that are better suited for AFM than IBA-prepared samples [25,31]. Bi is deposited in UHV using the MBE system, and the samples are then removed from vacuum and transported to the AFM instrument. The tapping mode images are collected in air at room temperature using TESPA-V2 silicon tips (Bruker).

2.3 Results

AFM measurements are conducted to both calibrate the coverage of the Bi BLs and to monitor changes of the surface topography. Figure 2.1 shows AFM images collected after various treatments. Figure 2.1(a) shows the surface of Bi_2Se_3 following *in situ* cleaving in UHV, although the sample was removed from vacuum to collect the image. The IBA-prepared samples are essentially atomically flat, but they contain QL-high steps that separate terraces with widths of approximately 200 nm [27]. In contrast, *in-situ* cleaved

samples contain wider terraces, which makes them more suitable for calibrating the Bi coverage with AFM. Figures 2.1(b)-(e) show images collected from Bi films grown on Bi_2Se_3. The green curve labeled A in Fig.2.1(g) shows the profile of the line shown in the 1.0 BL image (Fig.2.1(c)). The heights of the features seen in Fig.2.1(g) are all about 0.5 nm, which corresponds to that of a single Bi BL, and this value is indicative of all of the features observed in the AFM images. The Bi coverage is calculated from the ratios of the accumulated area of the Bi islands or films to the area of the entire substrate. Analysis of the areas measured for Bi evaporation times of 2.5, 3.5 and 5.5 min indicate that these substrates are covered with 0.7, 1.0 and 1.5 BL, respectively. This implies that the Bi evaporation rate is about 1.4 Å min^{-1} on average, which is consistent with the value determined using the QCM (1.45 Å min^{-1}). A 6 Bi BL covered surface is also examined, as shown in Fig.2.1(e), in which the surface is fairly flat with a height variance of ±0.5 nm, as shown by line profile B in Fig.2.1(g), but it still has features with heights that are integral numbers of Bi BLs. The AFM images confirm that Bi grows in quasi bilayer-by-bilayer mode at high coverages and there's no evidence of tall islands for a 6 BL coverage at room temperature.

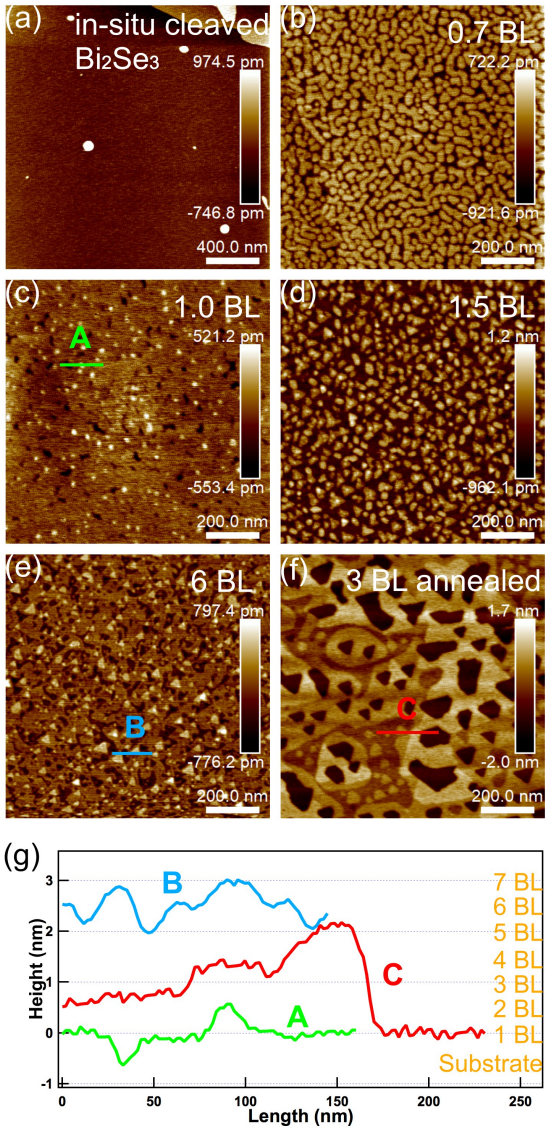

Figure 2. 1. AFM images collected from (a) an *in-situ* cleaved Bi_2Se_3 surface, and from Bi films grown on Bi_2Se_3 with evaporation times of (b) 2.5 min, (c) 3.5 min (d) 5.5 min and (e) 21 min, which lead to the indicated Bi coverages (see text), (f) 3 Bi BLs grown on Bi_2Se_3 and annealed at 120°C for 10 hrs, (g) height profiles of lines A, B and C that are drawn in (c), (d) and (e).

LEED is used to monitor the surface symmetry and determine how the lattice parameter changes with Bi deposition. Figure 2.2 shows LEED patterns collected for

different coverages of Bi. Note that the LEED image and background appear dimmer on the right half of the screen due to a degradation of the screen coating. A pristine Se-terminated Bi_2Se_3 substrate displays a 1×1 hexagonal pattern, as seen in Fig. 2.2(a). Three-fold LEED spots that are observed at higher beam energies are not shown here. When a single Bi BL is deposited onto the substrate, the LEED spots shift slightly towards the center and get much brighter, as seen in Fig. 2.2(b) [16]. Three-fold higher-order satellite spots start to show up at 1.7 BL, while the spots from the 1st BL are still visible, which indicates that a Moiré structure is formed on substrate. The satellite spots get clearer and brighter when the Bi coverage reaches 3 BLs at the expense of decreasing the intensity of the LEED spots associated with the 1st Bi BL. The satellite spots only appear if the Bi_2Se_3 substrate and the Bi film are both clean and well-ordered. For example, if the annealing temperature is too low or the annealing time too short during the IBA process, then the LEED spots are blurry. The satellite spots gradually fade out as more Bi is deposited, while the LEED spots corresponding to bulk Bi(0001) get brighter (Figs. 2.2(d)-(f)). The LEED pattern eventually evolves to that of a bulk-like Bi(0001) single crystal (Fig. 2.2(g)) when the coverage reaches about 8 BLs or more.

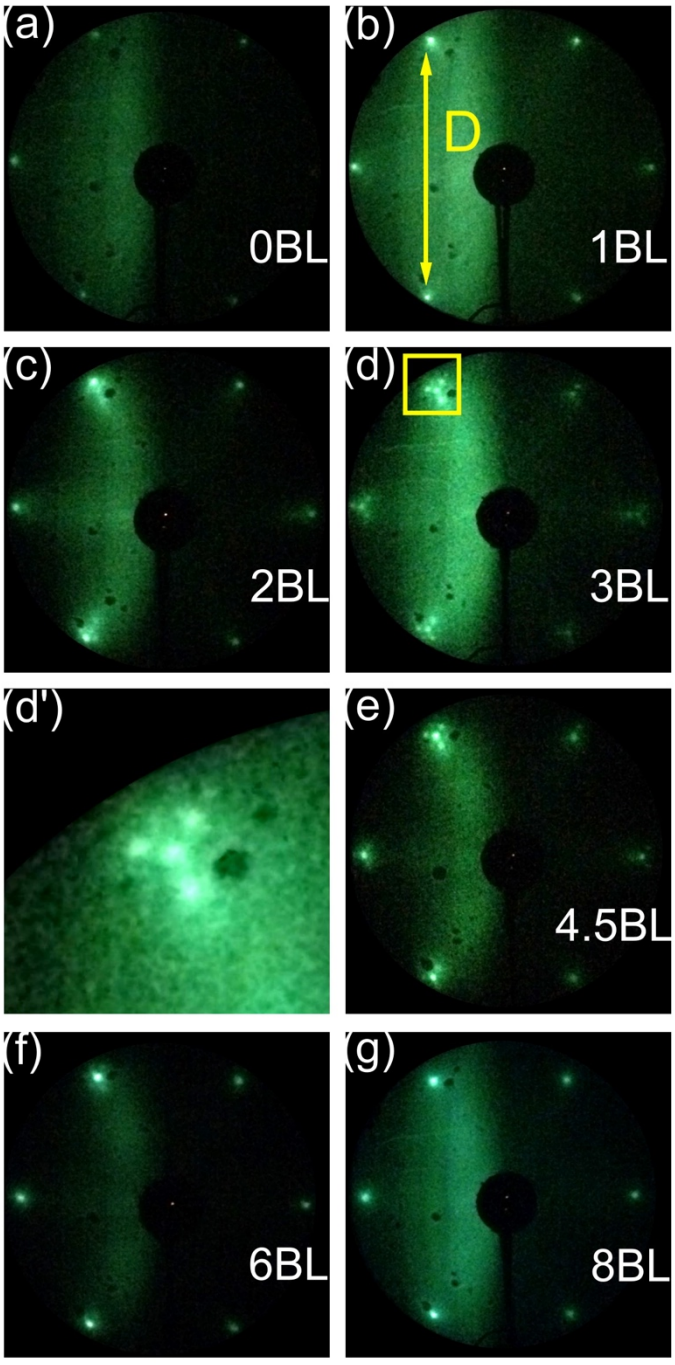

Figure 2. 2. LEED patterns collected from Bi_2Se_3 surfaces with the indicated Bi coverages. (d') is a close-up of the boxed area in (d). All of the LEED images were collected using a beam energy of 21.8 eV.

Based on the average of the measured distances between the centers of equivalent LEED spots (such as line D in Fig. 2.2(b)) and using the known Bi_2Se_3 surface lattice constant of 4.14 Å [32] for calibration, the lattice constants of the outermost Bi BLs are calculated, which are shown in Fig. 2.3 as a function of Bi BL coverage. The lattice parameters shown in Fig. 2.3 have error limits of ±0.05 Å as estimated from the standard deviation of multiple measurements. These data are reasonably consistent with the results of Ref. [19], although they show a less gradual change of lattice constant with Bi film thickness. Although this can be due to the finer gradations of coverage used in Ref. [19] combined with the lower resolution of our LEED optics, another possibility is that LEED probes deeper than RHEED and is thus less sensitive to changes in the uppermost layer lattice constant. Thus, by the time that LEED shows a change in lattice constant, it is probing multiple bilayers.

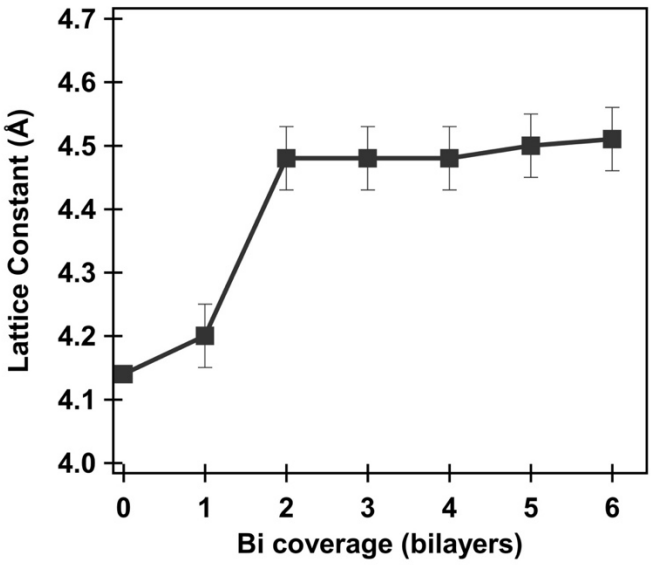

Figure 2. 3. Top layer lattice constant as a function of Bi coverage calculated using the length of line D in Fig. 2.2(b) and calibrated with the known Bi_2Se_3 lattice constant of 4.14 Å.

The average grain size of the first bilayer can be estimated from the LEED spot width and the distance between the LEED spots. The measured width of LEED spots is the sum in quadrature of the intrinsic resolution of the LEED optics ($\sigma_{intrinsic}$) and the broadening caused by a limited surface domain size (σ_{grain}). The measured LEED spot width is 2.3% of the Brillouin zone (BZ) for an IBA prepared Bi_2Se_3 substrate, and 5.6% of the BZ for a 1 Bi BL covered sample. The intrinsic width, $\sigma_{intrinsic}$, is unknown, but a range of possible grain sizes can be estimated. By assuming that $\sigma_{intrinsic} = 0$, the lower limit of the grain size is the inverse of the width due to the finite grain size, which is equal to $\frac{1}{\sigma_{grain}} = \frac{1}{\sigma_{measured}} = \frac{1}{5.6\%} = 17.8$ atoms. By assuming that the Bi_2Se_3 substrate is perfect with an infinite grain size, the width measured from the clean substrate is then equal to $\sigma_{intrinsic}$ and the upper limit of the 1st BL grain size is calculated to be $\frac{1}{\sigma_{grain}} = \frac{1}{\sqrt{\sigma_{measured}^2 - \sigma_{intrinsic}^2}} = \frac{1}{\sqrt{5.6\%^2 - 2.3\%^2}} = 19.6$ atoms. Thus, the estimated diameter of the grains in the first Bi BL is around 19 atoms.

The lattice constant of the superlattice formed by the 1st and 2nd Bi BLs can be calculated by inserting the lattice constants of the 1st and 2nd BLs into the Moiré equation,

$$d = \frac{a_1 \times a_2}{|a_1 - a_2|},$$

where a_1 is lattice constant of the 1st Bi BL (4.2 Å) and a_2 is the lattice constant of the 2nd Bi BL (4.48 Å). From this analysis, it is found that d = 67 Å, which suggests that the two lattices line up such that 15 unit cells of the 2nd Bi BL line up with 16 unit cells of the substrate. As the Bi coverage increases beyond 2 BLs, the lattice constant remains nearly

the same, but expands very slightly until it reaches the Bi(0001) bulk value of 4.54 Å [6] at a thickness of about 5 BLs.

LEIS is a surface sensitive technique that is typically used to investigate the atomic composition and structure of the first few atomic layers of a solid [28]. Low energy ions (1 to 10 keV) only penetrate the first few atomic layers, and a double alignment scattering geometry can be chosen to make the spectra sensitive to only the outermost surface atoms [5,22,33]. In addition, when alkali ions are used as the projectiles, the probability that they are neutralized is related to the local electrostatic potential (LEP) just above the scattering site [34-36].

LEIS TOF spectra are used here to identify the surface elemental composition and measure the neutral fraction (NF). Figure 2.4 shows TOF spectra collected from Bi_2Se_3 samples with different Bi coverages. Note that the time scale in the figure is reversed so that increasing energy of the scattered projectiles is towards the right. The most prominent features in the spectra are the single scattering peaks (SSPs), which are labeled by the target atom symbol in the figure. A SSP corresponds to a projectile that experiences a single hard collision with a surface target atom and backscatters directly into the detector. The target atoms can be considered to be unbound atoms located at the lattice sites, as the kinetic energy of the projectiles is much greater than the bonding energy of atoms in a solid. Because low energy ions have very small de Broglie wavelengths, the energy lost in a single collision is primarily through a classical binary elastic collision so that the kinetic energy of the SSPs provide the mass distribution of the surface atoms. The peak at 4.1 μs in Fig. 2.4 is the Bi SSP, while the peak at 5.6 μs is the Se SSP. The data is analyzed by

integrating each SSP after subtracting the background caused by multiple scattering, as described elsewhere [34]. This allows for a determination of the site-specific neutral fraction (NF) by calculating the ratio of the neutral yield to the total yield for each SSP [29]. Similarly, the ratio of the total yield Se SSP to the total yield Bi SSP can be determined, which is useful for monitoring the surface composition.

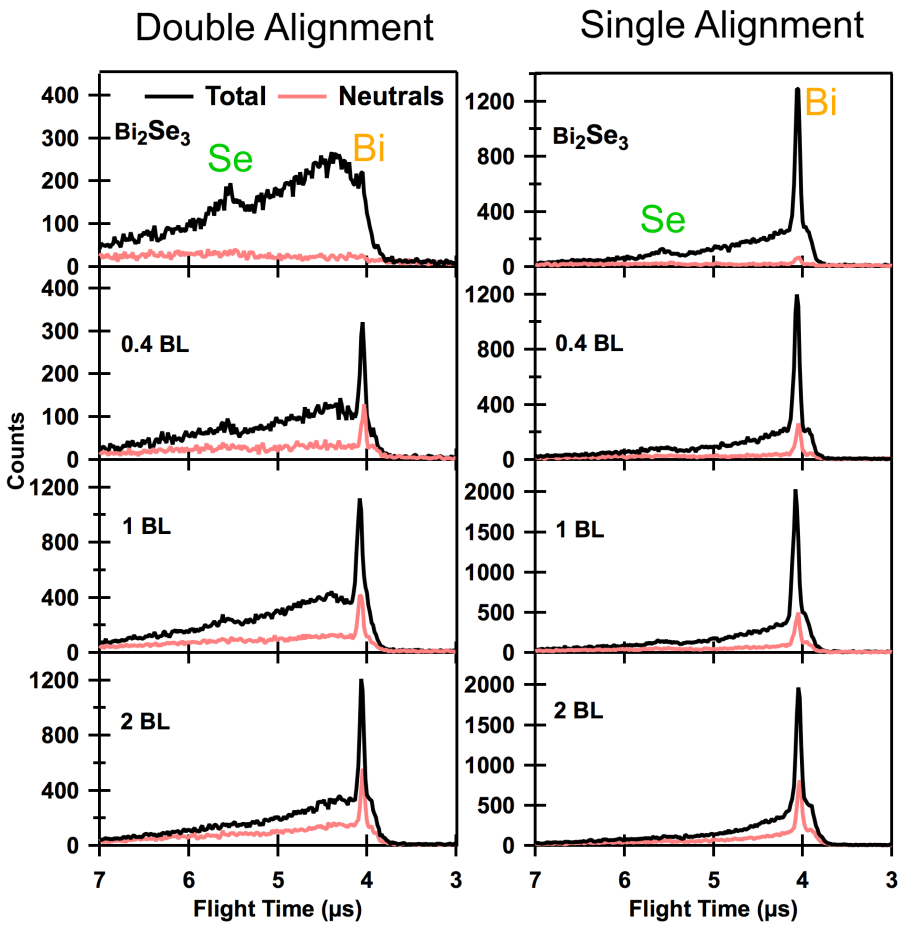

Figure 2. 4. LEIS TOF spectra collected from Bi_2Se_3 with the indicated Bi coverages. A 3.0 keV Na^+ ion beam is incident normal to sample surface and the detector is positioned at a scattering angle of 125°. In each spectrum, the black line represents total yield and red line represents the scattered neutral particles. The spectra are normalized to each other using the ion beam current measured on the sample and the data collection time so that they can be quantitatively compared.

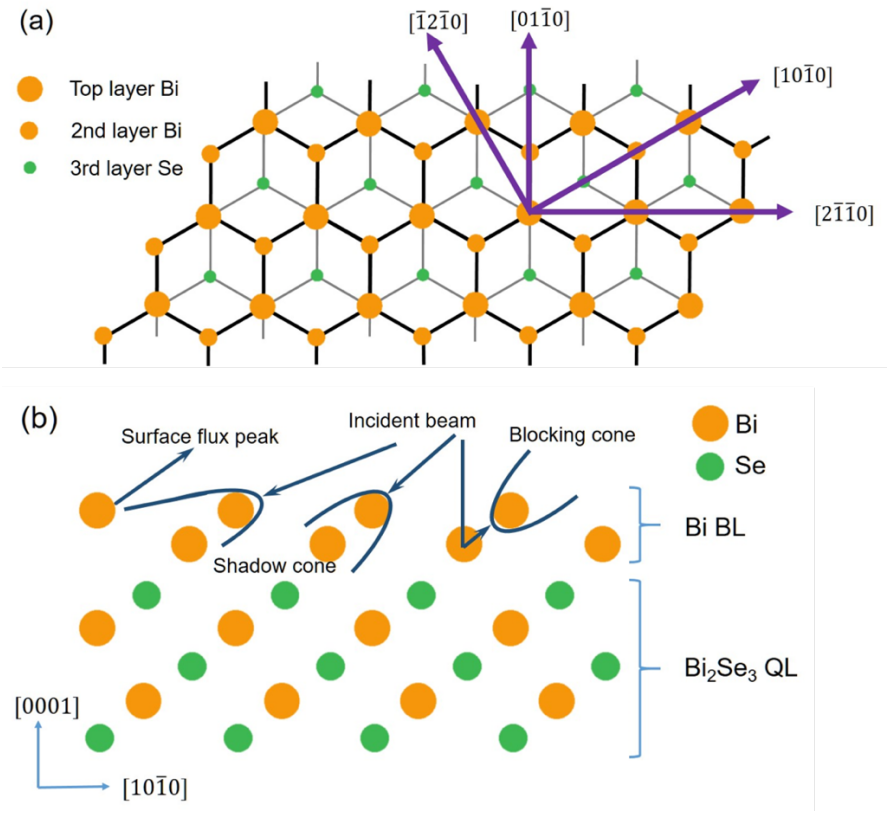

Figure 2. 5. (a) Top view of a single Bi bilayer on a Bi_2Se_3(0001) surface. (b) Side view of the $(1\bar{2}10)$ plane of 1 Bi bilayer on Bi_2Se_3(0001). Representative shadow and blocking cones are indicated in (b).

For the TOF spectra collected here, the incident ion beam is aligned normal to the sample surface and the azimuthal angle with respect to the crystal is adjusted. When the incoming projectiles are normal to the sample, only the outermost three atomic layers are directly visible to the beam for a bulk-terminated Bi_2Se_3 surface structure [5,22]. When the outgoing direction is parallel to the $[10\bar{1}0]$ azimuth at a scattering angle of 125º (35° from the surface normal), as illustrated in Fig. 2.5(a), then both the incident and outgoing trajectories are along low index crystal lattice directions, which is a double alignment

orientation. In this orientation, the projectiles scattered from the second and third layers are blocked from reaching the detector by the first layer atoms, as illustrated by the "blocking cone" in Fig. 2.5(b), so that the SSPs in the spectra represent only those atoms in the outermost layer. Maintaining normal incidence, but using other outgoing azimuthal angles, such as the $[01\bar{1}0]$ direction, produce single alignment orientations in which particles singly scattered from second and third layer atoms can also reach the detector.

In the double alignment TOF spectra collected from clean Bi_2Se_3 shown in the upper left panel of Fig. 2.4, the near absence of the Bi SSP verifies that the surface is Se-terminated [5]. The appearance of the Bi SSP in the single alignment orientation in the upper right panel of Fig. 2.4 shows that Bi is present in the second or third atomic layer. In both alignments shown in Fig. 2.4, the Se SSP decreases in intensity and the Bi SSP increases with Bi deposition, as expected. Note that the cross section for scattering 3.0 keV Na from Bi is ~2.3 times larger than for scattering from Se [37], which needs to be considered when analyzing the ratio of the Se and Bi SSPs.

The diamonds in Fig. 2.6 show how the Se:Bi ratio in single alignment varies with increasing Bi coverage, using the right y-axis. The ratio is obtained by dividing the areas of the SSPs and normalizing by the differential scattering cross sections [37] and MCP efficiencies at the kinetic energy of each SSP [38]. In single alignment, the beam can detect down to the third layer, so that Se SSP disappears after the 2nd Bi bilayer is deposited causing the Se:Bi ratio to become zero.

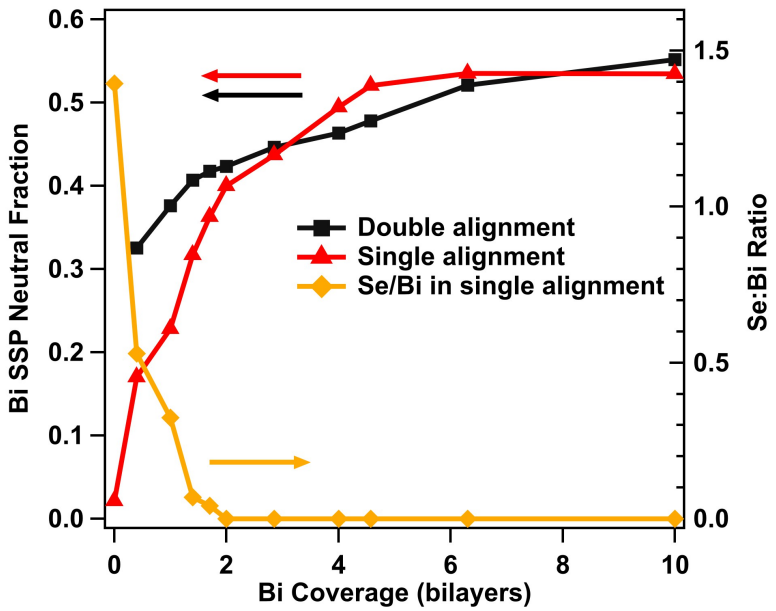

Figure 2. 6. Neutral fractions of the Bi SSP for 3.0 keV Na^+ scattered from Bi_2Se_3 in both single and double alignment along with the Se:Bi ratio calculated from ion scattering data collected in single alignment, shown as a function of Bi coverage.

Figure 2.6 also shows how the Bi SSP NF in both alignments varies with increasing Bi coverage using the left y-axis. The NF in both orientations increases dramatically when the 1st Bi BL is deposited and increases more slowly until they both reach approximately 50% after 4 BLs are deposited. The increase of the NF is consistent with a more metallic surface being produced by the deposited Bi. According to the resonant charge transfer (RCT) model [35] that is normally used to describe the neutralization of scattered low energy alkali ions, the NF in scattering from a conventional solid increases as the local work function above the scattering site is reduced. Therefore, an increase of the neutral fraction with Bi deposition is expected, since the work function of Bi(0001) is 4.27 eV [39], which is lower than the 5.40 eV work function of Bi_2Se_3 [40].

The NFs in single and double alignment are different in scattering from the first Bi bilayer but become the same after the 2nd BL is deposited. The difference in NFs when there is a single BL deposited shows that the chemical environments above the top and bottom Bi atoms in the first bilayer are different. In general, an upward dipole on surface decreases the local work function and thereby increases the measured NF [41,42]. The higher NF in double alignment than in single alignment indicates there are more electrons accumulated under the top Bi atoms in the first bilayer, which is consistent with the calculation in Ref. [43]. Such inhomogeneous distribution of charge can produce a strong electric field and result in the commonly observed Rashba effect [14-17]. When two or more BLs are deposited, the BLs are more freestanding and the chemical environment above the Bi atoms in each BL are then equivalent.

Impact collision ion scattering spectroscopy (ICISS) is performed to investigate the surface structure of the Bi bilayers. ICISS is a specialized version of LEIS in which the intensity of singly scattered ions is monitored as a function of the polar angle between the incident ion beam and the sample surface plane [30,44,45] Figure 2.5(b) illustrates the relationship between representative shadow cones and the atoms in the outermost two atomic layers. At very low incidence angles, i.e., close to the surface plane, each surface atom falls within the shadow cone of its neighbor so that no backscattering occurs. As the polar angle is increased, the edge of each surface atom shadow cone passes through its neighboring atom, causing ions to impact that atom and backscatter at the SSP energy. The ion flux at the edge of a shadow cone is enhanced relative to that of the incident beam due to small angle scattering. Thus, when the incident polar angle is continuously increased, a

maximum appears in the scattering yield, called a flux peak, at the angle at which the edge of the shadow cone passes through the scattering atom. When the edge of a shadow cone formed by one first layer atoms hits the neighboring first layer atoms, as illustrated by leftmost shadow cone in Fig. 2.5(b), the peak is called a surface flux peak (SFP). Other flux peaks appear at larger angles when the shadow cone edge passes through a deeper lying atom.

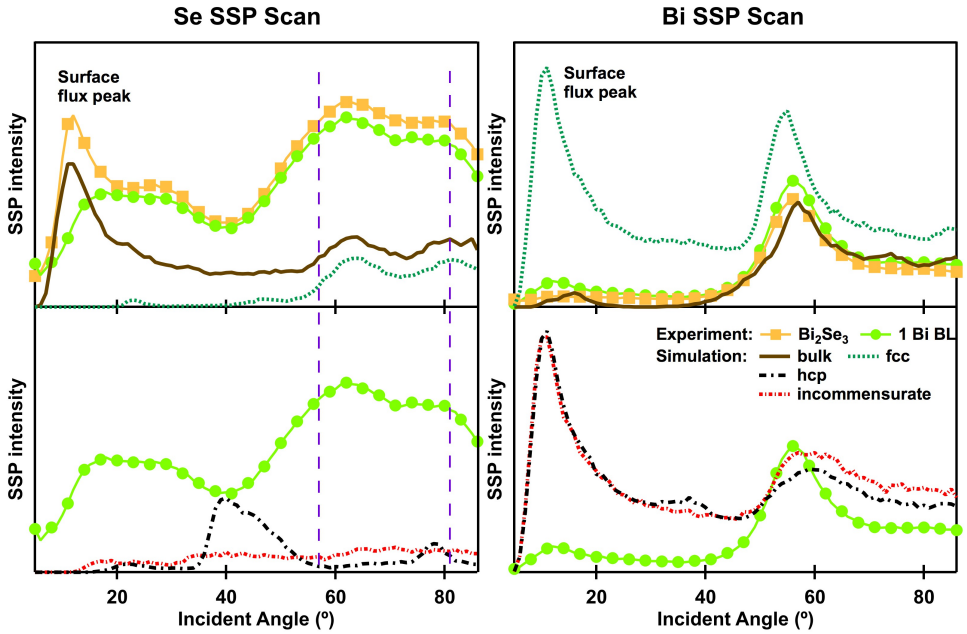

Figure 2. 7. Impact collision ion scattering spectroscopy (ICISS) polar angle scans and simulations for the Se (left panels) and Bi (right panels) SSPs collected from Bi_2Se_3 and the 1 Bi BL covered surface using 3.0 keV Na^+ ions at a scattering angle of 161°. The sample rotates in the polar direction along the $[\bar{1}010]$ azimuth so that the ion incidence direction gradually varies from the surface plane to the surface normal. The surface flux peaks are indicated in upper panels. The legend in bottom right panel applies to all of the graphs.

The symbols in Figure 2.7 show separate ICISS angular scans for scattering from Bi and Se atoms that were collected from as-prepared Bi_2Se_3 (squares) and from that

surface covered with 1 BL of Bi (circles). The clean Bi_2Se_3 surface shows a clear Se SFP at 10º, while there is little Bi SSP intensity in that same angular region, which is expected for a Se-terminated surface. When 1 Bi BL is deposited, the Se SFP attenuates and a Bi SFP grows, which indicates that the surface Se atoms are replaced by Bi. The shapes of Bi SSP scans in the large angle (20°-90°) region are nearly unchanged with Bi coverage, except for a slight enhancement of the peak at 55°, which indicates that Bi adlayer has the same basic atomic structure as a clean Bi_2Se_3 surface with Bi replacing Se.

Molecular dynamics (MD) simulations of ICISS are performed using the Kalypso software package [46] as done in previous work with Bi_2Se_3 [47]. The Thomas-Fermi-Molière repulsive potential using the Firsov screening length, corrected by a factor of 0.8, is used to calculate each projectile-target atom interaction. The acceptance angle used is 4° to match the experimental data. The target model is a two-dimensional $(1\bar{2}10)$ plane as shown in the schematic diagram of Fig. 2.5(b). Periodic boundary conditions are applied parallel to the surface. The atomic positions at the Bi_2Se_3 surface are taken from the structural parameters determined by LEED in Ref. [48]. The vertical distance between the top two atomic layers is set to 1.55 Å. The height of the deposited Bi bilayer is set at 1.71 Å and distance from bottom of the bilayer to the top Se surface atoms is set at 1.96 Å to best fit the experimental data.

The upper panels in Fig. 2.7, which include the experimental data for the Se-terminated Bi_2Se_3 surface as square symbols, also show the simulations performed for the bulk structure as a solid line. Note that the simulations only reproduce single scattering events, while the experimental data contain a background of multiple scattering and out-

of-plane scattering, which is more pronounced for the Se SSP scans because of the lower scattered energy, so that the background intensity of the experimental scans is generally larger than that of the simulations. What is important to focus on when analyzing these data, however, is the existence and positions of particular flux peak features since they indicate when the edge of a shadow cone impacts another atom, which is dependent on the specific crystal atomic surface structure. There is a good agreement between the positions and relative intensities of the flux peaks in the experimental data and simulations for the clean Bi_2Se_3 surface, which indicates the reliability of the simulations in reproducing angular scans for a given surface structure.

For the Bi BL-covered surface, three types of stacking orders are modeled to determine which one best fits the experimental data, which are shown as filled circles in both the upper and lower panels of Fig. 2.7. The simulations for the various stacking orders are separated into either the upper or lower panels to make it easier to distinguish them from each other. The first stacking order assumes that the Bi layer next to uppermost Se layer sits in fcc-like sites, the second places the Bi atoms in hcp-like sites, while the third considers the film to form a superlattice with the substrate. In an fcc-like stacking, the lower Bi atoms in the 1st BL are positioned directly above the 3rd layer Se, as is shown in Fig. 2.5. For hcp-like stacking, the lower Bi atoms in the 1st BL are positioned directly above the 2nd layer Bi. The first two models use the lattice parameter of the substrate (4.14 Å) as that of the Bi adlayer. The simulation of fcc stacking of the Bi bilayer, shown as green dashed lines in the top panels of Fig. 2.7, shares similar features with the experimental Se SSP scan, such as the positions of the rising edge at around 57° and the

peak intensity at 81°, which are marked by vertical dashed lines. In addition, the Bi SSP scan shows an enhancement of the peak at 55° in the simulated scan, which is consistent with the experimental data. The hcp stacking simulation, shown by the black dashed lines in the bottom panels, has an extra feature in the Se SSP scan at around 40°, which is not observed in the experimental data. A superlattice, based on the different lattice parameters of Bi_2Se_3 and Bi, has 69 Bi atoms per single adlayer with a lattice constant of 4.2 Å and 70 Se atoms per substrate layer with a lattice constant of 4.14 Å, is used as the target in the simulation shown by the red dashed lines in the lower panels. This model can be considered as an average of the fcc, hcp and on-top stacking, which has the effect of suppressing all the features in the large angle (20°-90°) region and thus does not provide a good match to the measured scans. Thus, the fcc stacking model provides the best match to the experimental data.

Two different annealing temperatures are used to modify the surface composition and structure. Figure 2.8 shows the LEED patterns collected from an as-deposited 3 BL film and after annealing that sample at different temperatures, while Fig. 2.9 shows the corresponding TOF spectra collected in a double alignment orientation. Before annealing, the LEED in Fig. 2.8(a) shows the satellite spots and the upper panel in Fig. 2.9 shows primarily a Bi SSP, as all of the Se in the substrate is covered by the Bi film.

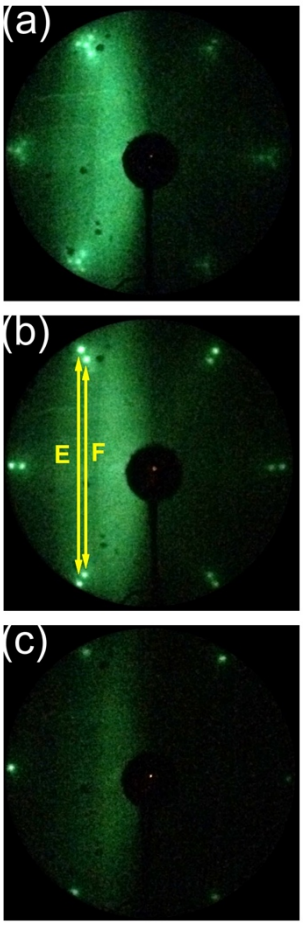

Figure 2. 8. LEED patterns collected from 3 Bi BLs deposited on Bi_2Se_3 (a) before annealing, (b) after annealing at 120°C for 10 hrs, and (c) after annealing at 490°C for 0.5 hrs.

The lower annealing temperature of 120°C is used to investigate the connection between the Bi_2Se_3 surface and the 1st Bi BL. The LEED pattern in Fig. 2.8(b) suggests that the surface Bi crystalizes after annealing at 120°C, which makes the satellite spots disappear, but retains the 1st Bi BL LEED spots, showing the coexistence of the single Bi BL and Bi(0001) bulk patterns. Also, the corresponding TOF spectrum in the middle panel of Fig. 2.9 doesn't show any significant changes in the intensity of either the Se or Bi SSP,

indicating that Bi is not removed in a manner that reveals the substrate. By measuring the distance between the LEED spots (Fig. 2.8(b), lines E and F), corresponding lattice constants of 4.20 Å and 4.57 Å are found, which have a relative difference of about 9%. This can be interpreted as the 2nd and 3rd Bi BLs collapsing under annealing and forming bulk-like Bi single crystal islands, while the 1st Bi bilayer remains stable and covers the substrate as a commensurate layer. The AFM images in Figs. 2.1(f)-(g) confirm this assumption. Figure 2.1(f) was collected from a Bi_2Se_3 surface covered with 3 Bi BLs and annealed at 120°C for 10 hours, and it shows the appearance of holes and islands. The red line C in Fig. 2.1(g) shows the line profile from Fig. 2.1(f), which displays island heights up to 5 BLs and 1 BL deep holes. As the total coverage is 3 Bi BLs, it can be inferred that there is a single Bi BL covering the substrate at the bottom of the holes, while the 2nd and 3rd Bi BLs crystalize to form islands with heights of 4 or 5 BLs.

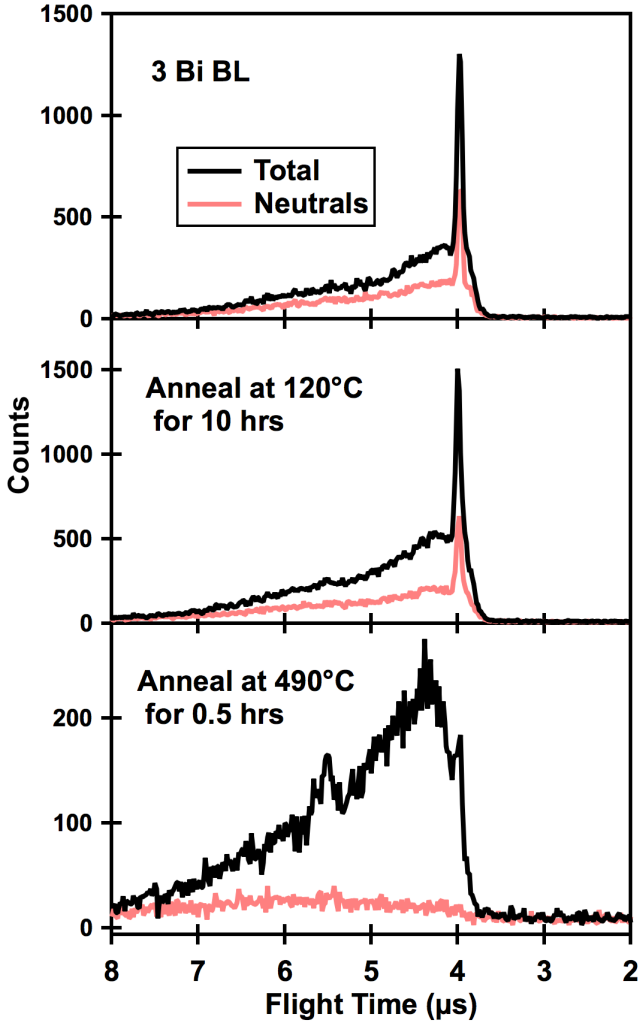

Figure 2. 9. LEIS TOF double alignment spectra collected using 3.0 keV Na^+ ions scattered from 3 Bi BLs deposited on a Bi_2Se_3(0001) surface and after annealing at the indicated temperatures for the indicated times.

When the annealing temperature is 490°C, the surface of the sample reverts to the stable Se-terminated Bi_2Se_3 surface produced by IBA, as shown by the LEED pattern (Fig. 2.8(c)) and TOF spectra (bottom panel of Fig. 2.9). This indicates that the Bi film

sublimates, perhaps along with some substrate QLs, and the surface recrystallizes to produce a fresh Se-terminated surface, as occurs after annealing in the IBA process.

2.4 Discussion

The measurements as a function of Bi deposition are used to determine the growth mechanism of Bi films on Bi_2Se_3 surfaces. A combination of surface analysis tools shows that the first BL grows flat while subsequent layers initially form thin "islands". This is similar to the Stranski–Krastanov (SK) growth mode, indicating a change in the surface energy with film thickness. For Bi/Bi_2Se_3, however, these "islands" are no higher than 2 BLs and coalesce into complete bilayers before thicker islands build up, which is because the bonding between the layers in 2D materials, such as Bi, is relatively weak. Therefore, the growth is not purely SK, and is thus often referred to in the literature as being a quasi bilayer-by-bilayer mode, such as in Refs. [20,49]. These references also observe that Bi grows in a step-flow mode at higher temperature due to the increased surface mobility of Bi adatoms, but the growth of Bi at room temperature is at the boundary of the transition between these two modes.

The first bilayer grows commensurately on fcc-sites of the Se-terminated Bi_2Se_3 surface with a small domain size. As shown in Fig. 2.5(b), if the Bi bilayer sits on fcc-sites of the substrate, the structure of the top layers is basically the same as pristine Bi_2Se_3, except that the first Se layer is replaced by Bi atoms. Therefore, the ICISS scans maintain the features of the original surfaces, except for the loss of the Se surface flux peak. Meanwhile, a simulation of the ICISS scans using a superlattice, in which both the adlayer and substrate maintain their own lattice parameters, does not agree with the experimental

ICISS data. Since the estimated domain size from LEED for 1 BL of deposited Bi is around 19 atoms, it's reasonable to infer that the surface does not consist of large superlattices, but instead of small domains in which the Bi atoms are located at fcc-like sites above the Bi_2Se_3 substrate and the strain between the Bi bilayer and substrate doesn't accumulate over a long range. The lattice parameter measured from the LEED patterns and in Ref. [19] is 4.2 Å, a bit larger than the substrate parameter of 4.14 Å, which may indicate some lateral expansion of the local domains. Thus, the deposited Bi atoms favor forming small domains instead of a superlattice.

When the 2nd bilayer grows, its lattice constant jumps up from 4.20 Å to 4.48 Å, which is a lattice mismatch of 6.7%. Recent work using scanning tunneling microscopy (STM) shows that Bi BLs epitaxially grown on Bi_2Se_3 have a similar large lattice mismatch of 3.3% between the 1st and 2nd Bi BLs [19]. The small difference in the measured lattice mismatch numbers between the present results and those of Ref. [19] are possibly due to the nature of the techniques. STM probes the well-ordered portions of the sample locally, while LEED averages over a large area of the sample surface.

For coverages from 2 to 6 BL, satellite spots appear in the LEED images, indicating that a Moiré structure forms on substrate. The appearance of a Moiré structure can, in principle, be caused by two different scattering mechanisms [50]:

1. Multiple scattering between a substrate and film with different lattice parameters.
2. An undulation of a film that is locked in at nearly commensurate substrate positions, which forms a phase grating for the scattered electrons.

The satellite spots show up when the 2nd Bi BL is deposited and remain until the substrate is covered by 8 BLs. Note that the LEED detection depth is about 5-10 Å [51], which is close to the thickness of 2 Bi BLs. Therefore, the persistence of the satellite spots in LEED indicates that it is most likely due to a periodic undulation of the surface. This conclusion is consistent with the STM study of Ref. [19], where a periodic corrugation is observed for Bi_2Se_3 samples covered by 2 to 5 Bi BLs, which attenuates after more Bi is deposited.

The corrugation between the 1st and subsequent BLs releases the strain caused by the large lattice mismatch of the different materials. Bi_2Se_3 has lattice constant of 4.14 Å while bulk Bi(0001) has lattice constant of 4.54 Å, which is a mismatch of 9.6%. The lattice mismatch is accommodated between the 1st and 2nd Bi BL, rather than between the surface Se and the 1st Bi BL, which is consistent with there being a stronger bond between the top layer Se in the substrate and the 1st Bi BL than between the additional Bi BLs.

Evidence for the relatively strong bond between the 1st Bi BL and the substrate is supported by several of the measurements performed here. After annealing at 120°C, for example, the 1st BL stays in place, as shown by the strong Bi SSP in the double alignment TOF-LEIS spectrum in the center panel of Fig. 2.9. The AFM image in Fig. 2.1(f)) shows that the additional Bi diffuses to form islands, which is a lower energy configuration. The formation of islands releases the strain in the 2nd Bi BL caused by the large lattice mismatch between the 1st and 2nd Bi BL, while the 1st BL Bi doesn't diffuse away due to the stronger bonds between Bi and the surface Se in Bi_2Se_3. The stronger bonding of the 1st BL to the substrate is also indicated by the other AFM images. The 1st Bi BL islands on bare Bi_2Se_3

(Fig. 2.1(b)) and the islands created from the 2nd Bi BL (Fig. 2.1(d)) have different shapes. The single Bi BL islands are more stretched and flat while the 2nd bilayer islands are more triangular shaped. This implies that the bonding between Bi_2Se_3 and a single Bi BL is different than that between Bi BLs. All of this provides evidence of the particular stability of a single BL-covered Bi_2Se_3 surface, consistent with calculations in the literature [21-24].

2.5 Conclusions

The deposition of Bi BLs on Bi_2Se_3(0001) is studied by LEED, LEIS and AFM as a function of coverage and annealing temperature. The first Bi bilayer is locally commensurate, confirming results from the literature that employed different experimental techniques [19]. Furthermore, it is shown here that the BL adsorbs on fcc-sites of the Bi_2Se_3 substrate with an average domain size that is less than 20 atoms in diameter. Charge transfer from the first BL to the substrate is demonstrated by the neutralization of scattered Na^+ ions, and this charge transfer is different for the outermost and second layer Bi atoms in that 1st BL. Satellite spots appear when the 2nd Bi BL is deposited indicating a corrugation of the 2nd BL. Additional deposited Bi grows as free-standing bilayers that follow the corrugation. The outermost surface eventually flattens to become a film with the structure of bulk Bi when more than 8 BLs are deposited. Annealing leaves the 1st Bi BL intact, while the additional Bi diffuses to form taller islands. This indicates a strong interaction between the substrate Bi_2Se_3 QL and the 1st Bi BL, which is consistent with theoretical predictions and other experimental results that suggest that a single Bi BL-covered Bi_2Se_3 surface is a particular stable structure. This explains why Bi-rich surfaces

have been observed to be stable following cleaving under certain conditions [5,22,25,26]. The interaction between Bi BLs is not as strong, which leads to the formation of islands of bulk Bi following annealing of samples with larger coverages.

Bibliography

1. H. Zhang, C.-X. Liu, X.-L. Qi, X. Dai, Z. Fang, and S.-C. Zhang, Nat. Phys. **5**, 438-42 (2009).
2. M. Z. Hasan and C. L. Kane, Rev. Mod. Phys. **82**, 3045-67 (2010).
3. X.-L. Qi and S.-C. Zhang, Rev. Mod. Phys. **83**, 1057-110 (2011).
4. Y. Xia, D. Qian, D. Hsieh, L. Wray, A. Pal, H. Lin, A. Bansil, D. Grauer, Y. S. Hor, R. J. Cava, and M. Z. Hasan, Nat. Phys. **5**, 398-402 (2009).
5. W. Zhou, H. Zhu, and J. A. Yarmoff, Phys. Rev. B **94**, 195408 (2016).
6. P. Hofmann, Prog. Surf. Sci. **81**, 191-245 (2006).
7. S. Murakami, Phys. Rev. Lett. **97**, 236805 (2006).
8. I. K. Drozdov, A. Alexandradinata, S. Jeon, S. Nadj-Perge, H. Ji, R. J. Cava, B. Andrei Bernevig, and A. Yazdani, Nat. Phys. **10**, 664-9 (2014).
9. F. Y. Yang, K. Liu, K. Hong, D. H. Reich, P. C. Searson, and C. L. Chien, Science **284**, 1335-7 (1999).
10. Z. Liu, C.-X. Liu, Y. S. Wu, W.-H. Duan, F. Liu, and J. Wu, Phys. Rev. Lett. **107**, 136805 (2011).
11. G. Bian, Z. Wang, X.-X. Wang, C. Xu, S. Xu, T. Miller, M. Z. Hasan, F. Liu, and T.-C. Chiang, ACS Nano **10**, 3859-64 (2016).
12. F. Yang, L. Miao, Z. F. Wang, M.-Y. Yao, F. Zhu, Y. R. Song, M.-X. Wang, J.-P. Xu, A. V. Fedorov, Z. Sun, G. B. Zhang, C. Liu, F. Liu, D. Qian, C. L. Gao, and J.-F. Jia, Phys. Rev. Lett. **109**, 016801 (2012).

13. L. Miao, Z. F. Wang, W. Ming, M.-Y. Yao, M. Wang, F. Yang, Y. R. Song, F. Zhu, A. V. Fedorev, Z. Sun, C. L. Gao, C. Liu, Q.-K. Xue, C.-X. Liu, F. Liu, D. Qian, and J.-F. Jia, PNAS **110**, 2758–62 (2013).

14. A. Eich, M. Michiardi, G. Bihlmayer, X. G. Zhu, J.-L. Mi, B. B. Iversen, R. Wiesendanger, P. Hofmann, A. A. Khajetoorians, and J. Wiebe, Phys. Rev. B **90**, 155414 (2014).

15. Z. F. Wang, M. Y. Yao, W. Ming, L. Miao, F. Zhu, C. Liu, C. L. Gao, D. Qian, J. F. Jia, and F. Liu, Nature Communications **4**, 1384 (2013).

16. T. Lei, K.-H. Jin, N. Zhang, J.-L. Zhao, C. Liu, W.-J. Li, J.-O. Wang, R. Wu, H.-J. Qian, F. Liu, and K. Ibrahim, J. Phys.: Condens. Matter **28**, 255501 (2016).

17. S. H. Su, P. Y. Chuang, S. W. Chen, H. Y. Chen, Y. Tung, W. C. Chen, C. H. Wang, Y. W. Yang, J. C. A. Huang, T. R. Chang, H. Lin, H. T. Jeng, C. M. Cheng, K. D. Tsuei, H. L. Su, and Y. C. Wu, Chem. Mat. **29**, 8992-9000 (2017).

18. R. Shokri, H. L. Meyerheim, S. Roy, K. Mohseni, A. Ernst, M. M. Otrokov, E. V. Chulkov, and J. Kirschner, Phys. Rev. B **91**, 205430 (2015).

19. K. F. Zhang, F. Yang, Y. R. Song, C. Liu, D. Qian, C. L. Gao, and J.-F. Jia, Appl. Phys. Lett. **107**, 121601 (2015).

20. M. Chen, J.-P. Peng, H.-M. Zhang, L.-L. Wang, K. He, X.-C. Ma, and Q.-K. Xue, Appl. Phys. Lett. **101**, 081603 (2012).

21. Y. N. Zhang, J. Chem. Phys. **143**, 151101 (2015).

22. X. He, W. Zhou, Z. Y. Wang, Y. N. Zhang, J. Shi, R. Q. Wu, and J. A. Yarmoff, Phys. Rev. Lett. **110**, 156101 (2013).

23. M. S. Christian, S. R. Whittleton, A. Otero-de-la-Roza, and E. R. Johnson, Comp. Theor. Chem. **1053**, 238-44 (2015).

24. K. Govaerts, K. Park, C. De Beule, B. Partoens, and D. Lamoen, Phys. Rev. B **90**, 155124 (2014).

25. A. S. Hewitt, J. Wang, J. Boltersdorf, P. A. Maggard, and D. B. Dougherty, J. Vac. Sci. Technol. B **32**, 04E103 (2014).

26. M. T. Edmonds, J. T. Hellerstedt, A. Tadich, A. Schenk, K. M. O'Donnell, J. Tosado, N. P. Butch, P. Syers, J. Paglione, and M. S. Fuhrer, J. Phys. Chem. C **118**, 20413-9 (2014).

27. W. Zhou, H. Zhu, C. M. Valles, and J. A. Yarmoff, Surf. Sci. **662**, 67-73 (2017).

28. J. W. Rabalais, *Principles and applications of ion scattering spectrometry : surface chemical and structural analysis* (Wiley, New York, 2003).

29. G. F. Liu, Z. Sroubek, P. Karmakar, and J. A. Yarmoff, J. Chem. Phys. **125**, 054715 (2006).

30. T. Fauster, Vacuum **38**, 129 (1988).

31. V. V. Atuchin, V. A. Golyashov, K. A. Kokh, I. V. Korolkov, A. S. Kozhukhov, V. N. Kruchinin, S. V. Makarenko, L. D. Pokrovsky, I. P. Prosvirin, K. N. Romanyuk, and O. E. Tereshchenko, Cryst. Growth Des. **11**, 5507-14 (2011).

32. S. Nakajima, J. Phys. Chem. Solids **24**, 479-85 (1963).

33. L. C. Feldman, "Rutherford Backscattering and Nuclear Reaction Analysis", in *Ion Spectroscopies for Surface Analysis*, edited by A. W. Czanderna and D. M. Hercules (Springer Science & Business Media, New York, 2012).

34. C. B. Weare and J. A. Yarmoff, Surf. Sci. **348**, 359-69 (1996).

35. J. P. Gauyacq and A. G. Borisov, J. Phys. Condens. Matter **10**, 6585-619 (1998).

36. Q. B. Lu, R. Souda, D. J. O'Connor, and B. V. King, Phys. Rev. Lett. **77**, 3236-9 (1996).

37. H. Niehus, W. Heiland, and E. Taglauer, Surf. Sci. Rep. **17**, 213-303 (1993).

38. J. Oberheide, P. Wilhelms, and M. Zimmer, Meas. Sci. Technol **8**, 351-4 (1997).

39. M. Muntwiler and X.-Y. Zhu, New J. Phys **10**, 113018 (2008).

40. M. T. Edmonds, J. T. Hellerstedt, A. Tadich, A. Schenk, K. M. O'Donnell, J. Tosado, N. P. Butch, P. Syers, J. Paglione, and M. S. Fuhrer, ACS Nano **8**, 6400–6 (2014).

41. L. Q. Jiang, Y. D. Li, and B. E. Koel, Phys. Rev. Lett. **70**, 2649 (1993).

42. W. Zhou, H. Zhu, and J. A. Yarmoff, Phys. Rev. B **97**, 035413 (2018).

43. T. Hirahara, G. Bihlmayer, Y. Sakamoto, M. Yamada, H. Miyazaki, S. I. Kimura, B. Stefan, and S. Hasegawa, Phys. Rev. Lett. **107**, 166801 (2011).

44. J. A. Yarmoff, D. M. Cyr, J. H. Huang, S. Kim, and R. S. Williams, Phys. Rev. B **33**, 3856-68 (1986).

45. M. Aono and R. Souda, Jpn. J. Appl. Phys. **24**, 1249 (1985).

46. M. A. Karolewski, Nucl. Instr. Meth. Phys. Res. B **230**, 402 (2005).

47. W. Zhou, H. Zhu, and J. A. Yarmoff, J. Vac. Sci. Technol. A **35**, 03E104 (2017).

48. D. D. dos Reis, L. Barreto, M. Bianchi, G. A. S. Ribeiro, E. A. Soares, W. S. e. Silva, V. E. de Carvalho, J. Rawle, M. Hoesch, C. Nicklin, W. P. Fernandes, J. Mi, B. B. Iversen, and P. Hofmann, Phys. Rev. B **88** (2013).

49. G. Jnawali, H. Hattab, C. A. Bobisch, A. Bernhart, E. Zubkov, R. Möller, and M. Horn-von Hoegen, Phys. Rev. B **78**, 035321 (2008).

50. S. Tiefenbachera, C. Pettenkofera, and W. Jaegermannb, Surf. Sci. **450**, 181–90 (2000).

51. K. Heinz, Rep. Prog. Phys. **58**, 637-704 (1995).

Chapter 3

Spatial Distribution of Topological Surface State Electrons in Bi_2Te_3 Probed by Low Energy Na^+ Ion Scattering

3.1 Introduction

Topological insulator (TI) materials are characterized by topological surface states (TSS) that connect the conduction and valence bands [1,2]. The electrons in these TSS are responsible for the novel spin-dependent transport properties of TI materials [2-4]. A detailed characterization of the TSS is part of the ongoing effort to understand the physics of these materials and enable their use in various applications, such as spintronics and quantum computing. An important aspect that has yet to be addressed experimentally is the spatial distribution of the carriers in the TSS.

This chapter contains materials published in W. Zhou, H. Zhu, J. A. Yarmoff, Spatial distribution of topological surface state electrons in Bi_2Te_3 probed by low-energy Na^+ ion scattering, *phys. rev.* B 97, 035413 (2018)

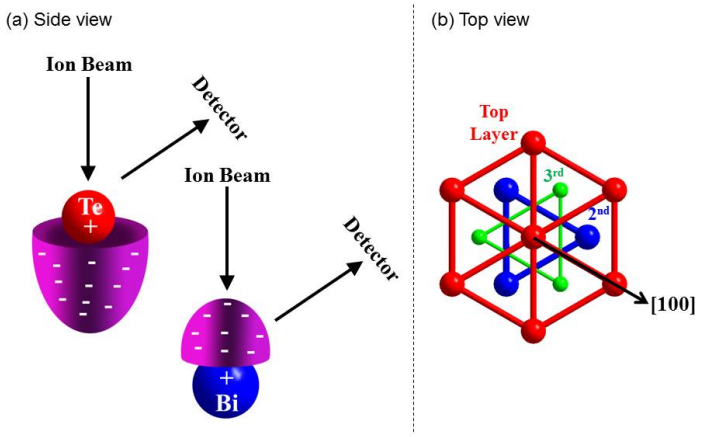

Figure 3. 1. (a) A schematic of the Te and Bi atoms in the outermost atomic layers of single crystal Bi_2Te_3 shown along with the spatial distribution of the TSS electrons as suggested by calculations in the literature. The solid balls indicate the positively charged nuclei, while the cones indicate the electron clouds of the filled TSS, which accumulate below the Te and above the Bi atoms. The incoming ion beam and exit paths for singly scattered projectiles are shown. Note that the diagram is not drawn to scale. (b) A top view of the (001) surface showing the atoms in the first three atomic layers that are visible to the incoming ion beam along the surface normal. The [100] azimuthal direction along which the detector is place is also indicated.

The atomic structure along the (001) cleavage plane of Bi_2Te_3, one of the more common TI materials, consists of stacked two-dimensional quintuple layers (QL) that are ordered as Te-Bi-Te-Bi-Te. Although there has been some question as to whether the material cleaves between QLs causing the surface of actual single crystal materials to be terminated with Te, or with Se for Bi_2Se_3, which is another popular TI with the same basic crystal structure [5-8], other studies have shown that under good ultra-high vacuum (UHV) conditions, the surface is cleaved between QLs and is thus Te- (or Se-) terminated [9,10].

Bi_2Se_3 prepared by ion bombardment and annealing have also been shown to be Se-terminated [11].

First principle calculations have indicated that the TSS in Bi_2Te_3 are located almost completely within the outermost QL, and that the spatial distribution of the electrons is inhomogeneous [12]. Similar charge distributions have been calculated for Bi_2Se_3 [13,14]. The calculations indicate that the electron density near the Fermi energy accumulates below the first and third layer Te (or Se) and above the second layer Bi, as illustrated in Fig. 3.1(a). To our knowledge, however, there has been no experimental verification of the distribution of the charge associated with the TSS.

In this paper, a novel variant of low energy ion scattering (LEIS) is used to probe the charge arrangement at the surface of Bi_2Te_3. LEIS is an experimental technique that has traditionally been used for surface elemental identification and surface atomic structural analysis [15]. It has been further shown, however, that the neutralization probability of scattered low energy alkali ions depends on the surface local electrostatic potential (LEP), sometimes called the local work function, a few Å's directly above the scattering site [16-18]. The larger the work function, the less likely the neutralization, and vice versa. This property of alkali LEIS enables investigations into the inhomogeneity of the LEP for single crystal surfaces that have spatial variations in the valence electron distribution [19] and for surfaces with submonolayer coverages of adsorbates [20-22]. Neutralization in alkali LEIS is used here to image the TSS in Bi_2Te_3 and the results are in good agreement with the calculations. This also demonstrates the usefulness of this method to experimentally probe the distribution of filled surface electronic states in novel materials.

3.2 Experimental Procedure

Single crystals of Bi_2Te_3 were grown using a multi-step heating method [23]. High-purity Bi and Te shot (Alfa Aesar, 5N purity) were mixed stoichiometrically and sealed in an evacuated quartz tube. The tube was heated to 700°C for 60 hours, cooled to 475°C and kept at that temperature for 3 days, and then naturally cooled to room temperature. The material cleaves easily along the (001) plane producing samples around 5 mm in diameter.

The samples are attached to a Ta sample holder by spot-welded Ta strips, cleaved in air several times to obtain a visually flat surface, and then inserted into an ultra-high vacuum (UHV) chamber that has a base pressure of 2×10^{-10} Torr. The instrument contains an entry chamber that enables rapid sample introduction into UHV and transfer onto the foot of a rotatable x-y-z sample manipulator. Surface preparation, low energy electron diffraction (LEED) and LEIS measurements are all performed in this UHV chamber.

Clean and ordered Bi_2Te_3(001) surfaces are prepared by Ar^+ ion bombardment and annealing (IBA), similar to the method used to prepare Bi_2Se_3 described elsewhere [11]. The IBA procedure involves a preliminary degassing at 130°C for two hours, followed by several cycles of 30 min bombardment using 0.5 keV Ar^+ at an average beam flux of approximately 200 nA cm^{-2}, and then a 30 min annealing at 340°C. The ion bombardment acts to remove contaminants from the surface by sputtering, while the annealing recrystallizes the surface. Samples prepared by IBA show a sharp 1x1 triangular LEED pattern confirming that the surface is clean and well-ordered. The LEED pattern is also used to locate the [100] azimuth for LEIS measurements, as described elsewhere [10]. Such

LEIS measurements show that these surfaces are terminated with Te while Bi atoms are located in the second layer, as is expected from the QL structure.

Time-of-flight (TOF) LEIS is performed with the sample at room temperature, using a pulsed Na^+ ion gun (Kimball Physics) with a triple microchannel plate (MCP) detector mounted at the end of a drift tube. The manipulator allows for variation of the azimuthal and polar orientations while the ion gun is mounted on a turntable, which enables independent adjustment of incident polar angle and scattering angle θ. For the present measurements, the incident ion kinetic energy is 3.0 keV and the beam is pulsed at 100 kHz. The incident beam is aimed along the surface normal and θ is fixed at 130°, while the exit direction is along the [100] azimuthal orientation, as indicated in Fig. 3.1(b). There is a pair of parallel plates in the drift tube that can deflect the scattered ions so that spectra of the scattered total yield and neutral species can be collected independently. The entrance to the MCP is grounded to ensure equal sensitivity to charged and neutral projectiles. The ion fluence is kept below 5×10^{13} cm^{-2} so that less than 0.5% of the surface atoms are impacted, which ensures that the data reflect the surface of the unperturbed material.

3.3 Results and Discussion

LEIS spectra display a distinct single scattering peak (SSP) for each element that is directly visible to both the incoming ion beam and the entrance to the drift tube. An SSP represents projectiles that have made a single collision with a surface atom and are then

scattered directly into the detector. The kinetic energy of a SSP is determined primarily by the energy lost in a classical binary elastic collision with an unbound surface atom [24].

Using normal incidence with the Te-terminated Bi_2Te_3 surface, the incoming ion beam can only directly impact atoms in the outermost three atomic layers because the deeper lying atoms are shadowed by these surface atoms, as shown in top view diagram in Fig. 3.1(b). These three upper layers are comprised of Te, Bi and Te atoms, respectively. Along the [100] azimuthal exit orientation, the 1st and 3rd layer Te and the 2nd layer Bi atoms are all in different planes perpendicular to the surface, so that projectiles that undergo a single collision with these atoms can all reach the detector. Note that scattering along the [010] azimuth, which is identical to the outermost three atomic layers of the [100] azimuth, is explicitly discussed in Ref. [11] where it is verified that all such scattered projectiles do not interact with atoms in the neighboring planes at the scattering angle used here and thus contribute to the SSP.

Figure 3.2 shows representative TOF spectra of 3 keV Na^+ scattered from an IBA-prepared Bi_2Te_3 surface. The x-axis indicates the flight time that it takes for a projectile to travel from the sample to the detector, while the y-axis shows the number of scattered projectiles. The dashed line shows the total yield (neutrals and ions), while the solid line indicates the scattered neutral projectiles. SSPs that correspond to Na^+ scattering from Te and Bi, at 4.5 and 3.9 μs, respectively, are riding atop a background of multiply scattered projectiles. This is consistent with the notion that Na^+ scattered from the heavier Bi target atoms would exit the surface with a larger velocity than those scattered from Te, and thus have a shorter flight time. The neutralization probability, or neutral fraction (NF), for

scattering from each element is calculated by dividing the area of the neutral by that of the total yield SSP after subtracting the multiple scattering background, as described in Ref. [20].

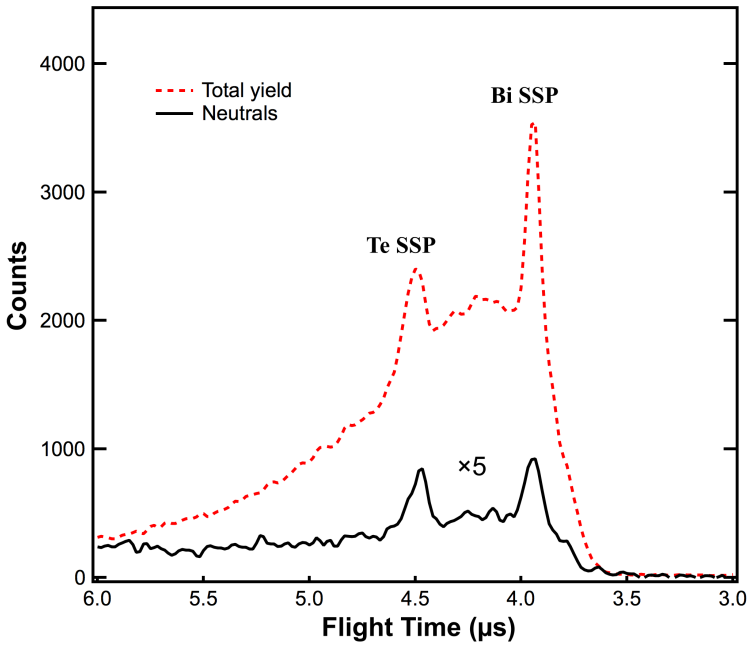

Figure 3. 2. Typical TOF spectra collected for normally incident 3.0 keV Na^+ scattered from Bi_2Te_3 along the [100] azimuth at a scattering angle of 130°. The x-axis is shown in reverse, as smaller flight times indicate higher scattered energies. The solid line shows the scattered neutral projectiles, while the dashed line shows the total scattered yield. The neutral spectrum is multiplied by a factor of 5 for clarity.

The neutralization of low energy alkali ions provides a unique method for measuring the surface LEP [20-22,25]. In the resonant charge transfer model typically used to describe alkali-surface interactions, the ionization level of an alkali-metal atomic particle in the vicinity of a surface shifts upwards towards the Fermi level of the solid due to interaction with its image charge, while it also broadens due to overlap of the projectile and surface wave functions [26]. When the projectile is close to the surface, it can be

neutralized and/or re-ionized by electrons that tunnel between the projectile and the solid. During a low energy ion scattering collision, the neutralization probability is frozen in along the outgoing trajectory through a non-adiabatic process while the projectile is still within a few Å's of the surface, as the electron tunneling rate is smaller than the projectile velocity. The measured NF thus depends on the energy of the ionization level of the probe ion, the degree that the level shifts and broadens near the surface, and the LEP at the "freezing point" just above the scattering site.

Differences in the neutralization probability for scattering from different sites on the same surface indicate that the surface has an inhomogeneous potential. The NF in scattering from an isolated alkali adatom, for example, is generally larger than for scattering from the substrate sites due to the upwards dipole at the adatom site that reduces the LEP [16,27,28]. The dipole is formed by the positively charged alkali adatom and its negative image charge in the solid. This effect is most evident at low coverages, where the inhomogeneity is pronounced and the strength of the individual dipoles is large. A NF increase in scattering from an adatom was also observed for halogen adsorbates, which revealed that the charge within a halogen adatom is internally polarized such that the adatom itself contains an upward pointing dipole at its apex despite its being overall negatively charged [21,29]. This prior work demonstrates that neutralization in alkali LEIS is sensitive to the LEP on a very local, even sub-atomic, scale, and that it is a particularly useful tool for detecting local dipoles on a surface that has an inhomogeneous charge distribution.

In the absence of any surface states, it would be expected that the neutralization probability would be similar for the Bi and Te SSPs, as the bonding is largely covalent so there should be no surface dipoles. Note that there is a small possibility that the Bi SSP would have a larger NF than the Te SSP because the Bi-Te bonds are partially ionic such that the Bi atoms are somewhat more positively charged than the Te atoms, but this should cause only small dipoles along the bond direction and not necessarily along the exit trajectory. Contrary to these considerations, however, Fig. 3.3 shows that for a freshly prepared, well-ordered Bi_2Te_3 surface, the Te SSP has a NF of 0.10 and the Bi SSP has a NF of 0.07, with this difference being larger than the corresponding error bars. Thus, the LEP is inhomogeneous and it is unexpectedly smaller at the Te sites than at the Bi sites.

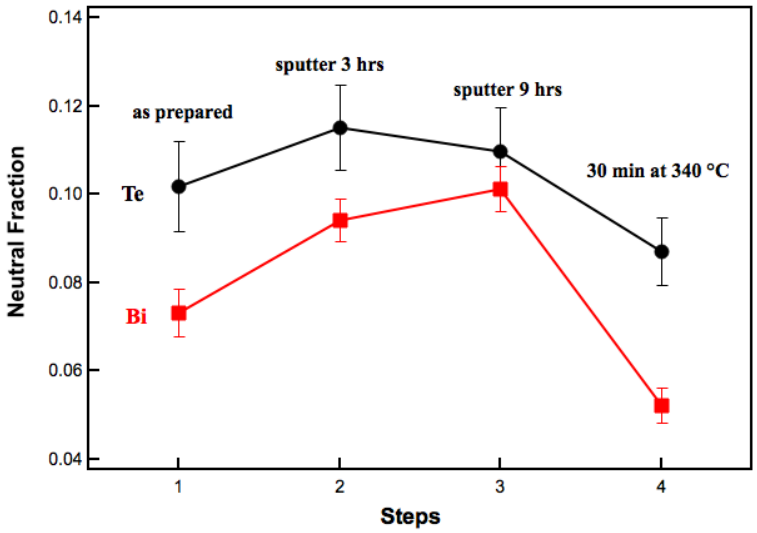

Figure 3. 3. Neutral fractions of the Bi (circles) and Te (squares) SSPs (1) after the initial IBA preparation, (2) after 3 hrs of additional 1.0 keV Ar^+ sputtering, (3) after 9 hrs of additional Ar^+ sputtering, and (4) after 30 min of annealing at 340°C.

It is proposed that this difference in the NFs of the Bi and Te SSPs is related to the specific details of the filled electron distribution of the TSS. As illustrated in Fig. 3.1(a), the calculations in Ref. [12] suggest a charge rearrangement in which TSS electrons accumulate locally below the surface and third layer Te atoms and above the second layer Bi atoms. Because the neutralization is sensitive to the LEP just above the target atoms, the measured neutralization probabilities would not be affected by any charge rearrangement deeper in the material. This charge distribution, which is associated with atoms in the outer three atomic layers, leads to an upward pointing dipole at the Te sites that decreases the LEP and thus increases the NF in scattering from surface Te atoms and a downward pointing dipole at the Bi sites that increases the LEP and decreases the NF in scattering from second layer Bi atoms. The measured NFs thus provide an unambiguous and direct verification of the charge rearrangement associated with the TSS.

To verify the idea that the anomalous NF originates from the special charge redistribution of the surface states, IBA-prepared Bi_2Te_3 samples were subjected to a specific sequence of Ar^+ sputtering and annealing to modify the surface structure, and neutralization measurements were performed after each step. The sputtering was performed with 1.0 keV Ar^+ at a current of approximately 2 μA over the entire sample and holder. Sputtering has the effect of not only removing material from the surface, but also leaving it in a damaged state with a locally amorphous structure [30,31]. For a binary compound, such as Bi_2Te_3, some preferential removal of the lighter element is expected. Additionally, larger scale structures may be formed by ion bombardment, but these would not affect the local nature of the alkali ion neutralization process [32]. After sputtering for 9 hrs, the

LEED pattern almost completely disappears confirming that the surface has become disordered. As seen in Fig. 3.3, the difference between the Bi and Te NFs decreases with sputtering. Note that the difference does not go completely to zero, but this is likely because sputtered materials do exhibit some amount of self-annealing at room temperature [33] so that portions of the surface still have the Te-terminated structure of the active TI and thus contain the TSS electron distribution. When the sputtered sample is annealed at 340°C for 30 min to recrystallize the material, the NF difference and the 1x1 LEED pattern are fully recovered. Note that the absolute values of the NFs after the final annealing are smaller than that after the initial surface preparation, which is likely due to an increase in the overall work function caused by subsurface defects, such as Te vacancies, induced by the lengthy sputtering.

An important question is the role that the position of the Fermi energy with respect to the Dirac point plays in these measurements. When Bi_2Te_3 samples are prepared by IBA or cleaving, there is always a possibility of unintentional doping due to surface defects introduced by sputtering or the mechanical action of cleaving, as well as by surface contamination. This doping affects the position of the Fermi level and can be detected by transport or angular resolved photoelectron spectroscopy (ARPES) measurements. Unfortunately, our apparatus has no way to directly measure the doping level of the sample nor the absolute position of the Fermi energy. Nevertheless, it can be inferred that the small changes to the Fermi energy position would not eliminate the differences in the NFs between the Te and Bi SSPs. Unless the doping was high enough to populate bulk states near the surface with electrons or holes, then the general shape of the localized electrons

in the TSS and the resulting dipoles would still dominate the charge exchange process in Na^+ ion scattering. Evidence for this is the change in the overall NF values after prolonged sputtering, as seen after step (4) in Fig. 3.3. Subsurface vacancy defects, which act as dopants and alter the Fermi energy, cause the overall NFs to shift, but the difference between scattering from Te and Bi is still large once the sample is recrystallized. It can thus be concluded that even if the Fermi energy position does not precisely align with the Dirac point, the LEIS neutralization data is still sensitive to the spatial distribution of the filled TSS states.

Another question to consider is whether the two-dimensional electron gas (2DEG) found on Bi_2Te_3 surfaces [34] plays a role in determining the NF. It is possible that this state increases the electron density between the Te and Bi layers, forming similar dipoles as proposed here for the TSS. The free electrons in such a state would, however, be less localized than those associated with the TSS, based on the parabolic shape of the energy dispersion curve [35], and are thus not be expected to induce strong dipoles and such a large NF difference. In addition, the sputtering measurements provide evidence that can exclude the contribution of this state to the NF difference because the energy band of the 2DEG only exists near the bottom of the conduction band, but the neutral fraction difference remains when the Fermi level shifts. Thus, it is concluded that although the 2DEG may have some contribution, it is not the main cause of the NF difference.

3.4 Conclusions

In summary, the higher neutralization probability for 3.0 keV Na^+ scattered from Te than from Bi sites in Bi_2Te_3 provides experimental verification that the spatial distribution of electrons in the TSS involves an accumulation of charge below the surface Te atoms and above the Bi atoms. This is because the TSS electrons below the Te atoms form a local upwards dipole that reduces the LEP above Te, while the TSS electrons above the Bi sites form a downward dipole that increases the LEP, causing the neutral fraction for Na^+ scattered from Te to be larger than from Bi sites. This result has important implications in understanding fundamental aspects of the electronic structure of TI materials, and in developing their use for various applications. In addition, this work shows that neutralization in low energy alkali ion scattering provides a means for experimentally probing the filled electron distributions in novel materials that rely on conductivity through topological or other types of surface states.

Bibliography

1. M. Z. Hasan and C. L. Kane, Rev. Mod. Phys. **82**, 3045 (2010).
2. X.-L. Qi and S.-C. Zhang, Rev. Mod. Phys. **83**, 1057 (2011).
3. C. Nayak, S. H. Simon, A. Stern, M. Freedman, and S. Das Sarma, Rev. Mod. Phys. **80**, 1083 (2008).
4. Z. Jiang, C.-Z. Chang, M. R. Masir, C. Tang, Y. Xu, J. S. Moodera, A. H. MacDonald, and J. Shi, Nat. Commun. **7**, 11458 (2016).
5. P. M. Coelho, G. A. S. Ribeiro, A. Malachias, V. L. Pimentel, W. S. Silva, D. D. Reis, M. S. C. Mazzoni, and R. Magalhães-Paniago, Nano Lett. **13**, 4517 (2013).
6. M. T. Edmonds, J. T. Hellerstedt, A. Tadich, A. Schenk, K. M. O'Donnell, J. Tosado, N. P. Butch, P. Syers, J. Paglione, and M. S. Fuhrer, J. Phys. Chem. C **118**, 20413 (2014).
7. X. He, W. Zhou, Z. Y. Wang, Y. N. Zhang, J. Shi, R. Q. Wu, and J. A. Yarmoff, Phys. Rev. Lett. **110**, 156101 (2013).
8. A. S. Hewitt, J. Wang, J. Boltersdorf, P. A. Maggard, and D. B. Dougherty, J. Vac. Sci. Technol. B **32**, 04E103 (2014).
9. D. D. dos Reis, L. Barreto, M. Bianchi, Guilherme Almeida Silva Ribeiro, E. A. Soares, W. S. Silva, V. E. de Carvalho, J. Rawle, M. Hoesch, C. Nicklin, W. P. Fernandes, J. Mi, B. B. Iversen, and P. Hofmann, Phys. Rev. B **88**, 041404 (2013).
10. W. Zhou, H. Zhu, and J. A. Yarmoff, Phys. Rev. B **94**, 195408 (2016).
11. W. Zhou, H. Zhu, C. M. Valles, and J. A. Yarmoff, Surf. Sci. **662**, 67 (2017).

12. T. Hirahara, G. Bihlmayer, Y. Sakamoto, M. Yamada, H. Miyazaki, S. I. Kimura, S. Blügel, and S. Hasegawa, Phys. Rev. Lett. **107**, 166801 (2011).

13. W. Zhang, R. Yu, H.-J. Zhang, X. Dai, and Z. Fang, New J. Phys. **12**, 065013 (2010).

14. H. Lin, T. Das, Y. Okada, M. C. Boyer, W. D. Wise, M. Tomasik, B. Zhen, E. W. Hudson, W. Zhou, V. Madhavan, C.-Y. Ren, H. Ikuta, and A. Bansil, Nano Lett. **13**, 1915 (2013).

15. H. Niehus, W. Heiland, and E. Taglauer, Surf. Sci. Rep. **17**, 213 (1993).

16. C. B. Weare, K. A. H. German, and J. A. Yarmoff, Phys. Rev. B **52**, 2066 (1995).

17. K. A. H. German, C. B. Weare, P. R. Varekamp, J. N. Andersen, and J. A. Yarmoff, Phys. Rev. Lett. **70**, 3510 (1993).

18. T. Kravchuk, Y. Bandourine, A. Hoffman, and V. A. Esaulov, Surf. Sci. **600**, L265 (2006).

19. M. Aono, C. Oshima, S. Zaima, S. Otani, and Y. Ishizawa, Jpn. J. Appl. Phys. **20**, L829 (1981).

20. C. B. Weare and J. A. Yarmoff, Surf. Sci. **348**, 359 (1996).

21. J. A. Yarmoff, Y. Yang, and Z. Sroubek, Phys. Rev. Lett. **91**, 086104 (2003).

22. J. P. Gauyacq and A. G. Borisov, J. Phys.: Condens. Matter **10**, 6585 (1998).

23. I. R. Fisher, M. C. Shapiro, and J. G. Analytis, Philosophical Magazine **92**, 2401 (2012).

24. W. J. Rabalais, *Principles and applications of ion scattering spectrometry : surface chemical and structural analysis* (Wiley, New York, 2003).

25. J. J. C. Geerlings, L. F. T. Kwakman, and J. Los, Surf. Sci. **184**, 305 (1987).

26. J. Los and J. J. C. Geerlings, Phys. Rep. **190**, 133 (1990).

27. J. A. Yarmoff and C. B. Weare, Nucl. Instr. Meth. Phys. Res. B **125**, 262 (1997).

28. L. Q. Jiang, Y. D. Li, and B. E. Koel, Phys. Rev. Lett. **70**, 2649 (1993).

29. C. J. Wu and J. E. Klepeis, Phys. Rev. B **55**, 10848 (1997).

30. H. E. Farnsworth, R. E. Schlier, T. H. George, and R. M. Burger, J. Appl. Phys. **26**, 252 (1955).

31. V. S. Smentkowski, Prog. Surf. Sci. **64**, 1 (2000).

32. U. Valbusa, C. Boragno, and F. B. de Mongeot, J. Phys.: Condens. Matter **14**, 8153 (2002).

33. B. Young, J. Warner, and D. Heskett, Surf. Sci. **644**, 64 (2016).

34. M. Bianchi, D. Guan, S. Bao, J. Mi, B. B. Iversen, P. D. C. King, and P. Hofmann, Nat. Commun. **1**, 128 (2010).

35. M. G. Vergniory, T. V. Menshchikova, S. V. Eremeev, and E. V. Chulkov, Jetp Lett+. **95**, 213 (2012).

Chapter 4

Halogen Adsorption and Reaction with $Bi_2(Se,Te)_3$ and $Bi/Bi_2(Se,Te)_3$

4.1 Introduction

Over the past decades, the fundamental science underlying halogen adsorption and reaction with semiconductor materials, such as silicon[1,2] and III-V compound semiconductors,[3-5] has been extensively studied because of the utility of these reactions in modifying surfaces and in forming device structures, typically through reactive ion etching (RIE) in a halogen containing plasma.[6,7] Halogens are also promising candidate molecules for atomic layer etching, which is one of the basic techniques being developed to fabricate nanometer-scale structures.[8,9] If the gaseous halogen reactant is in the stable molecular form, then the halogen-halogen bond must be broken at a reactive surface site before adsorption can occur, which means that halogens do not necessarily adsorb and react with all materials.[10] The adsorption of halogens on surfaces is thus complex and related to the surface termination, atomic structure and number of surface defects.

This chapter contains materials published in Haoshan Zhu, Weimin Zhou and Jory A. Yarmoff, Halogen Adsorption and Reaction with $Bi_2(Se,Te)_3$ and $Bi/Bi_2(Se,Te)_3$, *J. Phys. Chem. C* **122**, 16122 (2018)

Bi_2Se_3 and Bi_2Te_3 are topological insulators (TIs) that have attracted intensive interest in recent years. TIs are promising candidates for superconductor, spintronics and quantum computing applications.[11-13] Bi_2Se_3 and Bi_2Te_3 single crystals are compound two-dimensional (2D) materials composed of weakly interacting quintuple layers (QL) that are arranged as Se-Bi-Se-Bi-Se or Te-Bi-Te-Bi-Te, respectively. The stable surfaces are obtained in a clean environment by cleavage between QLs and are thus terminated with either Se or Te.

The reactions of $Bi_2(Se,Te)_3$ with several gases have been studied extensively because the band structure has been observed to decay over time, the so-called aging effect, which is possibly due to reaction with atmospheric contaminants leading to the formation of surface Se or Te vacancy defects.[14,15] Thus, many investigations have focused on the reactions of $Bi_2(Se,Te)_3$ with O_2 and H_2O.[16-19] NO_2 exposure has also been used to dope the surface and tune the Fermi level of Bi_2Se_3 to coincide with the Dirac point, which is the optimal position for device applications. Using a gas to dope the surface could tune the Fermi level position while not destroying the topological electronic states, as they are protected from nonmagnetic impurities.[18,20] The reaction of Bi_2Se_3 with H_2, which etches surface Se and leaves a Bi bilayer (BL) film on surface, has also been investigated.[21] The reactions of halogens with $Bi_2(Se,Te)_3$ surfaces have not yet been reported, however.

Such reactions may be comparable to halogen reaction with III-V semiconductors in which different surface terminations result in different adsorption behavior.[3,22-25] For example, previous work from our group showed that halogens adsorb on III-V

semiconductors that are terminated with the electron deficient group III atoms and that post-annealing causes the thermal desorption of group III halides, which leads to the surfaces becoming group V-terminated. Halogen reaction with group V-terminated materials leads to a disordered surface, as the halogens adsorb by breaking bonds between the upper two layers and attaching to second layer group III atoms. The preferential reactivity of halogens with particular atoms in a compound material leads to the possibility of selective chemistry in which certain elements can be etched from the surface leading to methods for intentionally altering the termination and surface structure.

The termination of clean TI surfaces has been studied extensively because of its contribution in determining the surface topological states.[26-28] $Bi_2(Se,Te)_3$ surfaces cleaved in ultra-high vacuum (UHV) and those prepared by ion bombardment and annealing (IBA) are naturally terminated with Se or Te,[26,29,30] but theory and experiment have also shown that a surface terminated with an additional Bi BL is particularly stable and energetically favorable compared to the pure QL layer-terminated surfaces.[31-34] Other work has shown that cleaving surfaces in air, or subsequent exposure to air, can lead to a Bi-termination.[16,27] It is thus interesting and important to explore the adsorption and reaction of halogens with TI surfaces that have different terminations.

Ultrathin Bi films on TI substrates have also attracted interest for their nontrivial properties such as a large magnetoresistance and topological edge states,[35,36] and an isolated Bi(0001) bilayer (BL) is also a 2D topological insulator.[37,38] Hetero-structure engineering with Bi BLs and other materials provide the ability to control the electronic

properties and fabricate unique device structures.[39-43] Among them, bottom-up methods such as molecular beam epitaxy (MBE) are the most commonly used fabrication techniques, although a top-down approach has also been reported.[21] Bi can react with halogen gases directly as does Si, which provides the possibility of etching Bi in a top-down process and forming a nanoscale device structure. This provides a further motivation for exploring halogen reaction with TIs and Bi-covered TIs.

The present paper presents a low energy electron diffraction (LEED) and low energy ion scattering (LEIS) study of halogen adsorption and etching of pure $Bi_2(Se,Te)_3$ and Bi-covered $Bi_2(Se,Te)_3$ surfaces. It is found that some molecular halogens adsorb on clean Se- or Te-terminated $Bi_2(Se,Te)_3$ surfaces, but the materials are not etched by the halogens. In contrast, surfaces covered by Bi thin films are more reactive to halogens and the Bi films are etched away by heating at a relatively low temperature.

4.2 Experimental Procedure

Single crystal Bi_2Se_3 and Bi_2Te_3 boules are grown using a multi-step heating method[44] following the procedures described previously.[26,45] The material cleaves easily along the (0001) plane producing approximately 5 mm diameter samples. The samples are attached to a transferable tantalum (Ta) sample holder for measurements using spot-welded Ta strips.

The surface analysis measurements are performed in an ultra-high vacuum (UHV) main chamber with a base pressure of 2×10^{-10} Torr or below. This main chamber contains a sputter gun for sample cleaning, solid-state electrochemical cells for halogen

exposure,[46] optics for LEED, and the equipment needed for LEIS that is described below. The sample holders are transferred from a load-lock chamber onto a manipulator that allows for positioning in the x-y-z directions and rotations about both the polar and azimuthal axes. The surfaces are heated radiatively using an e-beam filament mounted behind the sample without a bias voltage, as the annealing temperatures needed to prepare clean and ordered $Bi_2(Se,Te)_3$ surfaces are rather low. The sample is held at room temperature during halogen exposures and spectra collection.

Ion bombardment and annealing (IBA) is used to prepare clean and well-ordered surfaces.[29] For preparing Se-terminated $Bi_2Se_3(0001)$, the IBA process involves 30 min of 500 eV Ar^+ ion bombardment at a current density of 2.5×10^{12} cm^{-2} sec^{-1} with the sample at room temperature, followed by annealing in UHV at 490°C for 30 min.[26] Te-terminated $Bi_2Te_3(0001)$ surfaces are produced in the same way except that the annealing temperature is 340°C.

A MBE system is attached to the main chamber in a manner that enables samples to be transferred between the chambers while remaining under UHV. This MBE system is used for growing Bi films onto the $Bi_2(Se,Te)_3$ surfaces, which are held at room temperature during growth. Bi is evaporated at a rate of 1.45 Å min^{-1} from a Knudsen cell heated to 530°C, with the rate being calibrated by a quartz crystal microbalance (QCM). The coverages of Bi are reported here in units of bilayers.

Low energy ion scattering (LEIS) is performed in the main UHV chamber. The ions are produced from a thermionic emission Na^+ ion gun (Kimball Physics) that can be operated in a constant current mode or can produce a pulsed beam of ions. The scattered

particles are collected by either of two detectors, as described below. The gun is mounted on a rotatable turntable that allows for the scattering geometry to be adjusted. For the present data, the incident ion kinetic energy is fixed at 3.0 keV.

The first detector is used for time-of-flight (TOF) spectroscopy.[47] The beam is pulsed at 100 kHz and incident normal to the sample surface, while the scattered projectiles are collected at scattering angles of 125° for Bi_2Se_3 and 130° for Bi_2Te_3. The detector consists of a triple microchannel plate (MCP) array located at the end of a 0.57 m long flight tube. The entrance to the MCP detector is held at ground potential so that the sensitivity to ions and neutrals are equal. A bias voltage of 400 V applied to deflection plates in the flight tube separates the scattered ions from the neutrals. Ground potential and 400 V are applied interchangeably to enable the simultaneous collection of separate spectra for the total scattered yield and the scattered neutrals. The MCP detection sensitivity decreases rapidly as the kinetic energy of the scattered projectiles falls below about 2 keV,[48] which is part of the reason that a second detector is employed.

The second detector is a Comstock electrostatic analyzer (ESA), operated in constant pass energy mode, that collects only the scattered ions.[49] It is used here for detecting the presence of lighter elements, in particular Cl, as the TOF setup does not allow for a scattering angle less than 100° at which Na scatters from Cl at a kinetic energy that is below the detection limit of the MCP. Instead, the ESA accelerates the charged projectiles before they impact the internal dual MCP array so that there is no low energy cutoff. For the ESA data collected here, the gun is set to provide a scattering angle of 40°, which

enables the detection of adsorbed Cl. The beam is incident at a 70° angle from the surface normal when making these measurements.

Bromine and chlorine molecules are produced from solid-state electrochemical cells based on a silver bromide or chloride pellet, respectively, which are mounted on silver foils.[22,46] The cells are heated to approximately 120°C to enable ionic conduction through the pellet and operated at a current of about 10 μA. The exposures are reported here in terms of the cell current integrated over time and given in units of μA hrs. Spectra are collected immediately after each halogen exposure. Samples are also annealed at 130°C after halogen adsorption to explore etching of the material. The exposure or annealing time is varied for different halogens and sample materials to ensure saturation or complete reaction, which is identified when there are no further changes in the spectra with additional exposure or annealing.

4.3 Results

Bi_2Se_3, Bi_2Te_3 surfaces and Bi BL-capped $Bi_2(Se,Te)_3$ surfaces are exposed to bromine and chlorine molecules to study the reactions of halogens with TI surfaces. Section III.A describes how LEIS is used to obtain information from these materials using the clean surfaces as examples. The results for halogen exposure and post-annealing for clean Se- and Te-terminated surfaces are presented in section III.B. Section III.C provides results for halogen adsorption onto the TI surfaces when they are covered with a Bi film. Section III.D explores the chemical reactions that occur when the halogen-covered Bi-terminated surfaces are annealed.

A. Low Energy Ion Scattering from TI surfaces

LEIS spectra are used to investigate the surface composition and structure. As an example, the upper panels of Fig. 4.1 show total yield (ions plus neutrals) TOF spectra collected from clean Te-terminated Bi_2Te_3. In LEIS, the target can be considered to consist of unbound atoms located at the lattice sites, as the bonding energy is much smaller than the kinetic energy of the incoming projectiles. These kinetic energies are large enough that the binary collision approximation can be used, which treats the process as a sequence of isolated elastic collisions between the projectile and individual target atoms.[50] The most prominent features in the spectra are the single scattering peaks (SSPs), which ride on a background due to multiple scattering. A SSP corresponds to a projectile that experiences a single hard collision with a surface atom and backscatters directly into the detector, losing energy primarily through a classical elastic collision. Thus, the larger the mass of the target atom, the higher the scattered energy of the singly scattered projectile. Note that the time scale in the figure is reversed so that increasing energy of the scattered projectiles is towards the right. In Fig. 4.1, the Te SSP is at 4.7 μs and the Bi SSP is at 4.1 μs. The intensity of a given total yield SSP is basically proportional to the number of atoms that are directly visible to both the incoming ion beam and the detector multiplied by the differential scattering cross section at that scattering angle. In this case, the cross section for scattering from Te is about 1.5 times less than for scattering from Bi.[51]

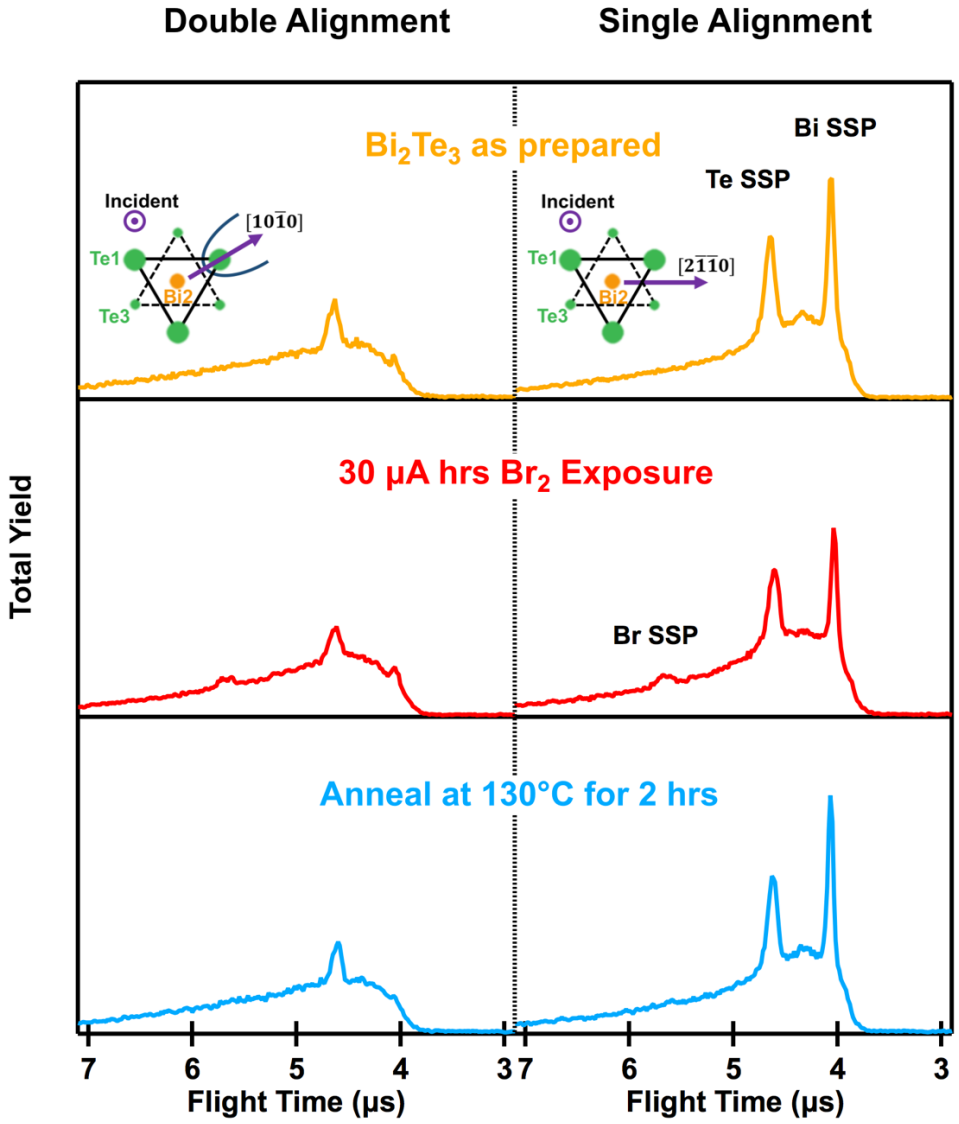

Figure 4. 1. LEIS total yield TOF spectra collected from (top) clean Bi_2Te_3, (middle) after 30 μA hrs of Br_2 exposure, and (bottom) post-annealing at 130 °C for 2 hrs. The 3.0 keV Na^+ ion beam is incident normal to sample surface and the detector is positioned at a scattering angle of 130°. The upper panels include top view schematics with projections of the azimuthal directions of the scattered beams, the atoms and their layer numbers indicated. The spectra in the left panel are collected along the $(1\bar{2}10)$ azimuthal plane, which is a double alignment configuration. The spectra in the right panel are collected in single alignment by rotating the azimuthal angle with respect to the detector by 30°. The intensities of the spectra are normalized to each other using the ion beam current measured on the sample and the data collection time.

The relative orientations of the ion beam, sample and detector can be used to make the LEIS spectra reflect only particular atoms in a single crystal sample by aligning the incident beam and/or the detector along low index crystalline directions.[26,52] For example, a normally incident beam, i.e., along the [0001] direction of $Bi_2(Se,Te)_3$, will only directly impact the three outermost atomic layers, as the atoms beneath are completely shadowed by the upper layers when using ions in the low energy regime. Such an arrangement in which the beam is incident along a low index direction, but the detector is not, is called single alignment. In addition, the detector can also be positioned along a low index crystalline direction so that projectiles scattered from deeper lying atoms are blocked from reaching the detector by the outermost atoms, which is called double alignment. For Bi_2Te_3 surface, as indicated by the schematic diagram in the upper left panel of Fig. 4.1, when the detector is along the $(1\bar{2}10)$ azimuthal plane and positioned 50° from the surface normal, the projectiles scattered from 2nd layer Bi and 3rd layer Te atoms are completely blocked by the first layer Te atoms and single scattering is only possible from the first atomic layer.[26,34] The diagram includes a projection onto the surface plane of a representation of the blocking cone that prevents projectiles scattered from the 2nd and 3rd layers from reaching the detector. The same protocol is used for the Bi_2Se_3 surface except that the detector is positioned at 55º from the surface normal. The upper panels in Fig. 4.1 show spectra collected in both single and double alignment from clean Bi_2Te_3. In single alignment, which probes the composition of the outermost three atomic layers, both Te and Bi SSPs are visible. The Bi SSP is very small in double alignment but it is not absent, however, which is possibly due to surface defects and/or edge atoms at surface terraces. It

can thus be concluded that the clean IBA-prepared Bi_2Te_3 surface is primarily Te-terminated, as is expected from the bulk crystal structure of this 2D layered material.

B. Halogen exposure of Se- or Te-terminated bulk $Bi_2(Se,Te)_3$

The middle and lower panels in Fig. 4.1 show TOF spectra collected from Bi_2Te_3 after exposure to Br_2 and then after post-annealing, respectively. The clean sample is exposed to 10 μA of Br_2 and TOF spectra are collected after each hour of exposure. The spectra do not change after 2 hrs of exposure, which means that the Br coverage has saturated. The middle panel of Fig. 4.1 shows spectra collected after 30 μA hrs of Br_2 exposure, i.e., the saturated surface. A peak at 5.5 μs that corresponds to the Br SSP appears after Br_2 exposure, and the intensities of the Te and Bi SSPs reduce in both alignments, which indicates that Br adsorbs on the surface and partially shadows or blocks the substrate atoms. Note that the cross section for scattering from Br is about 2.3 times less than for scattering from Bi,[51] so that the small size of the Br SSP corresponds to more adsorbed Br than it may appear.

Table 4. 1. Coverage of surface atoms calculated from ratios of the single scattering peak areas in LEIS TOF spectra collected in both double and single alignment orientations from Bi_2Te_3 and 1.5 Bi BL covered Bi_2Te_3 surfaces before and after exposure to Br_2 and Cl_2. No data is presented for chlorine coverages as the Cl SSP is not visible in the TOF spectra.

	Double Alignment			Single Alignment		
	Br	**Te**	**Bi**	**Br**	**Te**	**Bi**
Bi_2Te_3 as prepared		1±0.06	0.10±0.01		1.6±0.1	1±0.04
30 µA hrs Br_2 exposure	0.56±0.07	0.74±0.06	0.16±0.02	0.58±0.06	1.05±0.05	0.66±0.03
30 µA hrs Cl_2 exposure		0.98±0.09	0.07±0.01		1.47±0.15	0.91±0.09
Bi covered Bi_2Te_3		0.34±0.04	0.89±0.04		0.43±0.04	1.52±0.05
10 µA hrs Br_2 exposure	0.8±0.1	0.22±0.04	0.26±0.03	0.68±0.06	0.47±0.04	1.03±0.04
10 µA hrs Cl_2 exposure		0.44±0.07	0.31±0.04		0.40±0.06	0.93±0.07

The coverages of all of the surface elements before and after halogen exposure to Bi_2Te_3 are summarized in Table 4.1. The SSP areas are calculated by integrating the peaks after subtracting the multiple scattering background, with the errors being determined by assuming that they are purely statistical, i.e., the square root of the total number of counts in each SSP. The coverages are calculated from the ratio of the Br SSP to Bi SSP after normalizing by the relative differential scattering cross-sections[51] and the MCP detection efficiency.[48] The coverages are calibrated using the assumption that the number of visible surface Te atoms in double alignment and the number of visible Bi atoms in single alignment from the as-prepared surfaces are each 1 monolayer (ML). Here, 1 ML is defined

to be the number of atoms in the first layer of the defect-free TI surface. It is found that the coverage of Br on the saturated surface is about 0.57 ML, and the Te SSP attenuates by about 30% in both alignments, while the Bi SSP only decreases in single alignment. The clean surface has 0.1 ML of Bi visible in double alignment, which implies that the surface contains Te vacancy defects, which could be sites that Br adatoms attach to. The Bi SSP in double alignment has no decrease after adsorption, however, and the amount of adsorbed Br is larger than the number of defects that are present on the clean surface. Thus, it appears that Br does stick to the Te-terminated surfaces at sites other than defects. After Br adsorbs, the LEED pattern gets weaker and shows no higher order spots, indicating that the adsorbed Br atoms are not ordered and the surface itself may be somewhat disordered, possibly by the breaking of some Bi-Te bonds, which could be the reason why the Bi SSP in double alignment increases in intensity after Br exposure.

After reaching a saturation coverage of Br, annealing at 130°C for 2 hrs is performed to explore the surface reactions. The post annealing spectra in the bottom panels of Fig. 4.1 are very similar to those collected from clean bulk Bi_2Te_3, meaning that the Br SSP disappears and the Te and Bi SSPs recover their intensity. This indicates that the bonding between Br and the surface is weak and this low temperature annealing easily breaks the bonds. Br adatoms likely recombine into Br_2 as they desorb and any broken Bi-Te bonds reform, thus restoring the intact Bi_2Te_3 substrate.

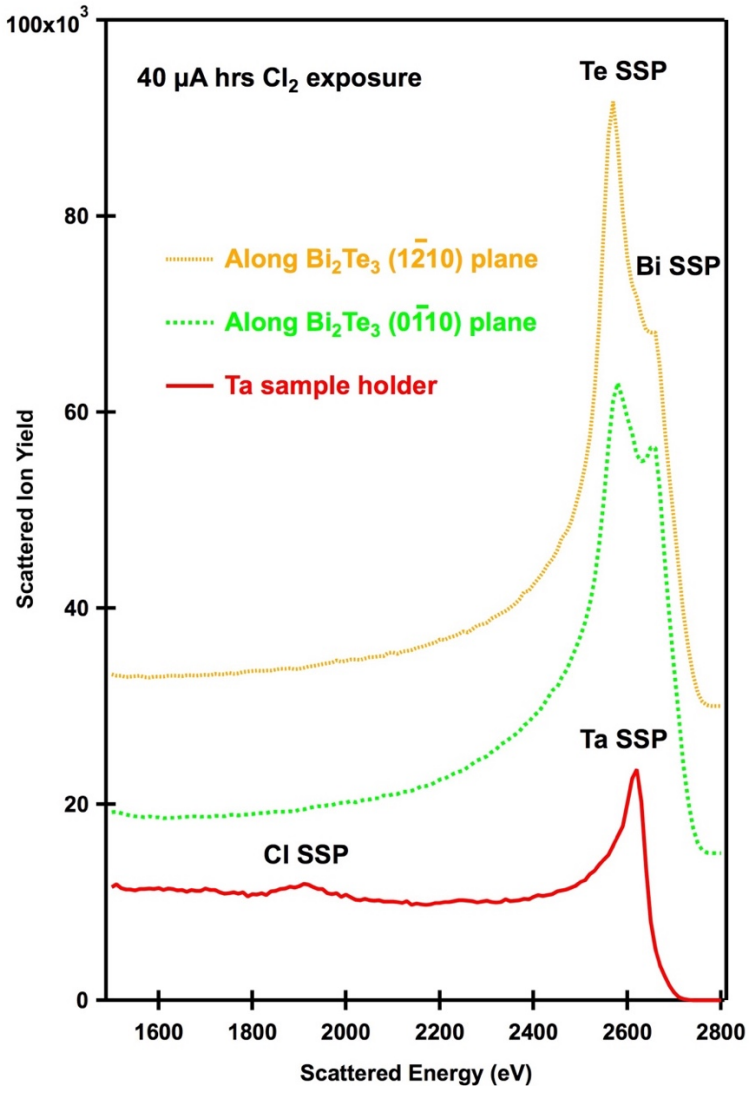

Figure 4. 2. 3.0 keV Na^+ LEIS spectra collected with the ESA from Bi_2Te_3 and the Ta sample holder following 40 µA hrs of Cl_2 exposure. The beam is incident at a 70° angle from the surface normal and the detector is positioned at a scattering angle of 40°. The spectra are offset vertically for clarity.

As Cl has a much smaller atomic mass than Br, it cannot be detected directly by TOF due to the poor efficiency of the MCP in measuring particles with low kinetic energy. Table 4.1 shows that after Cl_2 exposure, the amounts of Bi and Te at the surface do not substantially change, as in the case of Br_2 exposure. This implies that many fewer Cl atoms

stick to Bi_2Te_3 than do Br atoms. To confirm this, spectra were collected with the ESA for 3.0 keV Na^+ scattering at 40° along two different azimuths from Bi_2Te_3 and from the Ta sample holder after 40 μA hrs of exposure to Cl_2, as shown in Fig. 4.2. Note that neither of these orientations correspond to alignments along a low index crystalline direction, but the small scattering angle means that the beam and detector are close to the surface plane, so that most of the deeper lying atoms are shadowed by the surface atoms making this measurement primarily sensitive to the outermost couple of atomic layers. After Cl_2 exposure, a Cl SSP appears in the spectrum collected from the sample holder, which verifies that the sample has been exposed to Cl_2 and that this orientation is sensitive to the presence of Cl on the surface. The amount of Cl adsorbed on the sample holder is calculated to be roughly 0.5 ML. A Cl SSP is not, however, observed in spectra collected from the samples under either azimuthal alignment, which indicates that a significant amount of Cl_2 does not stick to the Bi_2Te_3 surface. In the same way, there is no Cl SSP visible in ESA spectra collected following Cl_2 reaction with Se-terminated Bi_2Se_3 surfaces (not shown). Note that the possibility that a small number of Cl atoms adsorb at vacancy defects cannot absolutely be excluded from these data, however, because under the grazing incident angles used in collecting the ESA spectra, Cl atoms adsorbed at a vacancy defect could be shadowed by surface Se or Te atoms. In addition, the differential cross section for 3.0 keV Na scattering at 40° from Cl is 1.65 times smaller than for Br,[51] so that the measurement is less sensitive to small amounts of Cl. Finally, note that the TOF spectra collected after Cl_2 exposure and annealing are identical to those following Br_2 reaction, suggesting that if

any chlorine were adsorbed that it recombines and desorbs under annealing thus restoring the clean surface in a similar manner as annealing a Br_2-reacted surface.

Additionally, for the ion scattering methods employed here, neither the TOF apparatus nor the ESA have sufficient energy resolution to distinguish the Br from the Se SSP due to their close atomic masses (M_{Se} = 79 u, M_{Br} = 80 u). Thus, the information that can be gleaned from the LEIS spectra is that Br does not adsorb at a site that shadows the Bi SSP in single alignment, implying that it does not adsorb to any great degree. Another measurement method is needed, however, to absolutely confirm that Br_2 does not stick to Se-terminated Bi_2Se_3.

C. Halogen exposure of Bi/$Bi_2(Se,Te)_3$

Halogen exposures and annealing are also performed on Bi-capped $Bi_2(Se,Te)_3$ samples. Deposited Bi grows in a quasi bilayer-by-bilayer mode on $Bi_2(Se,Te)_3$ surfaces as Bi bilayers oriented along the (0001) direction, as they have a similar hexagonal lattice structure.[53-55] The first Bi BL has a relatively strong bonding to the Bi_2Se_3 surface and sits flat on both surfaces. Additional deposited Bi grows epitaxially on top of previous bilayers, but multilayers start to form before any particular bilayer fully covers the surface, which leads to films that are not uniformly thick. To ensure that the samples are covered with at least one Bi BL while not yet being bulk-like Bi, a slight excess of 1.5 Bi BLs is grown on the samples prior to halogen exposure.[55]

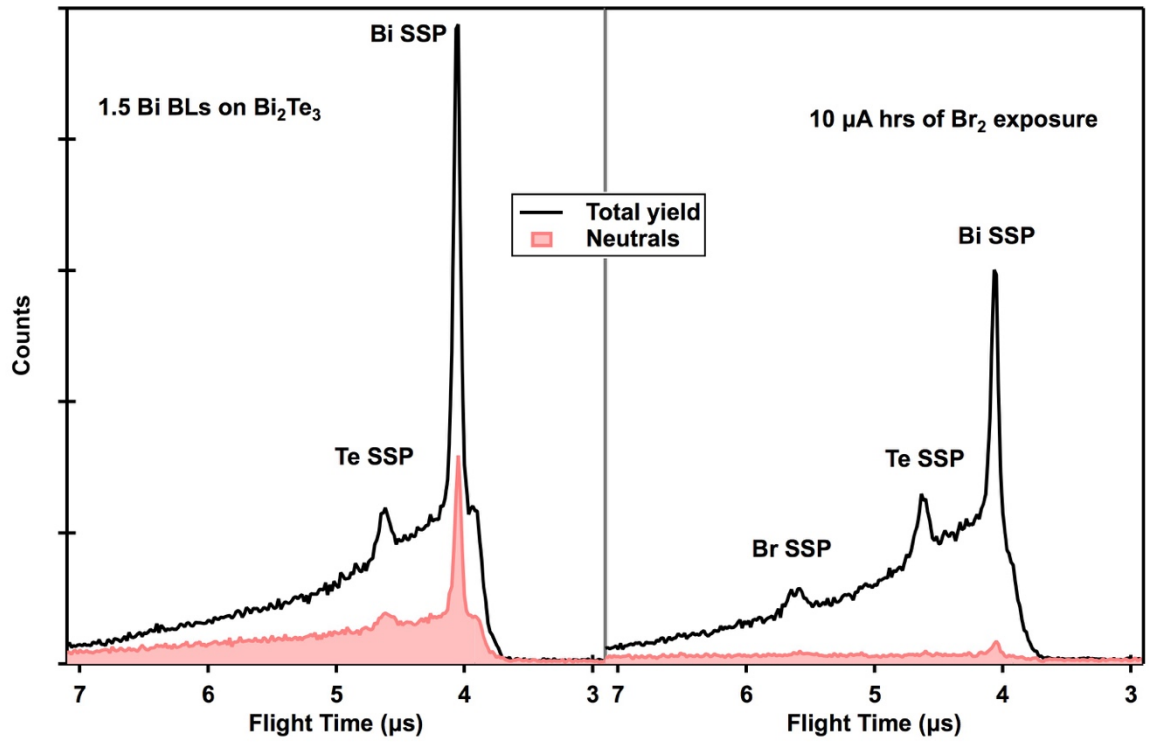

Figure 4. 3. 3.0 keV Na^+ LEIS TOF spectra collected from surfaces of (left) 1.5 Bi BL covered Bi_2Te_3, and (right) after exposure to 10 μA hrs of Br_2. All of the spectra are collected in single alignment. The solid black lines show the total yield spectra of scattered projectiles, while shaded areas show spectra of the scattered neutral particles.

It is found that Br_2 and Cl_2 always adsorb on the Bi BL-terminated $Bi_2(Se,Te)_3$ surfaces. Figure 4.3 shows TOF spectra collected from Bi/Bi_2Te_3 before and after Br_2 adsorption. All of the spectra are collected in single alignment and the upper curves are the total scattered yields. For the surface covered with a 1.5 Bi BL film, the spectra in the left panel show a prominent Bi SSP, as expected. There is still some Te SSP remaining, but it is much less than that observed from clean Bi_2Te_3 and is due to the fact that the ion beam and detector can still see 3rd layer Te atoms in single alignment. It is also possible there are

a small number of pinholes in the Bi film that expose some of the underlying Te-terminated surface. After the sample is reacted with 10 μA hrs of Br_2, the Br SSP appears and the Bi SSP intensity is reduced while the Te SSP intensity is unchanged, as seen in the right panel. This suggests that the Br attaches atop to the surface Bi atoms and not to any of the exposed Te atoms.

The number of visible Bi, Te and Br surface atoms before and after halogen adsorption is summarized in the lower three rows of Table 4.1. After a 10 μA hrs exposure of Br_2, more than 0.7 ML of Br atoms adsorb on surface, which is more than the amount that attaches to clean Bi_2Te_3. The large decrease of the Bi surface coverage shows that Br favors atop adsorption to Bi sites over Te. The same decrease of the Bi SSP intensity occurs for the Cl_2 exposed Bi/Bi_2Te_3, as seen in Table 4.1, and for halogen exposed Bi/Bi_2Se_3 surfaces (data not shown), which further illustrates how halogen atoms attach directly to Bi much more readily than to Te or Se.

Another useful feature of TOF spectra is that the site-specific neutral fraction (NF) can be obtained for each SSP, which provides information on the local electrostatic potential (LEP) directly above the scattering site.[47,56,57] According to resonant charge transfer (RCT) model typically used to model neutralization in low energy alkali ion scattering, when the projectile is close to a surface, the ionization level shifts and broadens while electrons tunnel between states in the surface and the ionization level. The measured neutralization probability thus depends on the relative positions of the projectile's ionization level and the surface Fermi energy at a “freezing distance”, which is typically a few Å’s above the scattering site,[58] as the process is non-adiabatic due to the high

velocity of the projectile. The NF for each SSP is calculated by dividing the integrated area of the neutral SSP by the area of total SSP after subtracting the multiple scattering background. The RCT model predicts that the NF in scattering from conventional solids decreases when the Fermi level moves down as the LEP (sometimes referred to as the local work function) increases, and vice versa, which has been confirmed by multiple experiments and calculations.[56,57,59]

Table 4. 2. The neutralization probability for 3.0 keV Na^+ singly scattered from Bi in a single alignment orientation from clean Bi_2Se_3, Bi_2Te_3 and these samples covered with 1.5 BL of Bi before and after 10 μA hrs exposures to Br_2 and Cl_2.

	Bi_2Se_3	Bi_2Te_3
Clean IBA prepared surface	**4.9% ± 0.4%**	**6.3% ± 0.7%**
After Br_2 exposure	**4.7% ± 0.5%**	**6.0% ± 0.5%**
After Cl_2 exposure	**3.1% ± 0.3%**	**5.3% ± 0.9%**
1.5 Bi BL covered surface	**43% ± 1%**	**34% ± 1.1%**
After Br_2 exposure	**7.1% ± 0.7%**	**6.8% ± 0.5%**
After Cl_2 exposure	**6.6% ± 0.5%**	**8.3% ± 1.1%**

For halogens adsorbed on bulk $Bi_2(Se,Te)_3$ and $Bi/Bi_2(Se,Te)_3$ hetero-structures, the electronegative halogen adatoms are expected to behave as hole donors, i.e., as p-dopants. P-doping of an initially intrinsic semiconductor would normally increase the work function and consequently decrease the NF,[60] but the neutralization in alkali LEIS depends on the surface potential and not necessarily on the bulk doping since the surface Fermi level could be pinned by surface states. In Fig. 4.3, the shaded areas show the TOF

spectra of the scattered neutrals, and that ratio of the SSP areas in the neutral to the total yield spectra indicate the NFs. Table 4.2 summarizes the Bi SSP NFs in single alignment before and after Br_2 and Cl_2 exposure of clean $Bi_2(Se,Te)_3$, Bi/Bi_2Se_3 and Bi/Bi_2Te_3.

When clean Bi_2Se_3 and Bi_2Te_3 surfaces are exposed to halogens, the first three rows of Table 4.2 show very subtle decreases in the NF, which indicate a minor p-doping effect. The difference is too small compared to the relative large error limits, however, to be conclusive. One reason for such a small change is that halogens only loosely, or do not at all, adsorb on the Te- and Se-terminated surfaces, so that the LEP and thus the NF, do not change significantly. Additionally, clean Bi_2Se_3 and Bi_2Te_3 have high work functions that result in very low NFs, so that changes in the NF are difficult to discern.

When $Bi_2(Se,Te)_3$ is covered with a Bi BL, the Bi SSP NF increases from that of the clean surface because Bi has a lower work function than $Bi_2(Se,Te)_3$ and serves as an electron donor. Thus, the NF becomes more sensitive to changes in the LEP that occur after halogen exposure. In comparing the left and right panels of Fig. 4.3 and the data in the last three rows of Table 4.2, it is seen that after Br_2 exposure of Bi_2Te_3, both the Te and Bi NFs decline. When Cl_2 is reacted with a $Bi/Bi_2(Se,Te)_3$ hetero-structure, TOF spectra show no Cl peak, but there is a reduction of the intensity of the Bi SSP and the overall NF decreases in a similar manner as for Br_2 (data not shown). All of the Bi SSP NFs drop to the 6%-8% level following halogen adsorption. Note that because the Se and Te SSPs are small, it is difficult to get accurate values for their NFs, but it is clear from the spectra that they also decrease. Since the halogen atoms adsorb to Bi sites, it can be assumed that they form local downward pointing dipoles by attracting electrons from the surface Bi atoms, thus

increasing the work function. The NF data thus confirm that these dipoles increase the LEP at the Bi sites, which then decreases the measured NFs, as is expected for p-doping.[61]

In addition, a special LEED pattern is found when a surface prepared by deposition of 1.5 Bi BLs on Bi_2Se_3 is exposed to 6.7 μA hrs of Br_2, as shown in Fig. 4.4. Note that the background is brighter on the left side of the image due to inhomogeneities in the phosphor screen. The pattern consists of higher order six-fold spots in the center, which means that the Br on the surface forms a $\sqrt{3} \times \sqrt{3}\, R30°$ superstructure. The LEED pattern stays the same when more Br_2 is reacted, indicating that the surface Br coverage is saturated by this point. The higher order LEED pattern is only found on the $Br_2/Bi/Bi_2Se_3$ system, as the other Bi BL-covered surfaces all maintain a well ordered 1x1 LEED pattern with the Bi BL crystal periodicity following halogen adsorption.

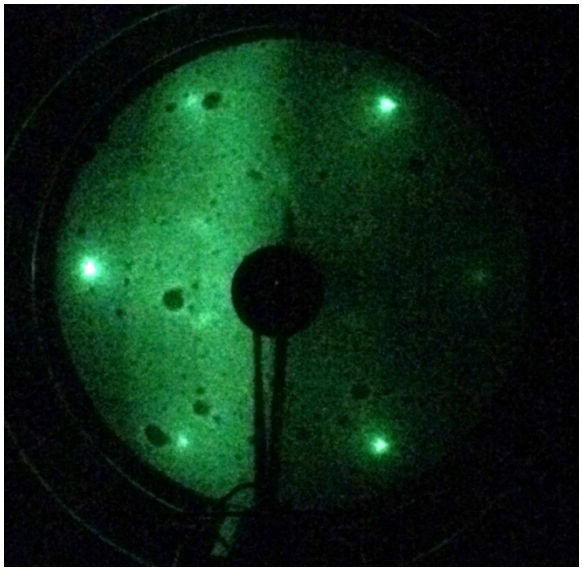

Figure 4. 4. LEED pattern collected from 1.5 Bi BL covered Bi_2Se_3 exposed to 6.7 μA hrs of Br_2. The image is collected using a beam energy of 21.8 eV and shows a $\sqrt{3} \times \sqrt{3}\, R30°$ LEED pattern.

D. Annealing of halogen-exposed surfaces

A 130°C low temperature anneal is performed on halogen-exposed $Bi_2(Se,Te)_3$ samples to study any surface chemical reactions. It is found that the TOF spectra have no change in either peak intensity nor NF after annealing. This is either because the halogens do not stick to the surfaces, or that they are so weakly bonded to the Se or Te surface atoms that a low temperature heating causes the halogen atoms to desorb leaving the Se or Te-terminated sample surfaces intact.

For Bi-covered surfaces, however, etching of the Bi atoms occurs after annealing. Figure 4.5 shows double alignment TOF spectra collected from Bi_2Te_3 after Bi is deposited, following exposure to Br_2, and then after it is post-annealed. The upper spectrum shows mostly the Te SSP, confirming the Te-termination. The next spectrum was collected after deposition of 1.5 Bi BLs, which causes a Bi SSP to appear. There's still some Te SSP visible, which is likely due to an incomplete coverage of Bi. A control experiment is then performed by annealing the Bi-capped sample at 130°C for 3 hrs in the absence of Br, as indicated by the dashed curve. In this case, the TOF spectra do not show any decrease of the Bi SSP intensity nor an increase of the Te SSP, which excludes the possibility of surface Bi being removed by annealing alone.

The Bi/Bi_2Te_3 surface is then exposed to 10 μA hrs of Br_2, which leads to the appearance of a Br SSP and the attenuation of the Te and Bi SSPs, as seen in the 4^{th} spectrum of Fig. 4.5. The attenuation of the Bi is greater than in Fig. 4.3 as only the top layer atoms are detected in double alignment, which implies that the Br attaches mainly to the top layer Bi atoms. Then, after annealing Br_2-reacted Bi/Bi_2Te_3 at 130°C for 2 hrs, the

Br SSP disappears and the Bi SSP is smaller than in the TOF spectra collected from the original Bi-capped sample. After an additional cycle of Br_2 exposure and annealing, as shown in the bottom spectrum of Fig. 4.5, the Bi SSP is very small and the Te SSP gets even larger, becoming close in area to that of clean Bi_2Te_3. This indicates that Bi atoms are removed during the annealing, presumably through an etching process in which Br reacts to form the volatile $BiBr_3$ compound, or $BiCl_3$ in the case of chlorine adsorption. This etching reaction removes the surface Bi and reveals the Te-terminated surface of the bulk sample.

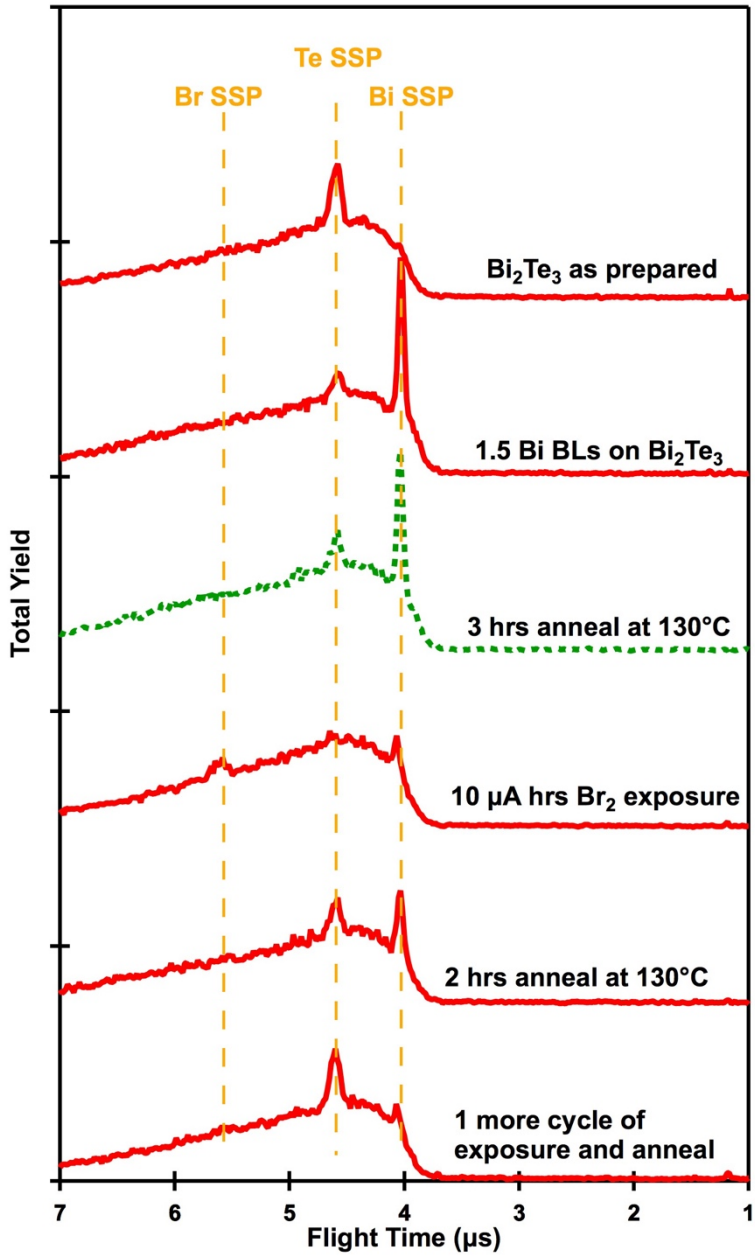

Figure 4. 5. 3.0 keV Na^+ LEIS TOF spectra collected in double alignment from the surfaces of clean Bi_2Te_3 and after subsequent treatments as marked in the graph and described in the text.

Figure 4.6 is a summary of the proportion of surface Bi remaining following halogen adsorption onto and annealing of samples covered with Bi films, shown as a

function of halogen exposure. Different annealing times are used in each cycle for the different reactants and materials, as these are determined by the time that it takes for the TOF spectra to saturate, i.e., display no further changes after additional annealing. The proportion of Bi is calculated as the ratio of the Bi SSP area to the total Bi and Se SSP areas. Note that the difference in differential cross section for Na scattering from Bi and Se (or Te) and MCP efficiency for scattered projectiles with different kinetic energies is included in calculating the total areas. The amount of surface Bi remaining declines with the amount of halogen exposure, and eventually reaches the value of pristine $Bi_2(Se,Te)_3$ bulk materials. It is thus found that the Bi films on $Bi_2(Se,Te)_3$ are etched away by a thermally driven reaction with adsorbed Br or Cl and that the removal of Bi is nearly complete with a sufficient halogen exposure.

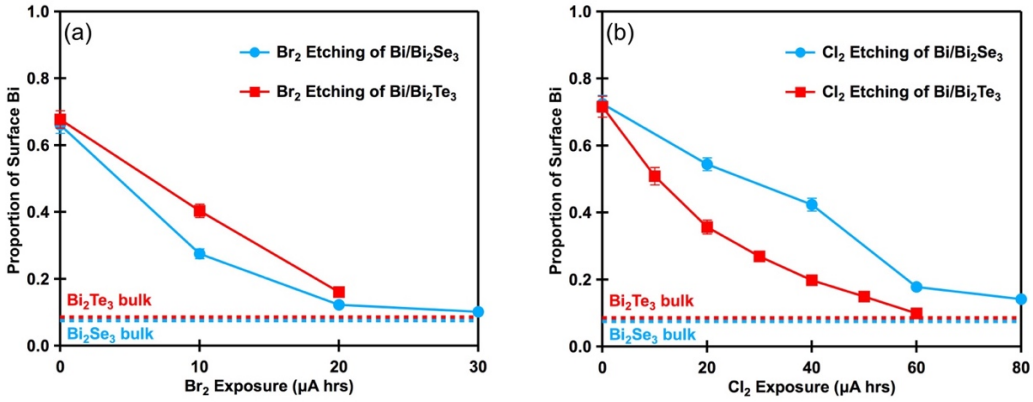

Figure 4. 6. The proportion of Bi on the surface following cycles of halogen adsorption and annealing shown as a function of (a) Br_2 exposure and (b) Cl_2 exposure. The annealing is performed at a temperature of 130°C for 4 hrs with Br_2 etching of Bi/Bi_2Se_3, 2 hrs for Br_2 etching of Bi/Bi_2Te_3, 0.5 hrs for Cl_2 etching of Bi/Bi_2Se_3 and 2 hrs for Cl_2 etching of Bi/Bi_2Te_3. The horizontal dashed lines indicate the proportions measured from the clean bulk-terminated surfaces. Note that the error bars associated with many of points are smaller than the symbols.

4.4 Discussion

According to the LEIS spectra, a limited number of Br atoms stick to clean Te-terminated Bi_2Te_3, but no evidence of Cl adsorption on either QL-terminated Bi_2Se_3 or Bi_2Te_3 is found. This is unexpected as Cl_2 is normally more reactive than Br_2, but it is partially because Cl atoms have a smaller LEIS cross-section than Br due to its smaller mass making Cl more difficult to discern in the spectra. In addition, it is possible that some Cl is located beneath the top layer, such as at a defect site so that it is directly attached to a Bi atom, which would cause the Cl to be shadowed by surface Te or Se atoms.

The bulk-terminated TI surfaces remain intact after annealing, either because halogens do not adsorb, or they are only weakly bonded. The limited bonding of molecular halogens to clean TIs may be partially due to these surfaces being relatively inert two-dimensional van der Waals materials, or because the terminating Se or Te atoms are unreactive because they have filled valence electron orbitals and are thus unable to break a halogen-halogen bond. The fact that Se- and Te-terminated surfaces are basically inert also means that halogens do not replace the surface atoms and bond to second layer Bi atoms. Thus, for clean and defect-free $Bi_2(Se,Te)_3$, it is difficult to modify the surface structure with halogen molecules. This is unlike the behavior of group V-terminated III-V semiconductor surfaces, for which halogens are able to dissociate and break the bonds between atoms in the first two layers and attach to the reactive group III atoms in the second layer.[22,23]

The notion that Br can occupy Se or Te surface vacancy defect sites is worth exploring, however, as the aging effect is believed to result in n-doping from such

vacancies, so that filling the vacancies with an electronegative halogen atom may help to compensate for the missing surface atoms and restore the Fermi level position. For the samples used in the present work, however, the number of surface vacancy defects is small and cannot account even for the small amount of Br that adsorbs on Te-terminated Bi_2Te_3 surfaces. Thus, this is still an open question and a future experiment is planned in which vacancy defects are intentionally produced to determine if halogen do occupy such sites, and whether they act as p-dopants when they do.

For Bi-covered surfaces, however, halogen adsorption readily occurs. There are a couple of reasons why this is likely. First, although Bi is also a two-dimensional van der Waals material, the manner in which it grows on $Bi_2(Se,Te)_3$ is not through a pure layer-by-layer process[53-55] so that there are many defects, step edges, etc., at which the Br_2 or Cl_2 can readily react and dissociatively adsorb. Second, due to Bi being more electropositive than Se or Te, it can more easily give up electrons to induce the dissociative adsorption of halogen molecules. This is parallel to the behavior of group III-terminated III-V semiconductors in which the surface atoms have empty surface states that readily react with halogens.[22,24] There is a large decrease of the NF of the Bi SSP with halogen adsorption implying that the bonding Bi atoms donate charge to Cl or Br, which is expected as Bi is more metallic and halogens are more electronegative. This implies a decrease of the Fermi level position and that halogens are a good candidate for p-doping of Bi-covered heterostructures. Further confirmation of this hypothesis can be obtained from angle-resolved photoelectron spectroscopy (ARPES), transport or other measurements.

In addition, etching of the halogen-covered Bi films occurs when the samples are heated. This is similar to the processes that occur with various other semiconductor surfaces that are etched by adsorbed chlorine and bromine.[2,3] For silicon reacted with Cl_2, for example, SiCl and $SiCl_2$ form on the surface and annealing a Cl-saturated surface to about 700 K removes the surface Si atoms in the form of gaseous silicon chlorides. For III-V semiconductors, such as GaAs reacted with Cl_2, volatile chlorides of both Ga and As form and the material is etched when the sample is heated at ~650 K.[3] A similar reaction can be inferred to occur between surface Bi and halogens. Halogens initially adsorb dissociatively to the surface Bi atoms. When heated, Bi then reacts with the halogens to form volatile molecules, which are most likely the stable Bi trihalides. The melting point of $BiCl_3$ is 227°C and 219°C for $BiBr_3$, which are relatively low, and the vapor pressures of $BiCl_3$ and $BiBr_3$ at 130°C are each about 3×10^{-3} Torr.[62] Thus, when the halogen-covered samples are heated to only 130°C, the halides evaporate leaving bare Se- or Te-terminated surfaces.

4.5 Conclusion

Halogen adsorption and reaction with Bi_2Se_3, Bi_2Te_3 and $Bi/Bi_2(Se,Te)_3$ surfaces is systematically studied by LEIS and LEED. Br_2 can weakly bond to Te-terminated Bi_2Te_3 surfaces, while Cl_2 shows no evidence of adsorption to either Bi_2Se_3 or Bi_2Te_3. The halogens that do stick desorb after a light annealing, leaving the surface intact and with the same structure as that of the initially prepared clean surface, which further demonstrates the inertness of QL-terminated TIs. Halogens do readily adsorb on Bi BL films on TI

substrates, however, and they have a p-doping effect. The Bi bilayers are etched by adsorbed halogens when heated at a relatively low temperature, which provides the possibility of fabricating nanoscale Bi structures through a controlled etching process, in addition to other methods such as direct bottom-up growth[40] and focused ion beam nanofabrication.[63]

Heterostructures consisting of a small number of Bi layers deposited onto TI or other materials are attracting more interest and such a controlled halogen chemical reaction suggests a way to manipulate the amount of Bi on the surfaces. The atomic level etching process requires further study, however, such as determining if the etching occurs in a layer-by-layer mode and whether the etching starts from the edge or if it is isotropic. Future studies from our group will focus on the effects of halogen adsorption on vacancy defect sites, especially monitoring any electronic structure changes such as Fermi level shifting.

Bibliography

1. H. F. Winters and J. W. Coburn, Surf. Sci. Rep. **14**, 161 (1992).

2. C. M. Aldao and J. H. Weaver, Prog. Surf. Sci. **68**, 189 (2001).

3. W. C. Simpson and J. A. Yarmoff, Annu. Rev. Phys. Chem. **47**, 527 (1996).

4. A. Jenichen and C. Engler, J. Chem. Phys. B **105**, 1956 (2001).

5. Y. Liu, A. J. Komrowski, and A. C. Kummel, Phys. Rev. Lett. **81**, 413 (1998).

6. I. Adesida, A. Mahajan, E. Andideh, M. A. Khan, D. T. Olsen, and J. N. Kuznia, Appl. Phys. Lett. **63**, 2777 (1993).

7. N. D. Altieri, J. K.-C. Chen, L. Minardi, and J. P. Chang, J. Vac. Sci. Technol. A **35**, 05C203 (2017).

8. T. Kubota, T. Baba, S. Samukawa, H. Kawashima, Y. Uraoka, T. Fuyuki, and I. Yamashita, Appl. Phys. Lett. **84**, 1555 (2004).

9. K. J. Kanarik, S. Tan, W. Yang, T. Kim, T. Lill, A. Kabansky, E. A. Hudson, T. Ohba, K. Nojiri, J. Yu, R. Wise, I. L. Berry, Y. Pan, J. Marks, and R. A. Gottscho, J. Vac. Sci. Technol. A **35**, 05C302 (2017).

10. R. G. Jones, Prog. Surf. Sci. **27**, 25 (1988).

11. H. Zhang, C.-X. Liu, X.-L. Qi, X. Dai, Z. Fang, and S.-C. Zhang, Nat. Phys. **5**, 438 (2009).

12. M. Z. Hasan and C. L. Kane, Rev. Mod. Phys. **82**, 3045 (2010).

13. X.-L. Qi and S.-C. Zhang, Rev. Mod. Phys. **83**, 1057 (2011).

14. H. J. Noh, H. Koh, S. J. Oh, J. H. Park, H. D. Kim, J. D. Rameau, T. Valla, T. E. Kidd, P. D. Johnson, Y. Hu, and Q. Li, Europhys. Lett. **81**, 57006 (2008).

15. M. Bianchi, R. C. Hatch, D. Guan, T. Planke, J. Mi, B. B. Iversen, and P. Hofmann, Semicond. Sci. Technol. **27**, 124001 (2012).

16. M. T. Edmonds, J. T. Hellerstedt, A. Tadich, A. Schenk, K. M. O'Donnell, J. Tosado, N. P. Butch, P. Syers, J. Paglione, and M. S. Fuhrer, J. Phys. Chem. C **118**, 20413 (2014).

17. L. V. Yashina, J. Sa´nchez-Barriga, M. R. Scholz, A. A. Volykhov, A. P. Sirotina, V. S. Neudachina, M. E. Tamm, A. Varykhalov, D. Marchenko, G. Springholz, G. Bauer, A. Knop-Gericke, and O. Rade, ACS Nano **7**, 5181 (2013).

18. M. Koleini, T. Frauenheim, and B. Yan, Phys. Rev. Lett. **110**, 016403 (2013).

19. H. M. Benia, C. Lin, K. Kern, and C. R. Ast, Phys. Rev. Lett. **107**, 177602 (2011).

20. D. Hsieh, Y. Xia, D. Qian, L. Wray, J. H. Dil, F. Meier, J. Osterwalder, L. Patthey, J. G. Checkelsky, N. P. Ong, A. V. Fedorov, H. Lin, A. Bansil, D. Grauer, Y. S. Hor, R. J. Cava, and M. Z. Hasan, Nature **460**, 1101 (2009).

21. R. Shokri, H. L. Meyerheim, S. Roy, K. Mohseni, A. Ernst, M. M. Otrokov, E. V. Chulkov, and J. Kirschner, Phys. Rev. B **91**, 205430 (2015).

22. W. K. Wang, W. C. Simpson, and J. A. Yarmoff, Phys. Rev. Lett. **81**, 1465 (1998).

23. Y. Liu, A. J. Komrowski, and A. C. Kummel, J. Chem. Phys. **110**, 4608 (1999).

24. K. N. Eltsov and A. A. Vedeneev, JETP Letters **99**, 466 (2014).

25. B. Han, C. Cha, and J. Weaver, Phys. Rev. B **56**, 4966 (1997).

26. W. Zhou, H. Zhu, and J. A. Yarmoff, Phys. Rev. B **94**, 195408 (2016).

27. A. S. Hewitt, J. Wang, J. Boltersdorf, P. A. Maggard, and D. B. Dougherty, J. Vac. Sci. Technol. B **32**, 04E103 (2014).

28. M. V. Kuznetsov, L. V. Yashina, J. Sánchez-Barriga, I. I. Ogorodnikov, A. S. Vorokh, A. A. Volykhov, R. J. Koch, V. S. Neudachina, M. E. Tamm, A. P. Sirotina, A. Y. Varykhalov, G. Springholz, G. Bauer, J. D. Riley, and O. Rader, Phys. Rev. B **91**, 085402 (2015).

29. W. Zhou, H. Zhu, C. M. Valles, and J. A. Yarmoff, Surf. Sci. **662**, 67 (2017).

30. D. D. dos Reis, L. Barreto, M. Bianchi, G. A. S. Ribeiro, E. A. Soares, W. Simões e Silva, V. E. de Carvalho, J. Rawle, M. Hoesch, C. Nicklin, W. P. Fernandes, J. Mi, B. B. Iversen, and P. Hofmann, Phys. Rev. B **88**, 041404(R) (2013).

31. Y. N. Zhang, J. Chem. Phys. **143**, 151101 (2015).

32. M. S. Christian, S. R. Whittleton, A. Otero-de-la-Roza, and E. R. Johnson, Comp. Theor. Chem. **1053**, 238 (2015).

33. K. Govaerts, K. Park, C. De Beule, B. Partoens, and D. Lamoen, Phys. Rev. B **90**, 155124 (2014).

34. X. He, W. Zhou, Z. Y. Wang, Y. N. Zhang, J. Shi, R. Q. Wu, and J. A. Yarmoff, Phys. Rev. Lett. **110**, 156101 (2013).

35. F. Y. Yang, K. Liu, K. Hong, D. H. Reich, P. C. Searson, and C. L. Chien, Science **284**, 1335 (1999).

36. Z. Liu, C.-X. Liu, Y. S. Wu, W.-H. Duan, F. Liu, and J. Wu, Phys. Rev. Lett. **107**, 136805 (2011).

37. S. Murakami, Phys. Rev. Lett. **97**, 236805 (2006).

38. I. K. Drozdov, A. Alexandradinata, S. Jeon, S. Nadj-Perge, H. Ji, R. J. Cava, B. Andrei Bernevig, and A. Yazdani, Nat. Phys. **10**, 664 (2014).

39. G. Bian, Z. Wang, X.-X. Wang, C. Xu, S. Xu, T. Miller, M. Z. Hasan, F. Liu, and T.-C. Chiang, ACS Nano **10**, 3859 (2016).

40. Z. F. Wang, M.-Y. Yao, W. Ming, L. Miao, F. Zhu, C. Liu, C. L. Gao, D. Qian, J.-F. Jia, and F. Liu, Nat. Comm. **4**, 1384 (2013).

41. F. Yang, L. Miao, Z. F. Wang, M.-Y. Yao, F. Zhu, Y. R. Song, M.-X. Wang, J.-P. Xu, A. V. Fedorov, Z. Sun, G. B. Zhang, C. Liu, F. Liu, D. Qian, C. L. Gao, and J.-F. Jia, Phys. Rev. Lett. **109**, 016801 (2012).

42. L. Miao, Z. F. Wang, W. Ming, M.-Y. Yao, M. Wang, F. Yang, Y. R. Song, F. Zhu, A. V. Fedorev, Z. Sun, C. L. Gao, C. Liu, Q.-K. Xue, C.-X. Liu, F. Liu, D. Qian, and J.-F. Jia, PNAS **110**, 2758 (2013).

43. T. Hirahara, G. Bihlmayer, Y. Sakamoto, M. Yamada, H. Miyazaki, S. Kimura, S. Blugel, and S. Hasegawa, Phys. Rev. Lett. **107**, 166801 (2011).

44. I. R. Fisher, M. C. Shapiro, and J. G. Analytis, Philos. Mag. **92**, 2401 (2012).

45. W. Zhou, H. Zhu, and J. A. Yarmoff, Phys. Rev. B **97**, 035413 (2018).

46. N. D. Spencer, P. J. Goddard, P. W. Davies, M. Kitson, and R. M. Lambert, J. Vac. Sci. Technol. A **1**, 1554 (1983).

47. C. B. Weare and J. A. Yarmoff, Surf. Sci. **348**, 359 (1996).

48. J. Oberheide, P. Wilhelms, and M. Zimmer, Meas. Sci. Technol **8**, 351 (1997).

49. K. A. H. German, C. B. Weare, and J. A. Yarmoff, Phys. Rev. B **50**, 14452 (1994).

50. J. W. Rabalais, *Principles and applications of ion scattering spectrometry : surface chemical and structural analysis* (Wiley, New York, 2003).

51. H. Niehus, W. Heiland, and E. Taglauer, Surf. Sci. Rep. **17**, 213 (1993).

52. F. W. Saris, Nucl. Instr. and Meth. **194**, 625 (1982).

53. K. F. Zhang, F. Yang, Y. R. Song, C. Liu, D. Qian, C. L. Gao, and J.-F. Jia, Appl. Phys. Lett. **107**, 121601 (2015).

54. M. Chen, J.-P. Peng, H.-M. Zhang, L.-L. Wang, K. He, X.-C. Ma, and Q.-K. Xue, Appl. Phys. Lett. **101**, 081603 (2012).

55. H. Zhu, W. Zhou, and J. A. Yarmoff, Thin Solid Films **660**, 343 (2018).

56. J. P. Gauyacq and A. G. Borisov, J. Phys. Condens. Matter **10**, 6585 (1998).

57. J. Los and J. J. C. Geerlings, Phys. Rep. **190**, 133 (1990).

58. R. D. Gann, J. X. Cao, R. Q. Wu, J. Wen, Z. Xu, G. D. Gu, and J. A. Yarmoff, Phys. Rev. B **81**, 035418 (2010).

59. C. B. Weare and J. A. Yarmoff, Surf. Sci. **348**, 359 (1996).

60. R. D. Gann, Z. Sroubek, and J. A. Yarmoff, Phys. Rev. B **85**, 165307 (2012).

61. J. A. Yarmoff, Y. Yang, and Z. Sroubek, Phys. Rev. Lett. **91**, 086104 (2003).

62. P. Imperatori, D.Ferro, and V. Piacente, J. Chem. Thermodyn. **14**, 461 (1982).

63. S. Friedensen, J. T. Mlack, and M. Drndic, Sci. Rep. **7**, 13466 (2017).

Chapter 5

Cs adsorption on Bi_2Se_3

5.1. Introduction

Topological insulator (TI) materials are characterized by topological surface states (TSS) that connect the conduction and valence bands [1,2]. The electrons in these TSS are responsible for the novel spin-dependent transport properties of TI materials and their potential utility in a variety of applications [2-4]. Bi_2Se_3, which is one of the most common TIs, is a two-dimensional material that consists of stacked quintuple layers (QL) ordered as Se-Bi-Se-Bi-Se. The QLs are bonded to each other through van der Waals (vdW) forces. The TSS of Bi_2Se_3 form a simple Dirac cone at the Γ point. First principles calculations have proposed that the TSS in Bi_2Se_3 are located almost completely within the outermost QL and that the spatial distribution of the TSS electrons is inhomogeneous [5,6].

Adsorption on TIs has been extensively studied due to the interest in these surfaces as electronic materials [7-9]. Although there is still a dispute about the effects of magnetic doping of TIs, nonmagnetic atoms or molecules adsorbed on TIs can alter the surface band structure but the TSS should be protected by time-reversal symmetry.

This chapter contains materials published in Haoshan Zhu, Weimin Zhou and Jory A. Yarmoff, Cs adsorption on Bi_2Se_3, *Surf. Sci.* **683** (2019) 17-22

Alkali atom adsorption on TIs has also been studied extensively as a means to explore or modify the electronic structure [10-13]. Recent scanning tunneling microscopy (STM) and surface x-ray diffraction (SXRD) measurements, along with first principle calculations, show that most of the deposited Cs adatoms on Bi_2Se_3(0001) form one-dimensional chains along the upper portion of the step edges during the initial adsorption, while additional Cs adsorbs onto the terraces [14]. Ref. [14] also reports that Cs adsorption at Se vacancy sites is more energetically favorable than on intact areas of the terraces. Other work has indicated that there is a large energy penalty for large alkali atoms, such as Cs, to intercalate between the vdW gaps of TIs, although they are very mobile across the TI surfaces [12].

Low energy ion scattering (LEIS) is an experimental technique that has traditionally been used for surface elemental identification and atomic structural analysis of single crystal surfaces [15]. The penetration depth for low energy ions is less than a few atomic layers and, by choosing particular incident and emission angles, it is possible to probe only the outermost atomic layer [16,17]. In addition, the neutralization probability of scattered low energy alkali ions depends on the surface local electrostatic potential (LEP) above the scattering site [18-20]. This property of alkali LEIS has enabled investigations into the inhomogeneity of the LEP for single crystal surfaces that have spatial variations in the valence electron distribution [21] and for surfaces with submonolayer coverages of adsorbates [22-24]. Our previous work using neutralization in alkali LEIS successfully verified the inhomogeneous LEP and spatial distribution of the TSS states in Bi_2Te_3, which is a similar TI material to Bi_2Se_3 [25].

In the present work, LEIS and work function measurements are performed on Bi_2Se_3 surfaces exposed to Cs to investigate the adsorption sites and electronic properties. Analysis of the data confirms that Cs initially diffuses to the step edges, which leads to a concurrent reduction of the work function due to doping and the dipoles formed by the positively charged adatoms and their image charges. The work function has a minimum at a coverage of 0.1 monolayer (ML) when the Cs adatoms at the step edges are close enough to each other that their dipoles begin to depolarize. Samples monitored over long time periods indicate an additional slow, room temperature diffusion of Cs adatoms from the terraces to the step edges. Se surface vacancies are produced by Ar^+ ion bombardment, but there is no evidence of any preference for adsorption at these defect sites. In addition, the neutralization of Na^+ scattered from Cs-adsorbed surfaces confirms that the spatial distribution of the filled TSS in Bi_2Se_3 is consistent with calculations [5,6] and similar to that of Bi_2Te_3 [25,26].

5.2 Experimental Procedure

Single crystals of $Bi_2Se_{3.12}$ are grown using a slow-cooling method by melting high-purity Bi and Se shot following the recipe in Ref. [16]. An excess of Se is used to compensate for its high volatility that can lead to surface vacancies. The material cleaves easily along the (0001) plane producing samples around 10 mm in diameter. The samples are attached to a Ta sample holder by spot-welded Ta strips and cleaved in air several times to obtain a visually flat surface. They are then transferred into the main ultra-high vacuum (UHV) chamber through a load-lock.

Preparation and measurements of high-quality Bi_2Se_3 surfaces are performed inside the main UHV chamber, which has a base pressure of 2×10^{-10} Torr. The surfaces are prepared by an Ar^+ ion bombardment and annealing (IBA) procedure described elsewhere [16,27]. It has been demonstrated that the samples prepared by IBA are QL-terminated with a surface quality equivalent to those cleaved in vacuum, but that they are also more resistant to surface contamination. The IBA procedure involves a preliminary degassing at 130°C for two hours, followed by a 2-hour bombardment by 0.5 keV Ar^+ with an average beam flux of about 200 nA cm^{-2} and then a 30-min anneal at 130°C. After the preliminary process, the sample is ion bombarded for an additional 30 min and finally recrystallized by a 30 min anneal at 510°C. One cycle is generally sufficient to achieve a clean and ordered Bi_2Se_3 surface [27], but additional cycles are performed to ensure that the Ta sample holder is also clean, particularly if the work function of the holder is to be measured. Low energy electron diffraction (LEED) is employed to ensure the crystallinity of the Bi_2Se_3 surface.

Cs atoms are deposited onto the sample at room temperature by running 6 A through a well-outgassed SAES getter. The deposition rate is measured by LEIS to be around 0.02 ML min^{-1} in the initial stages when sample surface is clean and the sticking coefficient should be near unity. 1 ML is defined as the number of first layer Se atoms on the Bi_2Se_3 crystal surface, which is $6.74\text{x}10^{14}$ cm^{-2}. More than one hour of ion bombardment is needed to remove Cs from the surface after a large exposure, however, and Cs diffuses back to the surface, presumably from the sample holder, after 30 min of annealing at 510°C. Because of the difficulty in removing the Cs adatoms, the samples are

not re-prepared by IBA before each Cs exposure, but instead a newly inserted sample is used only once with cumulative Cs depositions performed to collect a set of measurements.

Changes in the surface work function due to Cs adsorption are determined by bombarding the sample with a 200 eV electron beam and measuring the energy shift of the secondary electron cut-off via a modulation technique using the LEED optics [28]. The accuracy of the cutoff measurement is better than 0.1 eV, and the absolute value is calibrated by the known work function of the clean surface. The work functions are measured about 20 min after each Cs deposition, which is the fastest that this can be achieved due to positioning and setup time, but prior to any other measurements.

Time-of-flight (TOF) LEIS spectroscopy is performed using apparatus similar to that described in Ref. [22]. A pulsed beam of 3.0 keV Na^+ ions is produced from a thermionic emission gun. The scattered projectiles are collected by a triple microchannel plate (MCP) detector mounted at the end of a 0.57 m-long flight tube. The entrance to the MCP detector is held at ground potential to ensure equal sensitivity to charged and neutral species. There is a pair of parallel plates located in the flight tube that can deflect the scattered ions so that only the scattered neutral species are collected. For all of the TOF-LEIS data collected here, the ion beam is normally incident onto the sample and the emitted projectiles are collected at a scattering angle of 125°.

5.3. Results and Discussion

A. Adsorption of Cs

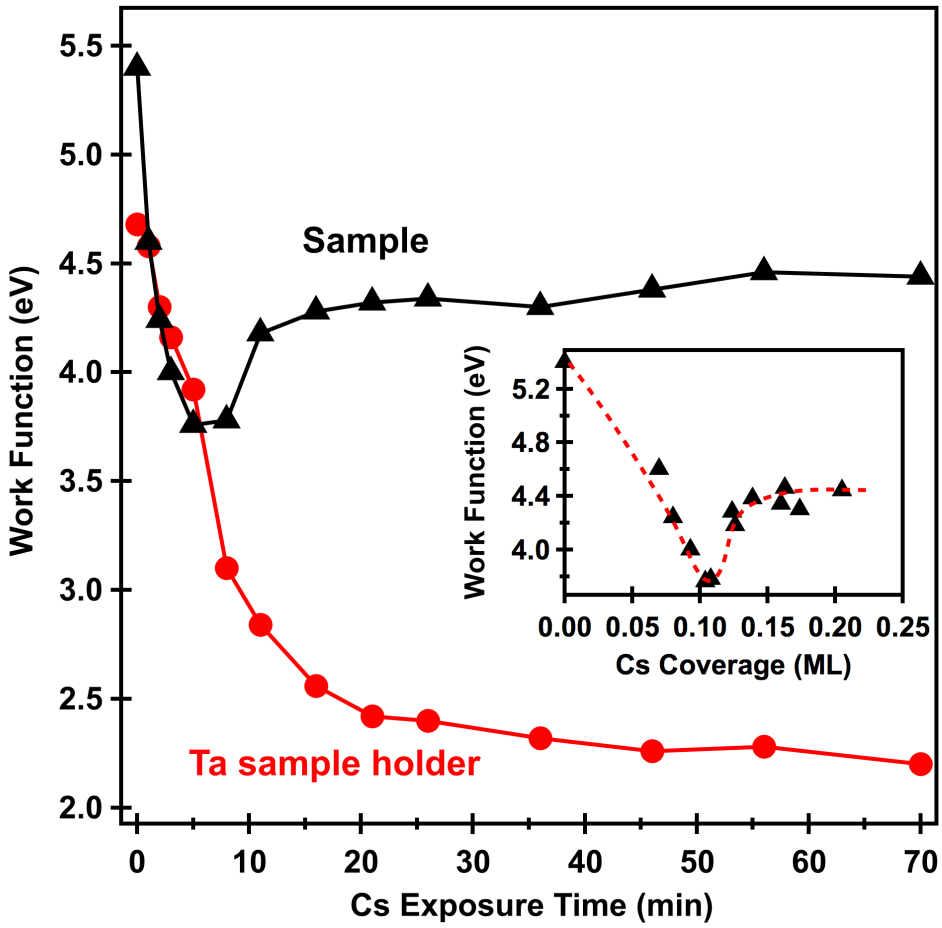

Figure 5. 1. Work function of an IBA-prepared Bi_2Se_3 surface (solid triangles) and the Ta sample holder (solid circles) shown as a function of Cs exposure time. The inset is the same work function data, but instead given with respect to Cs coverage (see text). The dashed line illustrates the trend of the work function change as an aid to the eye and is not a fit to the data.

Figure 5.1 shows the surface work functions of a Bi_2Se_3 sample and the Ta sample holder as a function of Cs exposure. The absolute value of the work function is calibrated

by setting the work function of IBA-prepared Bi_2Se_3 to the value of 5.4 eV that was measured by photoelectron spectroscopy for Bi_2Se_3 cleaved under UHV [29]. The work function of the Bi_2Se_3 sample drops from 5.4 eV to a minimum of ~3.8 eV after a 5 min Cs exposure, but it then increases to about 4.4 eV after an approximately 20 min deposition time and stays nearly constant with additional exposure. The work function is found to be uniform within an approximately 5 mm radius around the sample center.

The work function of the sample holder drops monotonically from 4.7 eV to 2.1 eV with Cs exposure. The work functions of pure Ta and Cs metal are 4.25 eV and 2.14 eV, respectively [30]. The initial work function of the sample holder is a little above the reference value because it is partially oxidized. The final value is close to the work function of Cs metal suggesting that the sample holder becomes completely covered by a Cs film after a sufficient exposure.

To better understand the behavior of Cs adsorption on Bi_2Se_3, the inset to Fig. 5.1 shows the work function as a function of the coverage of Cs on the surface. The coverage is determined from analysis of LEIS spectra, as described below. The amount of Cs on surface saturates at around 0.2 ML, indicating that the sticking coefficient drops to zero so that Cs does not form a complete film on Bi_2Se_3. Note that this saturation coverage is a factor of two smaller than is reported in Ref. [14], which is not too dissimilar a value, but the discrepancy could also be partially due to the different ways in which coverages are calculated. The work function is at its minimum at a Cs coverage around 0.1 ML and it increases with coverage above that until saturation. The saturation of the work function at such a low coverage suggests that additional Cs does not intercalate into the vdW gaps

between QLs, consistent with reports in the literature [12], as otherwise the work function would be expected to continue to decrease with exposure even as the number of Cs adatoms on the surface saturates.

A minimum in the work function vs. coverage is commonly observed for alkali adsorption on many materials [31-34]. For Cs, a minimum in the work function typically occurs in the range of 2 to 4×10^{14} atoms cm^{-2} [34,35], which would correspond to a coverage range of 0.3 to 0.6 ML for Cs/Bi_2Se_3. Adsorbed alkali adatoms donate their valence electron to the substrate becoming positively charged and thereby forming upward pointing local surface dipoles in conjunction with their image charges [36-38]. At low alkali coverages, the charged adatoms on most surfaces repel each other so that they disperse across the sample as individual adatoms that act as isolated, non-interacting dipoles that reduce the work function monotonically with coverage. As the coverage increases, however, the distance between adatoms decreases to a certain point, which is typically around 1 nm [34], at which the alkali adatoms are close enough to each other for the dipoles to interact and depolarize so that the individual dipole strengths reduce and the overall work function increases slightly.

For Cs on Bi_2Se_3, Ref. [14] shows that initially Cs primarily adsorbs on the upper step edges, forming one-dimensional structures. At higher coverages, more of the Cs adsorbs on the terraces. A close-up analysis of the STM image shown in Ref. [14] indicates an average distance between Cs adatoms along a single step edge of around 3 nm, which is larger than the distance at which depolarization normally begins, although the coverage associated with the image is not reported. Note that the 0.1 ML coverage at the minimum

in the work function, which is 6.7×10^{13} cm^{-2}, is much smaller than the typical Cs coverage on metal surfaces at the minimum. The unusually small Cs coverage at the work function minimum supports the idea that the depolarization and concurrent increase in the work function occurs as the adatoms get close to each other along the one-dimensional steps, instead of on the terraces as occurs on most material surfaces. Thus, an overall coverage of 0.1 ML places the maximum amount of Cs on the steps that can be accommodated without depolarization.

Clean Bi_2Se_3 samples prepared by IBA show a sharp hexagonal 1x1 LEED pattern [27]. The LEED pattern, in conjunction with LEIS measurements, is also used to locate the azimuthal orientations for performing LEIS [16]. As more Cs is deposited, the adatoms do not develop higher order LEED patterns, unlike Cs deposited on other materials [22,35,39-41], but instead the 1x1 pattern gets blurrier. The degradation of the LEED pattern is likely due to the preference for adsorbed Cs to diffuse to and agglomerate at the step edges, as these chains are not well ordered [14]. Since Cs is a strong electron scatterer, a non-uniform distribution of Cs would lead to a blurring of the LEED spots.

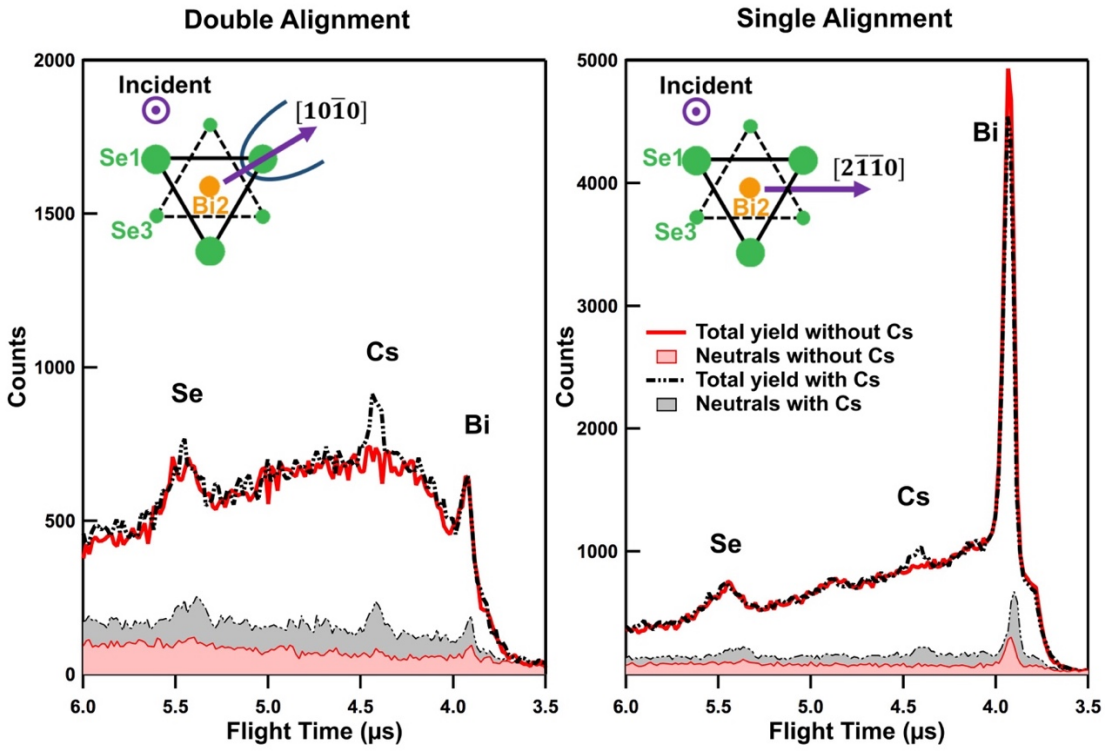

Figure 5. 2. TOF spectra of the scattered total yield and neutrals for 3.0 keV Na^+ in both double (left panel) and single (right panel) alignments before and after 0.07 ML of Cs is deposited onto Bi_2Se_3 surfaces that contain about 8% Se vacancies created by Ar^+ sputtering. The Na^+ ion beam is incident normal to sample surface and the detector is positioned at a scattering angle of 125° along the indicated azimuths. The spectra are normalized to the incident beam fluence. The insets to each panel show a schematic top view diagram of the crystal structure in which the atoms and their layer numbers are indicated along with projections of the azimuthal directions of the scattered beams.

TOF-LEIS is used to measure the surface elemental composition, termination and adsorbate coverage [16]. In LEIS, it is possible to orient the incoming ion beam and/or the position of the detector along low index crystalline directions so that single scattering is only possible from certain atoms in the crystal structure [16,17]. For all of the data presented here, the incident beam is along the surface normal so that only the three

outermost atomic layers of Bi_2Se_3[0001] are directly visible, as the atoms in the 4th and deeper layers are completely shadowed by the atoms in the first three layers. Double alignment spectra are collected from the Bi_2Se_3 surface by positioning the detector along the $(1\bar{2}10)$ azimuthal plane at an angle of 55° from the surface normal so that the projectiles scattered from 2nd layer Bi and 3rd layer Se atoms are completely blocked from reaching the detector by the first layer Se atoms [16,42]. This azimuthal orientation is illustrated in the inset to the left panel of Fig. 5.2. A single alignment orientation, in which the incoming beam is along the surface normal while the detector is not positioned along a low index direction, allows all three of the outermost atomic layers to be probed. Single alignment is achieved here by rotating the sample azimuthally by 30° from the double alignment orientation, as illustrated in the inset to the right panel of Fig. 5.2. Spectra collected from IBA-prepared Bi_2Se_3 in these two orientations are provided in Ref. [16], and they confirm that the clean surface is terminated by the Se associated with an intact QL.

Se surface vacancies are reported to be energetically favorable sites for Cs adsorption [14]. To create Se surface vacancies here, a clean Bi_2Se_3 sample is sputtered using 500 eV Ar^+ ions with a fluence of 1.8×10^{14} ions cm^{-2} followed by a light anneal at 130ºC for 90 min.

Figure 5.2 shows TOF spectra collected in both alignments before and after Cs exposure of the sputtered surfaces. The spectra are normalized by the incident beam fluence so that their absolute intensities can be directly compared to each other. The thick lines show the total yield, which includes both scattered ionic and neutral projectiles, while the

shaded areas show the projectiles that were neutralized during scattering. The x-axis is reversed as shorter flight times correspond to higher scattered kinetic energies. TOF spectra show a distinct single scattering peak (SSP) for each element on the surface atop a background of multiply scattered projectiles. After Cs exposure, the total yield spectra contain three SSPs that correspond to Na^+ scattering from Se, Cs and Bi. The total yield spectra are discussed here, as they are most useful in measuring surface coverages since the neutralization process does not need to be considered. The neutral spectra are discussed below in terms of the electronic properties of the surface. Note that the differential scattering cross section increases with the mass of the target atom and MCP detector has higher sensitivity to particles with higher energy, which causes the Bi SSP to be considerably larger than that for Se even when the surface coverages are the same. In addition, the peaks broaden due to inelastic losses that the projectiles experience as they travel through the material, which are primarily due to electron excitation [15]. Note that the longer flight time peaks appear to be wider than those at shorter flight times, but this is an artifact of plotting the data vs. flight time. Each of the SSPs actually have approximately the same width in units of energy.

The coverages of each element, including that of Cs which was used for the x-axis of the inset to Fig. 5.1, are calculated by normalizing the area of the relevant total yield SSP to the area of the total yield Bi SSP after subtracting the multiple scattering background, as described previously [22]. To calibrate the coverage, it is assumed that the area of the Bi SSP measured from the clean, unsputtered sample in single alignment (data not shown) corresponds to the 1 ML of Bi in the second atomic layer. The Bi SSP is used

for this calibration as it is the largest peak in the spectra, which leads to higher accuracy. To obtain accurate coverages, the SSP area ratios are corrected to account for both the differences in the differential cross-sections for Na^+ scattered from each element and the MCP detection efficiencies for projectiles with different scattered energies. The cross sections are calculated using the Thomas-Fermi-Moliere potential with the screening length reduced by an empirical formula [15]. The efficiency of the MCP detector as a function of scattered projectile energy is estimated from the data of Ref. [43]. Both of these effects act to increase the efficiency of projectile collection at higher scattered energies, which is why the Bi SSP is the largest one in single alignment. The error limits are determined by assuming that they are purely statistical in nature and thus equal to the square root of the total number of counts under each SSP. The calculated cross sections also have an inherent uncertainty due to a lack of accurate potentials [44,45], but this would only add a small systematic error to the reported coverages that would not alter any conclusions of the present paper.

In the double alignment spectra in the left panel of Fig. 5.2, a small Bi SSP is present after the clean surface has been sputtered. For clean defect-free surfaces, the Bi SSP is not observed in double alignment as is shown in Ref. [16]. The calibrated area of the Bi SSP represents 0.08 ML, which means that there are about 8% Se vacancies that leave the underlying Bi atoms exposed. It is assumed that most of these are isolated single atomic vacancies.

The LEIS results suggest that Cs adsorption at Se vacancies is less likely than adsorption on step edges or terrace sites. After exposure of the sputtered surface, a Cs SSP

corresponding to 0.07±0.01 ML is present in both alignments and the number of scattered neutrals increases due to Cs doping. The Bi SSP in double alignment does not measurably attenuate while the Bi SSP in single alignment decreases, which suggests Cs does not preferentially adsorb onto Se vacancy sites as otherwise the Cs adatoms would shadow the second layer Bi atoms in double alignment. This result does not agree with the DFT calculations of Ref. [14], which conclude that Se vacancy sites are at least 115 meV more energetically favorable than other sites. A possible reason for this discrepancy is that the energy savings is too small to lead to a difference in the surface site occupancy at room temperature. Furthermore, the preference of Cs adsorption at step edge sites over Se vacancies shows that these two kinds of defects behave very differently and are not equivalent.

B. Diffusion of Cs

The work function of Cs/Bi_2Se_3 not only changes with Cs coverage, but also changes over time as the sample sits in vacuum at room temperature. Figure 5.3 shows the change of work function as a function of time after various Cs exposures. When the Cs coverage is less than 0.1 ML, the work function is fairly stable, but when the coverage is larger than 0.1 ML, it increases by about 0.2 eV before stabilizing. The increase generally occurs more quickly for the samples that have a larger initial Cs coverage. The increase of work function over time suggests that adsorbed Cs is mobile and diffuses from the terraces to the step edges where the adatoms become closer together and thus more depolarized which causes the LEP above the Cs sites to increase. That the work function change occurs

more readily at larger coverages is likely caused by the fact that more Cs adatoms are located near step edges, even though a limited amount of diffusion may also occur at lower Cs coverages.

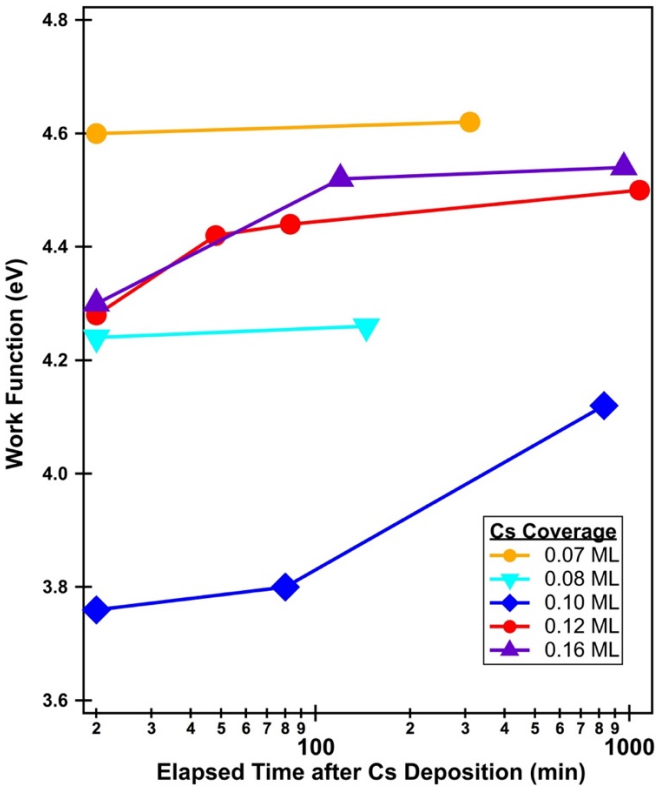

Figure 5. 3. The measured work function with the samples held at room temperature shown as a function of time after various Cs depositions on IBA-prepared Bi_2Se_3.

The neutralization of scattered low energy alkali ions provides a unique method for probing the surface local electrostatic potential (LEP) [22-24,46]. When an alkali-metal atomic particle is in the vicinity of a surface, its ionization level shifts towards the Fermi level of the solid due to interaction with its image charge, and it also broadens due to overlap of the projectile atomic level and surface wave functions [47]. In the resonant charge transfer (RCT) model, which is typically used to describe alkali-surface interactions,

electrons tunnel between the ionization level and the solid when the alkali is close to the surface. In low energy alkali scattering, the charge exchange is a non-adiabatic process in which the neutralization probability is frozen in along the outgoing trajectory while the projectile is still within a few Å's of the surface because the scattering times are short with respect to the electron tunneling rates. The neutralization probability, or neutral fraction (NF), of the particles scattered from a particular element is determined by dividing the area of the SSP in the neutrals spectrum by the area of the corresponding SSP in the total yield spectrum [22]. The measured NF depends on the value of the ionization potential, the degree to which the level shifts and broadens near the surface, and the LEP, which is sometimes referred to as the local work function, at the "freezing point" just above the scattering site. In general, the NF increases when the LEP decreases, and vice versa. This is the reason that the ratio of the neutral to the total yield SSPs increase in Fig. 5.2 after Cs deposition lowers the work function. If the surface potential were homogeneous, for example in a binary metal alloy with a free electron gas, the NF in scattering from each element would be the same.

Differences in the NF for scattering from different surface sites indicate, however, that the surface has an inhomogeneous potential. The NF in scattering from an isolated alkali adatom on a metal surface, for example, is generally larger than the NF in scattering from the substrate atoms due to the upwards dipole at the adatom site that reduces the LEP [18,48,49]. This effect is most pronounced at low coverages, where the strength of the individual dipoles is large. The prior work demonstrated that neutralization in alkali LEIS

is sensitive to the LEP on a very local scale, and that it is a particularly useful tool for imaging local dipoles on a surface with an inhomogeneous potential.

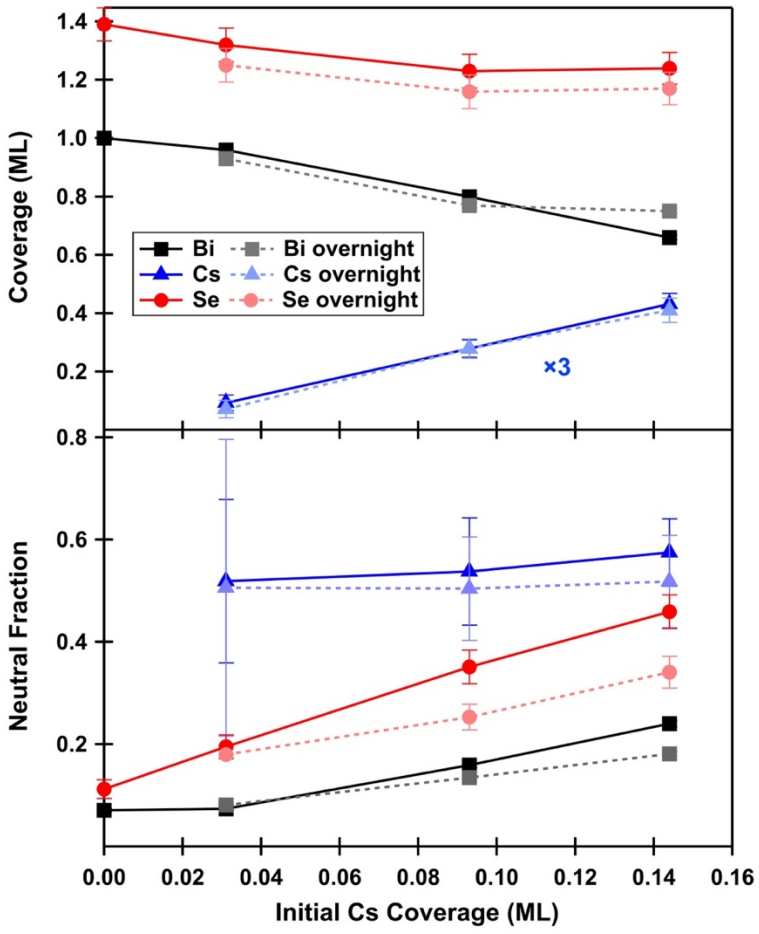

Figure 5. 4. Se, Cs and Bi coverages and neutral fractions for 3.0 keV Na^+ singly scattered in single alignment from an IBA-prepared Bi_2Se_3 sample shown as a function of the initial Cs coverage. The points connected by solid lines were derived from LEIS spectra collected immediately after deposition, while the points connected by dashed lines are from data collected after the samples sat in the UHV chamber overnight (about 9 hrs) at room temperature.

The changes in NF with coverage and over time provide further insight into the surface diffusion of Cs. Figure 5.4 shows the coverages and measured NFs of the SSPs of

all three elements as a function of the initial Cs coverage on a vacancy-free surface. The solid lines are the data collected within one hour of Cs exposure. The Cs coverage increases monotonically, as expected, and the data collected immediately after deposition is, by definition, a straight line with a slope of one. Both the Bi and Se coverages decrease with Cs coverage, however, due to shadowing by the Cs adatoms. The Cs SSP has the highest NF at all coverages due to the low LEP at the adatom sites, similar to alkali LEIS from alkali adatoms on metal and semiconductor surfaces [48]. The NF of the Cs SSP does not change significantly with coverage because it is determined by the combined effects of the decreasing global work function and the attenuating dipole strength at higher Cs coverages. The Cs NF has a large statistical error due to the small size of the SSP, however, particularly at the smallest coverages. The Bi and Se SSP NFs increase with Cs coverage due to the n-doping effect caused by Cs adsorption, as is expected.

The points connected by the dashed lines in Fig. 5.4 are obtained by collecting the same spectra after the samples have sat in the UHV chamber overnight for about 9 hrs. It is seen that the Cs surface coverage does not change over time. The NFs of all the SSPs decrease and the work function increases when the Cs coverage is close to or above 0.1 ML, however, which is the coverage at which the work function is at a minimum. These changes are consistent with the notion that Cs atoms continue to diffuse across the surface from the terraces to the step edges where their adsorption is more energetically favorable. When the Cs coverage is less than 0.1 ML, much of the Cs is concentrated at the steps but the distance between Cs adatoms is larger than the distance at which depolarization begins to occur, so that the work function and NFs do not change over time. When the Cs coverage

is larger, however, Cs adatoms from the terraces diffuse to the step edges and the increased concentration at the steps places the adatoms close enough to each other so that the dipoles start to interact, which increases the LEP and decreases the NFs.

Although surface contamination by residual gas in the UHV chamber could also contribute to the changes of work function and NF over time, as Cs adatoms are sites at which residual gasses often adsorb, that does not appear to be occurring. If contamination played a major role, then the Cs SSP should also show some decrease over time as the adatoms become covered by oxygen or other species, which is not the case here. Also, the LEED pattern (not shown) does not degrade after the sample has sat in the chamber overnight, further suggesting that contamination is not playing a role.

C. TSS charge distribution

An important observation is that the Se SSP measured from an unsputtered surface following Cs exposure always has a larger NF than the Bi SSP. The difference in the NFs is presumably due to the inhomogeneous TSS charge distribution within the first QL of Bi_2Se_3, as predicted by DFT calculations in the literature [5,6,26]. These DFT results indicate that the filled TSS are located beneath the 1st and 3rd layer Se atoms and above the 2nd layer Bi atoms, thereby forming upward dipoles at the Se sites and downward dipoles at the Bi sites. The dipoles formed by the TSS cause an increase in the Se SSP NF and a decrease in that for Bi. This same effect was observed for Na^+ scattered from clean Bi_2Te_3 [25], but it is not apparent for clean Bi_2Se_3 because it has a higher work function that causes the NFs to both be near zero so that any differences are not large enough to be measured

above the noise level. After adsorption of Cs, however, the overall work function of the sample is reduced so that the NFs all increase to values that enables the differences in the Bi and Se SSP NFs to be clearly distinguished.

The fact that the NF differences are maintained in the presence of Cs adsorbates shows that the TSS are not perturbed by the Cs adsorbates and have the same spatial distributions as on clean Bi_2Se_3 and Bi_2Te_3 surfaces. The stability of the TSS is likely due to their protection by time-reversal symmetry, but may also be partially because much of the Cs agglomerates at the step edges and thus has little effect on the electronic properties of the TIs that are determined by the band structure at the terraces.

In addition, the Bi SSP NF from a pre-sputtered surface with a 0.07 ML Cs coverage, as measured from the data in Fig. 5.2, is 0.29±0.05 for double alignment and 0.143±0.006 for single alignment. The NF in single alignment is similar to the value measured from the unsputtered surface in Fig. 5.4, which suggests that Cs adsorbs in the same manner on the pre-sputtered and unsputtered surfaces. The similarity in the single alignment NFs for as-prepared and pre-sputtered surfaces supports the conclusion reached above that there is no preference for adsorption at vacancy defect sites. The Bi SSP collected in double alignment from the pre-sputtered samples originates solely from 2^{nd} layer atoms above which there are no Se atoms, so that TSS electrons are presumably absent at these sites. In contrast, the Bi SSP in single alignment includes 2^{nd} layer Bi that is positioned below surface Se atoms so that the NF is expected to be affected by the presence of the TSS. The difference in which sites are probed would thus cause the NF of the Bi SSP in double alignment to be higher than in single alignment, which is consistent with observations. Therefore, the

smaller Bi SSP NF for a pre-sputtered surface in single alignment as compared to double alignment further confirms that the NF of the Bi SSP measured from defect-free surfaces is reduced by the dipoles formed by the TSS electrons positioned above the 2nd layer Bi atoms.

5.4. Conclusions

Both well-ordered Bi_2Se_3 surfaces and pre-sputtered surfaces that contain Se vacancies are exposed to Cs. The data indicate that Cs adsorbs as positively charged adatoms that initially agglomerate at the step edges. Above a 0.1 ML coverage, the Cs at the step edges become close enough to each other that the dipoles associated with the charged adatoms depolarize. With a sufficient Cs coverage, the work function and NF change over time suggesting that Cs adsorbed on the terraces continually diffuses to the step edges where their adsorption is more energetically favorable. There is no evidence in the present data that Cs prefers to adsorb at Se vacancy sites rather than on intact areas of the terraces. Thus, the role of any Se vacancies on the terraces is much different than that of atoms near the step edges, showing that these kinds of defects are not equivalent. In addition, Cs exposure reduces the overall work function so as to reveal that the spatial distribution of TSS charge is consistent with what is calculated by DFT and observed for clean Bi_2Te_3. This result demonstrates that alkali contamination does not perturb the TSS and thus should not interfere with devices fabricated from these materials.

Bibliography

1. M. Z. Hasan and C. L. Kane, Rev. Mod. Phys. **82**, 3045 (2010).
2. X.-L. Qi and S.-C. Zhang, Rev. Mod. Phys. **83**, 1057 (2011).
3. C. Nayak, S. H. Simon, A. Stern, M. Freedman, and S. Das Sarma, Rev. Mod. Phys. **80**, 1083 (2008).
4. Z. Jiang, C.-Z. Chang, M. R. Masir, C. Tang, Y. Xu, J. S. Moodera, A. H. MacDonald, and J. Shi, Nat. Commun. **7**, 11458 (2016).
5. W. Zhang, R. Yu, H.-J. Zhang, X. Dai, and Z. Fang, New J. Phys. **12**, 065013 (2010).
6. H. Lin, T. Das, Y. Okada, M. C. Boyer, W. D. Wise, M. Tomasik, B. Zhen, E. W. Hudson, W. Zhou, V. Madhavan, C.-Y. Ren, H. Ikuta, and A. Bansil, Nano Lett. **13**, 1915 (2013).
7. H. M. Benia, C. Lin, K. Kern, and C. R. Ast, Phys. Rev. Lett. **107**, 177602 (2011).
8. T. Valla, Z.-H. Pan, D. Gardner, Y. S. Lee, and S. Chu, Phys. Rev. Lett. **108**, 117601 (2012).
9. H. Zhu, W. Zhou, and J. A. Yarmoff, J. Phys. Chem. C **122**, 16122 (2018).
10. C. Seibel, H. Maaß, M. Ohtaka, S. Fiedler, C. Jünger, C.-H. Min, H. Bentmann, K. Sakamoto, and F. Reinert, Phys. Rev. B **86**, 161105(R) (2012).
11. M. Bianchi, R. C. Hatch, Z. Li, P. Hofmann, F. Song, J. Mi, B. B. Iversen, Z. M. Abd El-Fattah, P. Löptien, L. Zhou, A. A. Khajetoorians, J. Wiebe, R. Wiesendanger, and J. W. Wells, ACS Nano **6**, 7009 (2012).

12. A. G. Ryabishchenkova, M. M. Otrokov, V. M. Kuznetsov, and E. V. Chulkov, J. Exp. Theor. Phys+. **121**, 465 (2015).

13. Z.-H. Zhu, G. Levy, B. Ludbrook, C. N. Veenstra, J. A. Rosen, R. Comin, D. Wong, P. Dosanjh, A. Ubaldini, P. Syers, N. P. Butch, J. Paglione, I. S. Elfimov, and A. Damascelli, Phys. Rev. Lett. **107**, 186405 (2011).

14. M. M. Otrokov, A. Ernst, K. Mohseni, H. Fulara, S. Roy, G. R. Castro, J. Rubio-Zuazo, A. G. Ryabishchenkova, K. A. Kokh, O. E. Tereshchenko, Z. S. Aliev, M. B. Babanly, E. V. Chulkov, H. L. Meyerheim, and S. S. P. Parkin, Phys. Rev. B **95**, 205429 (2017).

15. H. Niehus, W. Heiland, and E. Taglauer, Surf. Sci. Rep. **17**, 213 (1993).

16. W. Zhou, H. Zhu, and J. A. Yarmoff, Phys. Rev. B **94**, 195408 (2016).

17. F. W. Saris, Nucl. Instrum. Meth. Phys. Res. **194**, 625 (1982).

18. C. B. Weare, K. A. H. German, and J. A. Yarmoff, Phys. Rev. B **52**, 2066 (1995).

19. K. A. H. German, C. B. Weare, P. R. Varekamp, J. N. Andersen, and J. A. Yarmoff, Phys. Rev. Lett. **70**, 3510 (1993).

20. T. Kravchuk, Y. Bandourine, A. Hoffman, and V. A. Esaulov, Surf. Sci. **600**, L265 (2006).

21. M. Aono, C. Oshima, S. Zaima, S. Otani, and Y. Ishizawa, Jpn. J. Appl. Phys. **20**, L829 (1981).

22. C. B. Weare and J. A. Yarmoff, Surf. Sci. **348**, 359 (1996).

23. J. A. Yarmoff, Y. Yang, and Z. Sroubek, Phys. Rev. Lett. **91**, 086104 (2003).

24. J. P. Gauyacq and A. G. Borisov, J. Phys.: Condens. Matter **10**, 6585 (1998).

25. W. Zhou, H. Zhu, and J. A. Yarmoff, Phys. Rev. B **97**, 035413 (2018).

26. T. Hirahara, G. Bihlmayer, Y. Sakamoto, M. Yamada, H. Miyazaki, S.-i. Kimura, S. Blügel, and S. Hasegawa, Phys. Rev. Lett. **107**, 166801 (2011).

27. W. Zhou, H. Zhu, C. M. Valles, and J. A. Yarmoff, Surf. Sci. **662**, 67 (2017).

28. J. H. Fritz and C. A. Haque, Rev. Sci. Instrum. **44**, 394 (1973).

29. M. T. Edmonds, J. T. Hellerstedt, A. Tadich, A. Schenk, K. M. O'Donnell, J. Tosado, N. P. Butch, P. Syers, J. Paglione, and M. S. Fuhrer, J. Phys. Chem. C **118**, 20413 (2014).

30. H. B. Michaelson, J. Appl. Phys. **48**, 4729 (1977).

31. B. N. J. Persson and H. Ishida, Phys. Rev. B **42**, 3171 (1990).

32. H. P. Bonzel, Surf. Sci. Rep. **8**, 43 (1988).

33. N. D. Lang, Phys. Rev. B **4**, 4234 (1971).

34. S. H. Chou, J. Voss, I. Bargatin, A. Vojvodic, R. T. Howe, and F. Abild-Pedersen, J. Phys.: Condens. Matter **24**, 445007 (2012).

35. J. Hrbek, Surf. Sci. **164**, 139 (1985).

36. R. W. Gurney, Phys. Rev. **47**, 479 (1935).

37. T. Aruga and Y. Murata, Prog. Surf. Sci. **31**, 61 (1989).

38. J. Topping, Proc. R. Soc. A **114**, 67 (1927).

39. C. A. Papageorgopoulos and J. M. Chen, Surf. Sci. **39**, 283 (1973).

40. A. Hohlfeld, M. Sunjic, and K. Horn, J. Vac. Sci. Technol. A **5**, 679 (1987).

41. R. D. Diehl and R. McGrath, J. Phys.: Condens. Matter **9**, 951 (1997).

42. X. He, W. Zhou, Z. Y. Wang, Y. N. Zhang, J. Shi, R. Q. Wu, and J. A. Yarmoff, Phys. Rev. Lett. **110**, 156101 (2013).

43. J. Oberheide, P. Wilhelms, and M. Zimmer, Meas. Sci. Technol. **8**, 351 (1997).

44. D. Primetzhofer, S. N. Markin, D. V. Efrosinin, E. Steinbauer, R. Andrzejewski, and P. Bauer, Nucl. Instr. Meth. Phys. Res. B **269**, 1292 (2011).

45. D. Primetzhofer, S. N. Markin, M. Draxler, R. Beikler, E. Taglauer, and P. Bauer, Surf. Sci. **602**, 2921 (2008).

46. J. J. C. Geerlings, L. F. Tz. Kwakman, and J. Los, Surf. Sci. **184**, 305 (1987).

47. J. Los and J. J. C. Geerlings, Phys. Rep. **190**, 133 (1990).

48. J. A. Yarmoff and C. B. Weare, Nucl. Instr. Meth. Phys. Res. B **125**, 262 (1997).

49. L. Q. Jiang, Y. D. Li, and B. E. Koel, Phys. Rev. Lett. **70**, 2649 (1993)